Doctoral Dissertations (All Dissertations, All Years)   Electronic Theses and Dissertations

2013-06-24

Detection of Spatial and Temporal Interactions in Renal Autoregulation Dynamics

Christopher Scully
Worcester Polytechnic Institute

Follow this and additional works at: https://digitalcommons.wpi.edu/etd-dissertations

DETECTION OF SPATIAL AND TEMPORAL INTERACTIONS IN RENAL AUTOREGULATION DYNAMICS

A Dissertation
Submitted to the Faculty of the
WORCESTER POLYTECHNIC INSTITUTE

in partial fulfillment of the requirements for the

Degree of Doctorate of Philosophy
in Biomedical Engineering

June, 2013

By

_____

Christopher George Scully

Approved by:

_____   _____

Ki H. Chon, Ph.D   Yitzhak Mendelson, Ph.D
Professor, Advisor   Associate Professor
Biomedical Engineering   Biomedical Engineering
Worcester Polytechnic Institute   Worcester Polytechnic Institute

_____   _____

Glenn R. Gaudette, Ph.D   Donald R. Brown III, Ph.D
Associate Professor   Associate Professor
Biomedical Engineering   Electrical & Computer Engineering
Worcester Polytechnic Institute   Worcester Polytechnic Institute

_____

William A. Cupples, Ph.D
Professor
Biomedical Physiology & Kinesiology
Simon Fraser University

Abstract

Renal autoregulation stabilizes renal blood flow to protect the glomerular capillaries and maintain glomerular filtration rates through two mechanisms: tubuloglomerular feedback (TGF) and the myogenic response (MR). It is considered that the feedback mechanisms operate independently in each nephron (the functional unit of the kidney) within a kidney, but renal autoregulation dynamics can be coupled between vascular connected nephrons. It has also been shown that the mechanisms are time-varying and interact with each other. Understanding of the significance of such complex behavior has been limited by absence of techniques capable of monitoring renal flow signals among a more than 2 or 3 nephrons simultaneously. The purpose of this thesis was to develop approaches to allow the identification and characterization of spatial and temporal properties of renal autoregulation dynamics.

We present evidence that laser speckle perfusion imaging (LSPI) effectively captures renal autoregulation dynamics in perfusion signals across the renal cortex of anaesthetized rats and that spatial heterogeneity of the dynamics is present and can be investigated using LSPI. Next, we present a novel approach to segment LSPI of the renal surface into phase synchronized clusters representing areas with coupled renal autoregulation dynamics. Results are shown for the MR and demonstrate that when a signal is present phase synchronized regions can be identified. We then describe an approach to identify quadratic phase coupling between the TGF and MR mechanisms in time and space. Using this approach we can identify locations across the renal surface where both mechanisms are operating cooperatively. Finally, we show how synchronization between nephrons can be investigated in relation to renal autoregulation effectiveness by comparing phase synchronization estimates from LSPI with renal autoregulation system properties estimated from renal blood flow and blood pressure measurements.

Overall, we have developed approaches to 1) capture renal autoregulation dynamics across the renal surface, 2) identify regions with phase synchronized renal autoregulation dynamics, 3) quantify the presence of the TGF-MR interaction across the renal surface, and 4) determine how the above vary over time. The described tools allow for investigations of the significance and mechanisms behind the complex spatial interactions and time-varying properties of renal autoregulation dynamics.

Acknowledgements

I would like to first thank my advisor, Dr. Ki Chon, for his guidance and support over the years. He has provided excellent opportunities for me to pursue research and develop my thoughts as a scientist. I believe that learning from him over the years has prepared me well for my future career.

I thank and am very grateful to my committee member Dr. William Cupples. I appreciate the many lengthy e-mail exchanges we had over the last few years, and I have learned much about physiology and science from him.

I would also like to thank my committee members Dr. Yitzhak Mendelson, Dr. Glenn Gaudette and Dr. Rick Brown for discussions and guidance throughout my graduate studies.

Laser speckle imaging experiments in this dissertation were performed in the laboratory of Dr. Cupples at Simon Fraser University, and I want to express my gratitude for all involved, especially Nicholas Mitrou. I thank Dr. Branko Braam at University of Alberta Hospital for his feedback over the course of this project.

I would like to thank the many graduate students and researchers who have passed through the laboratory of Dr. Chon over the years. I have had the opportunity to learn a great deal from a number of you. The experiments in Chapter 4 were performed by Dr. Kin Siu at Stony Brook University, and I thank him for collecting this data and allowing me to use it.

I would like to thank the many graduate students at Stony Brook University and Worcester Polytechnic Institute who have provided enjoyable company over the years.

Thank you to my parents, sister, family, and friends for supporting me throughout the years and encouraging my education. A special thank you to Dr. Magdalena Swierczewska; who I have been lucky enough to share the graduate student experience with.

Table of Contents

Table of Figures

Table of Tables

Abbreviations

TGF – tubuloglomerular feedback
MR – myogenic response
LSPI – laser speckle perfusion imaging
LS_{mean} – signal consisting of average of all pixels at each frame
BP – blood pressure
RBF – renal blood flow
GFR – glomerular filtration rate
TFR – time-frequency representation
TVTF – time-varying transfer function
STFT – short-time Fourier transform
VFCDM – variable frequency complex demodulation
AM – amplitude modulation
FM – frequency modulation
PC – phase coupling
NMF – non-negative matrix factorization
QPC – quadratic phase coupling
QFC – quadratic frequency coupling
HR – heart rate
RO – respiratory oscillations
BRC – baroreflex control
CV – coefficient of variation
SDR – Sprague Dawley Rat
SHR – Spontaneous Hypertensive Rat
CTL - control
L-NAME (NAM) - N^{ω}-nitro-L-arginine methyl ester
Y-27632 (Y) –rho-kinase inhibitor
NO – nitric oxide (NOS – nitric oxide synthase)

Chapter 1: Introduction

1.1   Overview

Systemic blood pressure (BP) fluctuates continuously [1]. Slow fluctuations that occur with large amplitudes can damage glomeruli capillaries in renal nephrons and disrupt glomerular filtration rate [2]. Renal autoregulation is the process that prevents kidney damage and maintains a relatively steady glomerular filtration rate during fluctuations in systemic BP by adjusting resistance in the preglomerular vasculature. Hypertensive patients with intact autoregulation generally do not incur significant renal damage, but diabetic or chronic kidney disease patients who have impaired autoregulation can develop glomerular injury from relatively minor BP elevations [3]. Tubuloglomerular feedback (TGF) and the myogenic response (MR) are the two dominant renal autoregulation mechanisms; both operate to constrict and dilate the afferent arteriole preceding each nephron [4].

The MR senses a variable related to wall shear stress that is a function of the pressure in each afferent arteriole and induces smooth muscle cell constriction or dilation as appropriate. This entire process occurs directly in the afferent arteriole and operates at a frequency of ~0.2 Hz [5]. Filtrate leaving the glomerulus capillary travels through the tubule around the loop of Henle and then back up towards the glomerulus capillary bed where contact at the macula densa is made with the afferent arteriole. Cells at the macula densa sense salt concentrations in the tubule and signal to the afferent arteriole to adjust flow rates by constricting or dilating. This process is known as TGF and has a frequency of operation of ~0.03 Hz [5]. Both the MR and TGF control smooth muscle cell activity in the afferent arteriole, and therefore an inherent interaction between the two mechanisms exists [6]. This interaction may allow TGF to control the MR [7] and provide an opportunity for more effective autoregulation [8]. In addition to the TGF-

myogenic interaction, coupling between neighboring nephrons has previously been reported [9] and TGF signals have been shown to be able to electrotonically conduct between nephrons [10]. Coupling between nephrons, referred to here as internephron coupling, has the potential for a large number of nephrons to synchronize and operate as an organized cluster.

The ability for nephrons to synchronize their activity through conducted responses is a potential additional route to adjust preglomerular resistance [10-12], as it has been shown in other vascular beds and modeling studies that conducted responses can recruit additional vessels by summing their properties as they travel upstream [13]. The occurrence of interactions between and within nephrons and physiological significance that those interactions may have is largely unknown because measurement device limitations have prevented simultaneous monitoring of a sufficient number of nephrons to extend the study of nephron interactions.

Laser speckle perfusion imaging (LSPI) allows monitoring of flow across a surface by analyzing the statistics of speckle patterns formed by shining a coherent light source across a surface [14]. In a vascularized territory, red blood cells act as scatterers blurring speckle patterns [15]. This allows a relative perfusion index that is a function of the velocity and concentration of red blood cells to be obtained at all points within an imaging window with relatively high spatial and temporal resolution [15]. In renal vascular beds, LSPI can be used to monitor blood flow fluctuations in superficial nephrons across the renal cortex [16].

1.2   Summary of Objectives

The objective of this project was to utilize LSPI to monitor renal autoregulation dynamics across the renal surface and to develop analytical tools capable of uncovering the properties within and between perfusion signals. These properties include synchronization between nephrons, the TGF-myogenic interaction within nephrons, and the time-varying nature of renal autoregulation.

2

It is the intended goal for these methods to be used for understanding the contributions that interactions in renal blood flow play in renal autoregulation effectiveness.

To report the development, testing, and experimental results of the methods, this thesis contains the following specific aims.

*Chapter 4***: *Time-frequency approaches for the detection of interactions and temporal properties in renal autoregulation.*

Time-varying and complex dynamics of renal autoregulation are reviewed along with time-frequency techniques that have been applied to the study of renal autoregulation. Through simulated signals, various time-frequency approaches applied to study renal autoregulation are tested to determine their applicability for uncovering amplitude and frequency modulation as well as detecting time-varying changes in the system gain (estimated as a function of renal blood flow (RBF) fluctuations relative to those in BP). The techniques are applied to laser Doppler flowmetry measurements on the renal cortex of anaesthetized rats where it is found that the peak system gain increases and amplitude modulation of the myogenic mechanism occurs after inhibition of nitric oxide synthase. (*Scully C. G., Siu K. L., Cupples W. A., Braam B., Chon K. H. Annals of Biomedical Engineering. 41: 172-184, 2013.*)

Chapter 5: Detecting physiological systems with laser speckle perfusion imaging of the renal cortex.

Experiments to determine if perfusion data obtained from LSPI can assess renal autoregulation dynamics are reported. RBF, BP, and LSPI are recorded during periods of control, enhanced (nitric-oxide inhibition), and attenuated (rho-kinase inhibition) autoregulation in anaesthetized rats. Spectral analysis is performed on time-series extracted from pixels across the renal surface. Frequencies related to baroreflex, respiration and cardiac pulse oscillations are highly correlated

between RBF and LSPI recordings and are homogenous across the renal surface. Renal autoregulation dynamics identified from LSPI have low correlations with those from RBF and are heterogeneous in their surface distribution. Transfer function analysis with BP as the input and RBF or LSPI signals as the output show equivalent information. Experiments reported in Chapter 5 indicate the following: (1) time-series extracted from LSPI contain appropriate flow dynamics, (2) heterogeneity exists in renal autoregulation signatures across the renal surface, and (3) LSPI of the renal cortex can be used to monitor renal autoregulation dynamics in time and space. (*Scully C.G., Mitrou N., Braam B., Cupples W.A., Chon K.H. American Journal of Physiology. Regulatory, Integrative and Comparative Physiology. 304(11):R929-39, Jun 2013.*)

Chapter 6: Segmentation of renal surface perfusion signals into clusters with phase synchronized renal autoregulation dynamics.

A method is presented to segment the imaged renal surface into regions with phase synchronized dynamics in either the TGF or MR frequency range. The approach uses a two step procedure. First, phase coherence is estimated between each pair of time-series extracted from LSPI as a measure of phase coupling between the two time-series. Phase coherence estimates are compared to a surrogate data-derived threshold that provides the expected phase coherence given the same signal dynamics but without phase coupling. A clustering method is then applied to the phase coherence estimates to identify groups of pixels that have high phase coupling with each other. Three different clustering approaches are compared for this purpose with simulated data. The applicability of the described approach is presented with experimental data.

Chapter 7: An approach to detect quadratic phase coupling between the renal autoregulation mechanisms in time and space.

A detection procedure is proposed to detect time-varying quadratic phase coupling. The approach uses wavelet bicoherence with a phase-randomization detection threshold. Simulations are presented that show the approach is capable of identifying quadratic phase coupling with high temporal resolution. It is applied to RBF and LSPI signals extracted from locations across the renal surface and shown that the distribution of quadratic phase coupling between the TGF and MR mechanisms varies in time and space. The described approach can be used to localize the presence of the TGF-myogenic interactions across the renal surface and is an indicator of where and when both are operating together. Such coordinated operation may indicate the occurrence of effective and well-organized autoregulation.

Chapter 8: Preliminary investigations into the renal autoregulation effectiveness and internephron synchronization relationship.

The relationship between renal autoregulation effectiveness and the level of synchronization present in the myogenic and TGF dynamics is explored. Indicators of renal autoregulation effectiveness and phase synchronization are estimated from the forced BP data presented in Chapter 5. Phase synchronization is significantly greater in the MR frequency range than TGF during control and enhanced autoregulation periods. Low frequency gain has a weak negative correlation with phase synchronization in the MR range and positive correlation with phase synchronization in the TGF range. These results indicate that TGF and MR oscillations may be synchronize by different mechanisms between nephrons and that such forms of synchronization have different impacts on renal autoregulation effectiveness. The analysis was expanded to compare time-varying changes in phase synchronization relative to those in system gain. We did

not identify a significant relationship between the two in either frequency range, nor were modulation frequencies of phase synchronization identified.

1.3   Dissertation Organization

The specific objectives outlined above are described in the respective chapters 4 – 8. In addition to these specific objectives this dissertation also contains the following. Chapter 2 describes the relevant renal physiology as well as what is currently understood about renal autoregulation interactions. In Chapter 3, LSPI theory is described and the specific imaging system used in this work is presented with experiments that show the applicability to monitoring renal perfusion and choices of particular experimental settings. The methods presented in this dissertation are applicable to any imaging system that can acquire the dynamics with sufficient spatial and temporal resolution. Chapter 9 summarizes the specific aims and how the developed methods can be utilized to answer questions about the role of interactions.

1.4   References

[1]   Marsh, D.J., J.L. Osborn and A.W. Cowley. 1/f fluctuations in arterial pressure and regulation of renal blood flow in dogs. *American Journal of Physiology. Renal Physiology*. 258:F1394-F400, 1990.
[2]   Loutzenhiser, R., K. Griffin, G. Williamson and A. Bidani. Renal autoregulation: new perspectives regarding the protective and regulatory roles of the underlying mechanisms. *American Journal of Physiology. Regulatory, Integrative and Comparative Physiology*. 290:R1153-R67, 2006.
[3]   Bidani, A.K. and K.A. Griffin. Pathophysiology of hypertensive renal damage: Implications for therapy. *Hypertension*. 44:595-601, 2004.
[4]   Cupples, W.A. and B. Braam. Assessment of renal autoregulation. *American Journal of Physiology. Renal Physiology*. 292:F1105-F23, 2007.
[5]   Yip, K.P., N.H. Holstein-Rathlou and D.J. Marsh. Mechanisms of temporal variation in single-nephron blood flow in rats. *American Journal of Physiology. Renal Physiology*. 264:F427-F34, 1993.
[6]   Chon, K.H., Y.-M. Chen, V.Z. Marmarelis, D.J. Marsh and N.-H. Holstein-Rathlou. Detection of interactions between myogenic and TGF mechanisms using nonlinear analysis. *American Journal of Physiology. Renal Physiology*. 267:F160-F73, 1994.
[7]   Marsh, D.J., O.V. Sosnovtseva, A.N. Pavlov, K.-P. Yip and N.-H. Holstein-Rathlou. Frequency encoding in renal blood flow regulation. *American Journal of Physiology. Regulatory, Integrative and Comparative Physiology*. 288:R1160-R67, 2005.

[8]   Cupples, W.A. Interactions contributing to kidney blood flow autoregulation. *Current Opinion in Nephrology and Hypertension*. 16:39-45 10.1097/MNH.0b013e3280117fc7, 2007.

[9]   Holstein-Rathlou, N.H. Synchronization of proximal intratubular pressure oscillations: evidence for interaction between nephrons. *Pflügers Archiv European Journal of Physiology*. 408:438-43, 1987.

[10]   Marsh, D.J., I. Toma, O.V. Sosnovtseva, J. Peti-Peterdi and N.-H. Holstein-Rathlou. Electrotonic vascular signal conduction and nephron synchronization. *American Journal of Physiology. Renal Physiology*. 296:F751-F61, 2009.

[11]   Kallskog, O. and D.J. Marsh. TGF-initiated vascular interactions between adjacent nephrons in the rat kidney. *American Journal of Physiology. Renal Physiology*. 259:F60-F64, 1990.

[12]   Laugesen, J.L., O.V. Sosnovtseva, E. Mosekilde, N.-H. Holstein-Rathlou and D.J. Marsh. Coupling-induced complexity in nephron models of renal blood flow regulation. A*merican Journal of Physiology. Regulatory, Integrative and Comparative Physiology*. 298:R997-R1006, 2010.

[13]   Diep, H.K., E.J. Vigmond, S.S. Segal and D.G. Welsh. Defining electrical communication in skeletal muscle resistance arteries: a computational approach. *The Journal of Physiology*. 568:267-81, 2005.

[14]   Dunn, A.K., H. Bolay, M.A. Moskowitz and D.A. Boas. Dynamic imaging of cerebral blood flow using laser speckle. *Journal of Cerebral Blood Flow and Metabolism*. 21:195-201, 2001.

[15]   Boas, D.A. and A.K. Dunn. Laser speckle contrast imaging in biomedical optics. *Journal of Biomedical Optics*. 15:011109-12, 2010.

[16]   Holstein-Rathlou, N.-H., O.V. Sosnovtseva, A.N. Pavlov, W.A. Cupples, C.M. Sorensen and D.J. Marsh. Nephron blood flow dynamics measured by laser speckle contrast imaging. *American Journal of Physiology. Renal Physiology*. 300:F319-F29, 2011.

Chapter 2: Background

2.1   Protective Importance of Renal Autoregulation

The kidney is responsible for maintaining fluid, electrolyte, and acid-base balance in the body. In the human kidney, blood flows through ~1,000,000 (~30,000 in rats) nephrons, the functional unit of the kidney where filtration and fluid balance occurs. The kidney accounts for ~0.5% of body mass but receives ~25% of cardiac output to maintain appropriate pressure levels for filtration in each nephron. Failure to stabilize flow at the nephron level during periods of elevated blood pressure (BP) can lead to cell damage in nephrons and disrupted fluid balance [1]. Approximately 20 million people in the United States are affected by kidney disease, and it accounts for ~80,000 deaths per year. In most cases it is a secondary disease, heavily associated with hypertension and diabetic neuropathy and often patients with these conditions die from complications of kidney disease rather than the primary condition [2].

Patients with uncomplicated hypertension are at low risk for renal damage [2]. When pressure fluctuations occur the renal vasculature responds to protect the nephrons, a process called renal autoregulation. Two situations highlighted in Figure 1 lead to renal damage: (1) systolic BP has increased to a point where the vasculature can no longer adequately respond and (2) renal autoregulation fails due to complications such as diabetic nephropathy.
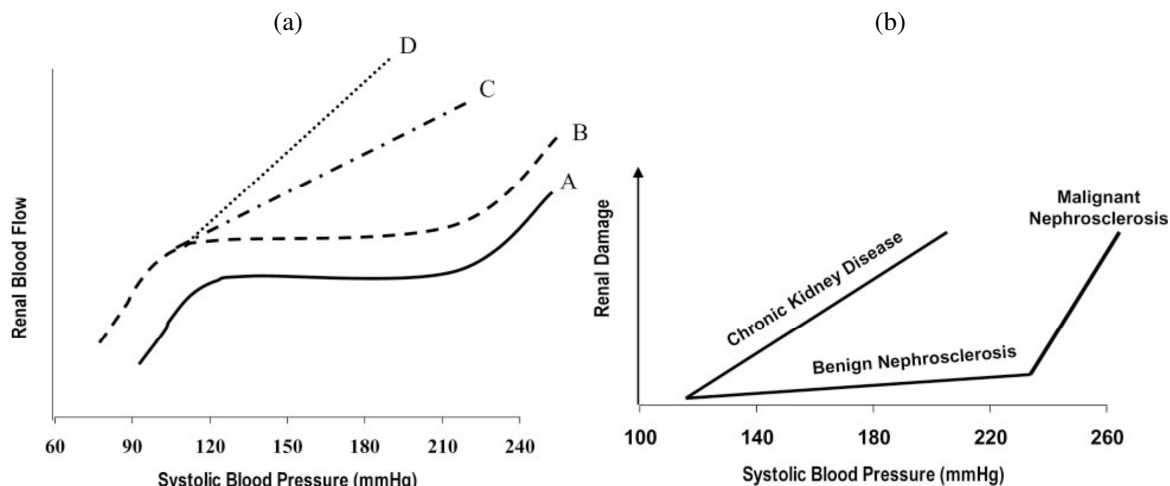
Figure 2.1 - Functional significance of renal autoregulation.
(a) Renal blood flow response to systolic blood pressure in normotensive rats (solid line, A), in vasodilation (dashed line, B), and in the chronic kidney disease model of 5/6 renal ablation representing impaired renal autoregulation (dash-dot line, C, and dot line D for complete loss of autoregulation). (b) Difference in renal damage response to blood pressure during uncomplicated hypertension (benign and malignant nephrosclerosis lines) and chronic kidney disease. *Figures reproduced with permission from [2] Bidani, A.K. and K.A. Griffin. Pathophysiology of hypertensive renal damage: Implications for therapy. Hypertension. 44:595-601, 2004.*

While systolic BP remains in a range of 90 – 220 mmHg renal blood flow (RBF) is stabilized and independent of BP in healthy patients, solid line in Figure 1a. This indicates that the vasculature is actively responding to maintain RBF. As can be seen in Figure 1b, renal damage that occurs in this situation, benign nephrosclerosis, is minimal until increased systolic BP loads, >220 mmHg, are received. After this threshold, the vasculature is no longer able to sufficiently reduce RBF and the increased BP loads reach nephrons. As nephrons are damaged in one region, the vasculature in the remaining portions of the kidney will be responsible for absorbing further increased load leading to additional damage that continues to spread, resulting in malignant nephrosclerosis. Alternatively, in chronic kidney disease patients the vasculature has a poor response to even moderate increases in systolic BP due to a failure of renal autoregulation, and there is a direct linear relationship between systolic BP and RBF. This leads to renal damage occurring with minimal increases in systolic BP, and often occurs with the coexistence of hypertension and diabetic nephropathy [2]. Over time, the continued presence of

chronic kidney disease will reduce the functional aspects of the kidney as more regions are damaged leading to end-stage renal disease and the need for dialysis or kidney transplant.

2.2   Renal Autoregulation

The kidney consists of an inner medulla and outer cortex that is surrounded by the thin, fibrous renal capsule. Blood flows into the kidney through the renal artery and proceeds to branch into a series of decreasing diameter vessels eventually reaching the cortical radial arteries. Afferent arterioles branch off cortical radial arteries and lead to cortical nephrons. Blood flows through the afferent arteriole to the glomerulus capillary bed and exits the glomerulus through the efferent arteriole, Figure 2a.
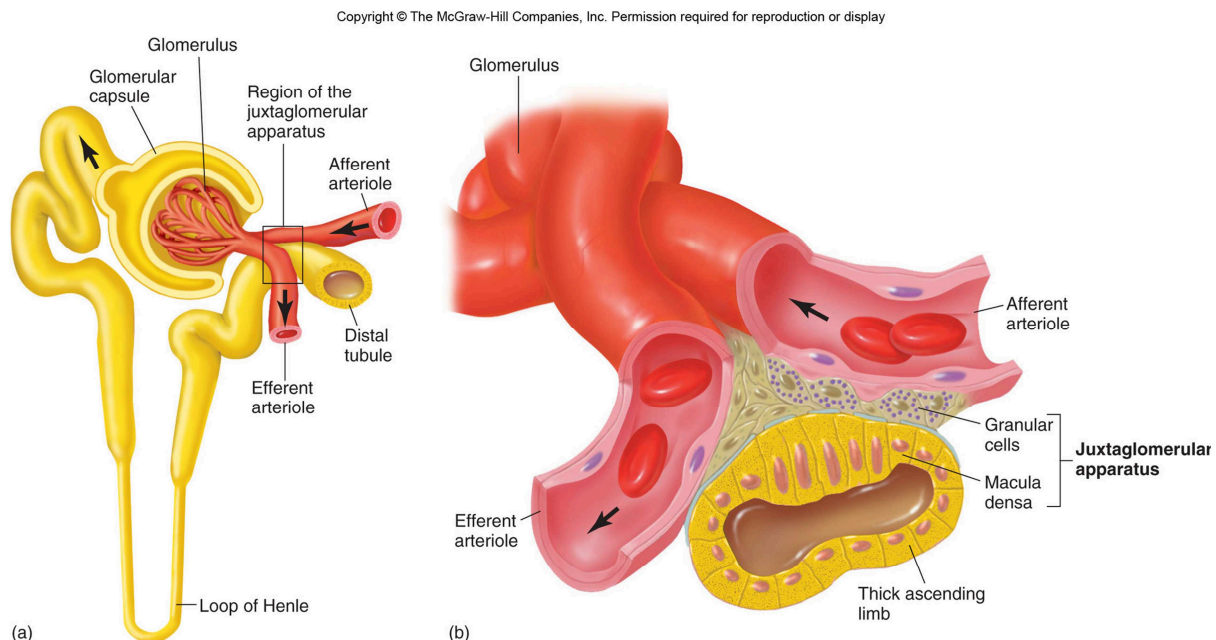
Figure 2.2 - Anatomy of the nephron.
(a) Blood flows into the nephron through the afferent arteriole and exits through the efferent arteriole. Filtrate is forced out of the glomerular capillaries into the Bowman's space. (b) At the juxtaglomerular apparatus the thick ascending limb is coupled to the afferent arteriole through the macula densa cells and granular cells.
Figure used with permission from Fox, S.I. Human Physiology. 12th edition, 2010. ©The McGraw-Hill-Companies, Inc.

Water and small molecules are driven out of the glomerular capillaries by the Starling forces between the capillaries and the surrounding space in the Bowman's capsule. Glomerular

filtration rate (GFR) is primarily set by the hydrostatic pressure in the glomerular capillaries, hydrostatic pressure in the Bowman's space, and oncotic pressure in the glomerular capillaries. A decrease in renal arterial pressure will cause a decrease in hydrostatic pressure in the glomerular capillaries if the vasculature does not respond, and therefore a decrease in GFR. Filtrate leaves the Bowman's spaces and travels through the proximal tubule, around the loop of Henle and then through the distal tubule where contact is made with the afferent arteriole at the juxtaglomerular apparatus, Figure 2b. Reabsorption of water, Na^+, Cl^-, and K^+ occurs throughout this period of flow. ~180 L of fluid are filtered through the tubule system daily in a healthy adult, but only ~0.5 – 1% is excreted in urine. The rest is reabsorbed in the tubules requiring high regulation of the reabsorption process and GFR. Hydrostatic pressure in the glomerular capillaries is maintained at ~60 mmHg to stabilize GFR by renal autoregulation. At least two mechanisms are responsible for renal autoregulation: the myogenic response (MR) and tubuloglomerular feedback (TGF) [3, 4].

The MR occurs directly in the afferent arteriole so it is able to alter preglomerular resistance [5]. When arterioles stretch due to increased transmural pressure the response of the vessel is to constrict so that the vessel resistance is increased [6, 7]. This change in vessel resistance offsets the change in pressure so that RBF is stabilized. An individual vessel will overshoot the needed range for constriction and dilation and can generate sustained oscillations. In the rat kidney these oscillations occur within a frequency range of 0.1 – 0.3 Hz [8], and the frequency of operation increases with renal perfusion pressure [9]. The MR occurs in the hydronephrotic kidney which does not contain tubules reinforcing the idea that the MR is contained entirely in the renal vasculature [10].

The second mechanism responsible for renal autoregulation is TGF and occurs at the juxtaglomerular apparatus. TGF is responsible for adjusting GFR by sensing Na^+, Cl^-, and K^+ concentrations in tubule fluid [11, 12]. Macula densa cells in the tubule at the juxtaglomerular apparatus have Na-K-2Cl co-transporters driven by Na^+ and Cl^- concentrations present in the tubule [4, 13, 14]. Increased GFR causes increased uptake of Na^+ and Cl^- by macula densa cells which in turn release ATP [15, 16]. The released ATP is converted to adenosine that activates receptors in the extra-glomerular mesangial cells and induces vasoconstriction in afferent arteriole smooth muscle cells [12]. This vasoconstriction will reduce blood flow in the afferent arterioles and GFR in the tubule. In addition to the vasoconstriction caused by adenosine, angiotensin II and nitric oxide have been shown to be involved in modulating TGF [5, 12]. TGF has three delays resulting in a slower response time than the MR: 1) salt flow through the tubule with a time delay proportional to tubule length, 2) sensor response time at the macula densa, and 3) transmission of signal through the afferent arteriole [17, 18]. Similar to the MR these delays allow for sustained oscillations to be developed in the rat kidney that occur with an operating frequency of ~0.03 Hz [19, 20]. Therefore, TGF operations are based on information acquired about altered renal function due to pressure changes in the glomerulus affecting GFR while the MR senses a variable directly related to systolic BP.

2.3   Dynamic Renal Autoregulation Assessment

Spontaneous oscillations at regular frequencies have been show for the TGF and MR operations in single nephron laser Doppler signals and RBF that occur due to the feedback operations of each mechanism [8, 21]. Slow frequencies are also present in tubule pressure signals, suggesting TGF, but the faster myogenic frequencies are not seen in these signals [8, 20]. During the process of glomerular filtration high frequency fluctuations present in the

preglomerular vasculature are filtered out due to tubular compliance and transport kinetics in the ascending limb, so that the MR is not observed in tubule pressure [22, 23].

Renal autoregulation dynamics are often assessed in animals by linear transfer function analysis using continuous BP measurements as the input and RBF as the output [3, 10, 20]. The pressure-flow relationship describes how the renal vasculature is adjusting for fluctuations in BP across a range of frequencies. At frequencies higher than the MR range of ~0.1 – 0.3 Hz, BP fluctuations are conducted directly to RBF without modification by the renal vasculature. This is identified on BP-RBF transfer functions by a gain >0 dB, coherence close to 1, and phase angle of ~0 rad. At frequencies lower than the MR frequency renal autoregulation is active to attenuate BP fluctuations in animals with functioning autoregulation. Gain decreases to <0 dB, coherence drops, and the phase angle between BP and RBF is altered. In animals without healthy autoregulation, gain stays > 0 dB at low frequencies and coherence remains close to 1, indicating that fluctuations are not being attenuated. Broad-band forcing is generally implemented experimentally when assessing renal autoregulation dynamics with transfer function analysis to ensure a range of frequencies are investigated.

Low coherence in the low frequency range indicates that non-linear or non-stationary processes are present in renal autoregulation and represent a limit to the information that can be obtained from transfer function analysis [24]. Indeed non-linear and non-stationary analyses have been applied to uncover information about the complex and time-varying renal autoregulation dynamics that are not captured with linear time-invariant transfer function analysis.

2.4   Complexity of Renal Autoregulation Dynamics

Renal autoregulation occurs by the MR and TGF operating in each of the ~30,000 nephrons in a rat kidney. Both mechanisms in all nephrons are primarily driven by BP

fluctuations which offer a source of hemodynamic coupling throughout the vasculature, but asymmetry in the vasculature disrupts the potential synchrony between nephrons [25]. Recorded RBF signals contain complex dynamics, of which it is mostly unknown how such complexity contributes to the overall effectiveness of renal autoregulation. For example, Spontaneous Hypertensive Rats (SHRs) withstand higher BP with stronger steady-state gain and have more complex, time-varying renal autoregulation than normotensive Sprague Dawley Rats (SDRs) [17, 26, 27].

2.4.1 TGF-Myogenic Interaction

TGF and the MR both operate by adjusting the tone of the afferent arteriole. Therefore, an inherent interaction exists between them. The presence of such an interaction was first shown to be non-linear in whole kidney blood flow signals using Volterra-Wiener analysis [21]. It is possible that such an interaction could be constructive or destructive towards the goal of stabilizing RBF. TGF has been shown to modulate the MR through a nitric oxide signaling pathway [28, 29].

Higher-order spectral analysis has been applied to investigate relationships between the two components from time-series of renal flow signals [30-33]. Time-invariant bispectral analysis showed that a non-linear interaction existed between TGF and the MR in stop-flow tubule pressure signals in SDRs but not SHRs [30]. It was thought that SHRs might have interactions over short time intervals, and a time-varying quadratic frequency coupling test was developed and found this to be true [31]. Using wavelet analysis, Marsh *et al.* have shown evidence from modeling and experimental studies that TGF is capable of modulating the amplitude and frequency of the MR [34, 35]. Because of the slow time delay of TGF it is not sufficient to provide renal autoregulation of higher frequencies by itself, but by modulating the

14

MR it can have a coordinated and stabilizing influence to regulate GFR [5]. In single nephron modeling studies autoregulation was less effective without TGF modulation of the MR [35].

2.4.2 Interactions between Nephrons

Nephrons are connected through the vascular network they branch from. As shown in Figure 3, multiple afferent arterioles branch from the same cortical radial artery, and afferent arterioles can have their own paired branching [36, 37]. It was first shown by Holstein-Rathlou in tubular pressure signals that neighboring nephrons could synchronize their TGF oscillations [38]. TGF synchronization was found to exist between nephrons branching from the same cortical radial artery, but physically adjacent nephrons supplied by different cortical radial arteries did not [18, 39]. This indicates that the vasculature is responsible for supplying coordination between neighboring nephrons. Marsh *et al.* showed that activation of TGF in one afferent arteriole can propagate a signal through electrotonic signal conduction that reaches the vasculature of adjacent nephrons [40]. A similar phenomenon is shown in other vascular beds and allows for upstream conduction of vascular signals [41, 45]. Modeling studies have shown that symmetric networks of nephrons can form large synchronization clusters, but asymmetry limits the size of synchronization [25, 43].
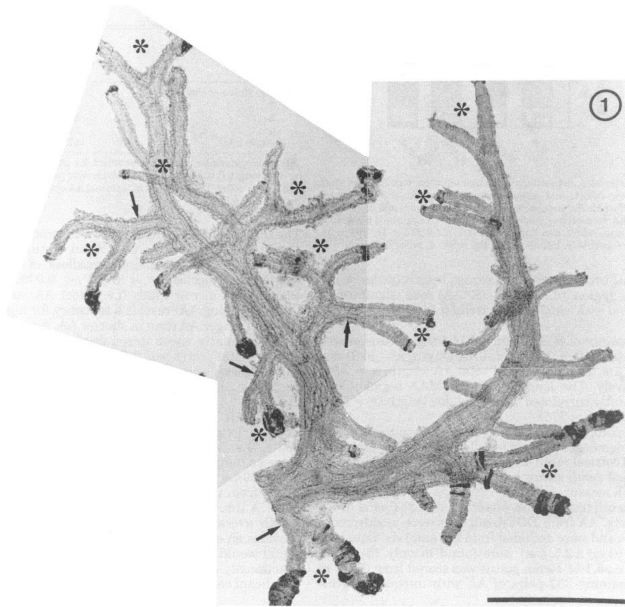
Composite micrograph of two cortical radial arteries and their afferent arteriole branching. (*) indicates afferent arteriole pairs. A total of 37 afferent arterioles are identified with 22 in pairs. Scale bar is 250 μm. *Reproduced from [35] Casellas, D., M. Dupont, N. Bouriquet, L.C. Moore, A. Artuso and A. Mimran. Anatomic pairing of afferent arterioles and renin cell distribution in rat kidneys. American Journal of Physiology. Renal Physiology. 267:F931-F36, 1994.*

Figure 2.3 - Afferent arteriole branching.

Experimental challenges have limited the exploration of synchronization in renal autoregulation between nephrons on a larger scale. Recently, Holstein-Rathlou *et al.* used laser speckle perfusion imaging (LSPI) to acquire flow signals across the renal surface [44]. Local regions were identified with phase coupled TGF oscillations, reinforcing the idea of synchronization mediated by vascular connectivity [44]. Such connectivity could allow recruitment of additional vessels to produce larger changes in preglomerular resistance than what a single nephron is capable of by itself.

2.4.3   Time-variance and the 3rd Renal Autoregulation Mechanism

It was suspected that the low coherence present in linear transfer functions could be caused by not only non-linear elements but also non-stationarities. Non-stationaries can present from 2 situations: (1) changes in blood pressure and other signals outside of the kidney or (2) changes in the properties of the feedback mechanisms. Towards the former, regular flow patterns and the oscillations that are developed by the feedback mechanisms can be interrupted by blood

pressure transients [45]. The kidney also interacts with the renin-angiotensin system through angiotensin II which can modulate kinetics of the TGF and MR [46]. This provides the potential for slow changes in the system properties over time.

To observe non-stationary behavior in TGF and the MR, time-varying transfer functions were applied to RBF and BP data from normotensive rats and SHRs [26]. The presence of time-variance was found in both the TGF and MR frequency ranges and could account for the low coherence identified in the low frequency range from transfer function analysis in normotensive rats [26]. The low coherence was not accounted for in SHRs though, indicating the presence of more non-linear mechanisms [26]. This agrees with studies of the TGF-myogenic interaction and internephron synchronization that have shown SHRs to have more complex dynamics than normotensive rats [17, 31, 47].

In addition to the TGF and MR mechanisms, Just and Arendhorst have shown evidence for a 3rd mechanism from RBF step response to a change in renal perfusion pressure that occurred over a length of 100 – 200 sec [11]. This response time is not known to be associated with either the TGF or MR mechanisms and accounted for <12% of the change in renal vascular resistance [11]. When analyzing short time-length data, the presence of an unknown slow mechanism could be interpreted as time-variance. Pavlov *et al.* identified a modulator of the TGF and MR mechanisms in renal signals with an ~0.01 Hz operation frequency [48]. Siu *et al.* performed chirp analysis by forcing blood pressure from 0 – 0.02 Hz and identified a resonance peak between of ~0.01 Hz in renal blood flow [49]. They also found amplitude modulation of the TGF and MR mechanisms at a frequency of ~0.01 Hz that was significantly higher in normotensive rats than SHR during telemetry experiments, but modulation by a low frequency source in isoflurane anaesthetized animals was not identified [49]. These independent studies

have shown the presence of a 3rd autoregulation mechanism that operates at ~0.01 Hz using multiple methods, but little is known about the potential function of this mechanism [5]. It has been suggested that its time scale is similar to the resetting of renal autoregulation by an angiotensin II dependent process [5], and modeling studies have shown that a frequency of ~0.01 Hz can arise from changes in vascular coupling in the renal network [25]. To date, the function and mechanism of the 3rd renal autoregulation component is unclear.

2.5   Summary

Renal autoregulation stabilizes RBF and GFR by at least two feedback mechanisms that are highly time-varying operating in ~30,000 nephrons in a rat kidney. Interactions between the feedback mechanisms exist within an individual nephron and between nephrons through vascular connectivity [50]. Until recently, knowledge of the extent and contribution of such complexity to the function of renal autoregulation has been restricted to what was learned from modeling studies and experiments that could only monitor a limited number of nephrons at a time [50]. With LSPI we can acquire signals related to renal flow dynamics across the surface [44]. This data can be analyzed to identify phase synchronization between locations, coupling within the interactions of individual nephrons, and how these change over time. With such analyses it can be explored how complexity plays a role in renal autoregulation and what influences it.

2.6   References

[1]   Loutzenhiser, R., K. Griffin, G. Williamson and A. Bidani. Renal autoregulation: new perspectives regarding the protective and regulatory roles of the underlying mechanisms. *American Journal of Physiology. Regulatory, Integrative and Comparative Physiology*. 290:R1153-R67, 2006.

[2]   Bidani, A.K. and K.A. Griffin. Pathophysiology of hypertensive renal damage: Implications for therapy. *Hypertension*. 44:595-601, 2004.

[3]   Cupples, W.A., P. Novak, V. Novak and F.C. Salevsky. Spontaneous blood pressure fluctuations and renal blood flow dynamics. *American Journal of Physiology. Renal Physiology*. 270:F82-F89, 1996.

[4]   Moore, L.C. and D. Casellas. Tubuloglomerular feedback dependence of autoregulation in rat juxtamedullary afferent arterioles. *Kidney International*. 37:1402-08, 1990.

[5]   Cupples, W.A. and B. Braam. Assessment of renal autoregulation. *American Journal of Physiology. Renal Physiology*. 292:F1105-F23, 2007.

[6]   Davis, M.J. and M.A. Hill. Signaling mechanisms underlying the vascular myogenic response. *Physiological Reviews*. 79:387-423, 1999.

[7]   Johnson, P.C. Autoregulation of blood flow. *Circulation Research*. 59:483-95, 1986.

[8]   Yip, K.P., N.H. Holstein-Rathlou and D.J. Marsh. Mechanisms of temporal variation in single-nephron blood flow in rats. *American Journal of Physiology. Renal Physiology*. 264:F427-F34, 1993.

[9]   Wang, X., R.D. Loutzenhiser and W.A. Cupples. Frequency modulation of renal myogenic autoregulation by perfusion pressure. *American Journal of Physiology. Regulatory, Integrative and Comparative Physiology*. 293:R1199-R204, 2007.

[10]   Cupples, W.A. and R.D. Loutzenhiser. Dynamic autoregulation in the in vitro perfused hydronephrotic rat kidney. *American Journal of Physiology. Renal Physiology*. 275:F126-F30, 1998.

[11]   Just, A. and W.J. Arendshorst. Dynamics and contribution of mechanisms mediating renal blood flow autoregulation. *American Journal of Physiology. Regulatory, Integrative and Comparative Physiology*. 285:R619-R31, 2003.

[12]   Vallon, V. Tubuloglomerular feedback and the control of glomerular filtration rate. *Physiology*. 18:169-74, 2003.

[13]   Wright, F.S. and J. Schnermann. Interference with feedback control of glomerular filtration rate by furosemide, triflocin, and cyanide. *The Journal of Clinical Investigation*. 53:1695-708, 1974.

[14]   Casellas, D. and L.C. Moore. Autoregulation and tubuloglomerular feedback in juxtamedullary glomerular arterioles. *American Journal of Physiology. Renal Physiology*. 258:F660-F69, 1990.

[15]   Schnermann, J. and D.Z. Levine. Paracrine factors in tubuloglomerular feedback: adenosine, ATP, and nitric oxide. *Annual Review of Physiology*. 65:501-29, 2003.

[16]   Komlosi, P., A. Fintha and P.D. Bell. Renal cell-to-cell communication via extracellular ATP. *Physiology*. 20:86-90, 2005.

[17]   Layton, A.T., L.C. Moore and H.E. Layton. Multistability in tubuloglomerular feedback and spectral complexity in spontaneously hypertensive rats. *American Journal of Physiology. Renal Physiology*. 291:F79-F97, 2006.

[18]   Yip, K.P., N.H. Holstein-Rathlou and D.J. Marsh. Dynamics of TGF-initiated nephron-nephron interactions in normotensive rats and SHR. *American Journal of Physiology - Renal Physiology*. 262:F980-F88, 1992.

[19]   Holstein-Rathlou, N.H., A.J. Wagner and D.J. Marsh. Tubuloglomerular feedback dynamics and renal blood flow autoregulation in rats. *American Journal of Physiology. Renal Physiology*. 260:F53-F68, 1991.

[20]   He, J. and D.J. Marsh. Effect of captopril on fluctuations of blood pressure and renal blood flow in rats. *American Journal of Physiology. Renal Physiology*. 264:F37-F44, 1993.

[21]   Chon, K.H., Y.-M. Chen, V.Z. Marmarelis, D.J. Marsh and N.-H. Holstein-Rathlou. Detection of interactions between myogenic and TGF mechanisms using nonlinear analysis. *American Journal of Physiology. Renal Physiology*. 267:F160-F73, 1994.

[22]   Layton, H.E., E.B. Pitman and L.C. Moore. Nonlinear filter properties of the thick ascending limb. *American Journal of Physiology - Renal Physiology*. 273:F625-F34, 1997.

[23]   Sakai, T., D.A. Craig, A.S. Wexler and D.J. Marsh. Fluid waves in renal tubules. *Biophysical Journal*. 50:805-13, 1986.

[24] Chon, K.Y., Y.M. Chen, N.H. Holstein-Rathlou, D.J. Marsh and V.Z. Marmarelis. On the efficacy of linear system analysis of renal autoregulation in rats. *Biomedical Engineering, IEEE Transactions on*. 40:8-20, 1993.

[25] Marsh, D.J., A.S. Wexler, A. Brazhe, D.E. Postnov, O.V. Sosnovtseva and N.-H. Holstein-Rathlou. Multinephron dynamics on the renal vascular network. *American Journal of Physiology. Renal Physiology*. 304:F88-F102, 2013.

[26] Chon, K.H., Y. Zhong, L.C. Moore, N.H. Holstein-Rathlou and W.A. Cupples. Analysis of nonstationarity in renal autoregulation mechanisms using time-varying transfer and coherence functions. *American Journal of Physiology. Regulatory, Integrative and Comparative Physiology*. 295:R821-R28, 2008.

[27] Holstein-Rathlou, N.H. and P.P. Leyssac. TGF-mediated oscillations in the proximal intratubular pressure: differences between spontaneously hypertensive rats and Wistar-Kyoto rats. *Acta Physiologica Scandinavica*. 126:333-9, 1986.

[28] Shi, Y., X. Wang, K.H. Chon and W.A. Cupples. Tubuloglomerular feedback-dependent modulation of renal myogenic autoregulation by nitric oxide. *American Journal of Physiology. Regulatory, Integrative and Comparative Physiology*. 290:R982-R91, 2006.

[29] Just, A. and W.J. Arendshorst. Nitric oxide blunts myogenic autoregulation in rat renal but not skeletal muscle circulation via tubuloglomerular feedback. *The Journal of Physiology*. 569:959-74, 2005.

[30] Chon, K.H., R. Raghavan, Y.-M. Chen, D.J. Marsh and K.-P. Yip. Interactions of TGF-dependent and myogenic oscillations in tubular pressure. *American Journal of Physiology. Renal Physiology*. 288:F298-F307, 2005.

[31] Raghavan, R., X. Chen, K.-P. Yip, D.J. Marsh and K.H. Chon. Interactions between TGF-dependent and myogenic oscillations in tubular pressure and whole kidney blood flow in both SDR and SHR. *American Journal of Physiology. Renal Physiology*. 290:F720-F32, 2006.

[32] Siu, K.L., J.M. Ann, J. Kihwan, L. Myoungho, S. Kunsoo and K.H. Chon. Statistical approach to quantify the presence of phase coupling using the bispectrum. *Biomedical Engineering, IEEE Transactions on*. 55:1512-20, 2008.

[33] Siu, K.L. and K.H. Chon. On the efficacy of the combined use of the cross-bicoherence with surrogate data technique to statistically quantify the presence of nonlinear interactions. *Annals of Biomedical Engineering*. 37:1839-48, 2009.

[34] Marsh, D.J., O.V. Sosnovtseva, A.N. Pavlov, K.-P. Yip and N.-H. Holstein-Rathlou. Frequency encoding in renal blood flow regulation. *American Journal of Physiology. Regulatory, Integrative and Comparative Physiology*. 288:R1160-R67, 2005.

[35] Marsh, D.J., O.V. Sosnovtseva, K.H. Chon and N.-H. Holstein-Rathlou. Nonlinear interactions in renal blood flow regulation. *American Journal of Physiology. Regulatory, Integrative and Comparative Physiology*. 288:R1143-R59, 2005.

[36] Casellas, D., N. Bouriquet and L.C. Moore. Branching patterns and autoregulatory responses of juxtamedullary afferent arterioles. *American Journal of Physiology. Renal Physiology*. 272:F416-F21, 1997.

[37] Casellas, D., M. Dupont, N. Bouriquet, L.C. Moore, A. Artuso and A. Mimran. Anatomic pairing of afferent arterioles and renin cell distribution in rat kidneys. *American Journal of Physiology. Renal Physiology*. 267:F931-F36, 1994.

[38] Holstein-Rathlou, N.H. Synchronization of proximal intratubular pressure oscillations: evidence for interaction between nephrons. *Pflügers Archiv European Journal of Physiology*. 408:438-43, 1987.

[39] Kallskog, O. and D.J. Marsh. TGF-initiated vascular interactions between adjacent nephrons in the rat kidney. *American Journal of Physiology - Renal Physiology*. 259:F60-F64, 1990.

[40] Marsh, D.J., I. Toma, O.V. Sosnovtseva, J. Peti-Peterdi and N.-H. Holstein-Rathlou. Electrotonic vascular signal conduction and nephron synchronization. *American Journal of Physiology. Renal Physiology*. 296:F751-F61, 2009.

[41]   Diep, H.K., E.J. Vigmond, S.S. Segal and D.G. Welsh. Defining electrical communication in skeletal muscle resistance arteries: a computational approach. *The Journal of Physiology*. 568:267-81, 2005.

[42]   Riemann, M., A. Rai, A.T. Ngo, M.H. Dziegiel, N.H. Holstein-Rathlou and C. Torp-Pedersen. Oxygen-dependent vasomotor responses are conducted upstream in the mouse cremaster microcirculation. *Journal of Vascular Research*. 48:79-89, 2011.

[43]   Marsh, D.J., O.V. Sosnovtseva, E. Mosekilde and N.-H. Holstein-Rathlou. Vascular coupling induces synchronization, quasiperiodicity, and chaos in a nephron tree. *Chaos: An Interdisciplinary Journal of Nonlinear Science*. 17:015114-10, 2007.

[44]   Holstein-Rathlou, N.-H., O.V. Sosnovtseva, A.N. Pavlov, W.A. Cupples, C.M. Sorensen and D.J. Marsh. Nephron blood flow dynamics measured by laser speckle contrast imaging. *American Journal of Physiology. Renal Physiology*. 300:F319-F29, 2011.

[45]   Wang, H., K. Siu, J. Kihwan, L.C. Moore and K.H. Chon. Identification of transient renal autoregulatory mechanisms using time-frequency spectral techniques. *Biomedical Engineering, IEEE Transactions on*. 52:1033-39, 2005.

[46]   Kim, S., H. Iwao, N. Nakamura, F. Ikemoto and K. Yamamoto. Fate of circulating renin in conscious rats. *American Journal of Physiology. Endocrinology And Metabolism*. 252:E136-E46, 1987.

[47]   Sosnovtseva, O.V., A.N. Pavlov, E. Mosekilde, K.-P. Yip, N.-H. Holstein-Rathlou and D.J. Marsh. Synchronization among mechanisms of renal autoregulation is reduced in hypertensive rats. *American Journal of Physiology - Renal Physiology*. 293:F1545-F55, 2007.

[48]   Pavlov, A.N., O.V. Sosnovtseva, O.N. Pavlova, E. Mosekilde and N.-H. Holstein-Rathlou. Characterizing multimode interaction in renal autoregulation. *Physiological Measurement*. 29:945, 2008.

[49]   Siu, K.L., B. Sung, W.A. Cupples, L.C. Moore and K.H. Chon. Detection of low-frequency oscillations in renal blood flow. *American Journal of Physiology. Renal Physiology*. 297:F155-F62, 2009.

[50]   Cupples, W.A. Interactions contributing to kidney blood flow autoregulation. *Current Opinion in Nephrology and Hypertension*. 16:39-45, 2007.

Chapter 3: Monitoring Renal Perfusion with Laser Speckle Perfusion Imaging

3.1   Spatial Monitoring of Renal Flow Patterns

The most successful techniques for studying interactions in renal autoregulation has been the use of micropipette measurements of tubular pressure and laser Doppler monitoring of efferent arteriole flow, but these techniques are limited in the number of nephrons that can be monitored simultaneously and the amount of time they can monitor for [1, 2]. Imaging techniques are advantageous because they are non-contact and simpler to implement. Previous attempts have been made to monitor renal surface perfusion with infrared (thermal), scanning laser Doppler, and NADH autofluorescence imaging, but these methods each have limitations for our purpose. Gorbach *et al.* showed the potential to monitor renal autoregulation dynamics using thermal infrared imaging, but this technique is non-specific to thermal changes in blood flow and is influenced by metabolic activity, thermal changes in nearby tissues, and fluctuations in room temperature [3-6]. It also lacks spatial resolution because of heat transfer through and across the surface of the kidney. Laser Doppler imaging uses a point laser source and requires scanning across the tissue, and therefore cannot provide instantaneous assessment of surface perfusion [7]. Autofluorescence imaging of NADH captures information related to the oxygen transport and usage related to metabolic activity [8]. It is possible to obtain high temporal and spatial resolutions but information specific to microvascular flow dynamics is not obtained [9].

Recently, laser speckle perfusion imaging (LSPI) has been shown to be capable of monitoring flow across the renal surface with sufficient spatial and temporal resolutions. Bezemer *et al.* have shown that LSPI (1) can monitor flow changes in renal cortical blood flow over time, (2) is linear with laser Doppler velocimetry measurements of renal cortical blood

flow, and (3) is capable of detecting heterogeneity in flow across the renal cortical surface [10].

Holstein-Rathlou *et al.* identified oscillations related to tubuloglomerular feedback (TGF) at points across the surface with LSPI [11]. They used this information to identify groups of nephrons with similar instantaneous TGF frequencies [11]. These studies indicate that LSPI of the renal cortex is a suitable technique for monitoring renal hemodynamics across the surface.

Efferent arterioles that leave glomeruli in the outer cortex can diverge and form a 'star' pattern underneath the renal capsule, Figure 1 [12, 13]. Oscillations related to the renal autoregulation dynamics have been shown to be present in efferent arteriole flow and TGF dynamics correspond to those in tubule pressure recordings [14]. Because these structures create a highly vascularized region that will diminish the penetration depth of our LSPI 785 nm laser source they most likely contribute the most to the acquired renal perfusion signals [11].
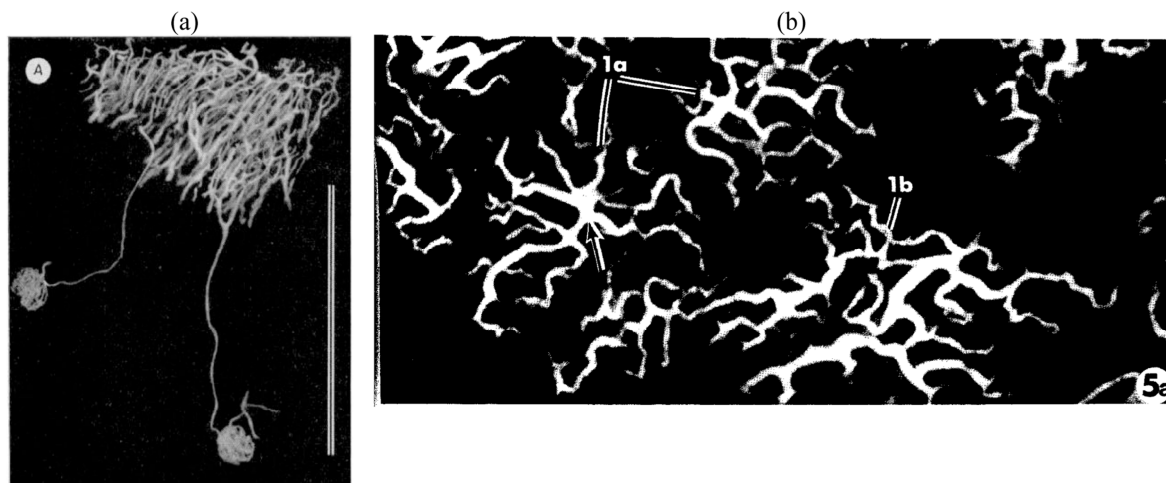
Figure 3.1 - Efferent star vessels on the renal surface.
(a) Photomicrograph of dog kidney efferent arterioles extending from the glomeruli in the outer cortex towards the renal surface where they diverge into many vessels. (Vertical bar is 1 mm) *Reproduced from [12] Beeuwkes III, R. Efferent vascular patterns and early vascular-tubular relations in the dog kidney. American Journal of Physiology. 221 (5):1361-1374, 1971.* (b) Efferent arteriole branching patterns representing the 'star' vessels underneath the renal capsule in a rat kidney (Image at x250). *Copyright © 1977 Wiley-Liss, Inc. Reproduced with permission from [13] Evan, A.P. and Dail, W.G. Efferent arterioles in the cortex of the rat kidney. The Anatomical Record. 187: 135-145, 1977.*

3.2   Laser Speckle Perfusion Imaging

LSPI has been used in biomedical applications for monitoring blood flow patterns across surfaces including retinal, skin, cerebral, and renal [15]. The optical imaging technique relies on quantifying the statistics of an imaged speckle contrast pattern generated by illuminating a surface with a coherent laser source [16, 17]. An LSPI systems consist of a coherent laser source to illuminate the target, a CCD camera to image the surface, and a processing system to determine statistics of the pattern that are related to motion. Because of imperfect surface geometry speckle patterns are created due to phase shifts in the light interaction with the surface which result in constructive and destructive interference patterns [18]. The pattern of a stationary surface will remain relatively constant, but interference patterns fluctuate when particles move through the surface. Increased velocity and volume of particles will result in increased fluctuations within the pattern so that when integrated over the exposure time of a CCD camera it will blur [18, 19]. The amount of blurring that occurs is measured by the speckle contrast,

$$K = \frac{\sigma}{\langle I \rangle} \tag{1}$$

, where σ and $\langle I \rangle$ represent the standard deviation and mean intensity over N pixels, respectively. The speckle contrast can be computed over a temporal or spatial set of pixels, Figure 2. By utilizing a spatial set of pixels the sampling rate of speckle contrast images will be that of the CCD camera intensity image series, but the spatial resolution will suffer as a function of the number of pixels. The converse is true for computing the temporal speckle contrast as the spatial sampling will be preserved but the sampling rate of the speckle contrast images will be reduced by the number of frames the speckle contrast is computed over.
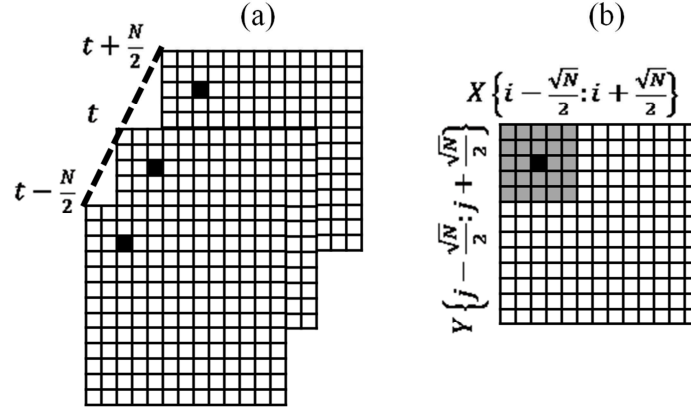
Figure 3.2 - Speckle contrast computation.
(a) Measurement of temporal contrast of the speckle pattern is over N samples at each pixel location, preserving the spatial resolution of the CCD camera while sacrificing temporal resolution. (b) Spatial contrast is computed over an NxN region at each frame, sacrificing spatial resolution while preserving temporal resolution.

Intensities of a fully evolved speckle pattern will follow a negative exponential distribution and therefore speckle contrast will range from 0 (fast motion blurring all speckles) to 1 (stationary surface with no blurring). The speckle contrast is related to the camera exposure time and the autocovariance sequence of a speckle intensity fluctuation induced by scatterers as first shown by Frecher and Briers [16] and modified in [20]. The decorrelation time of the autocovariance sequence is related to the velocity and velocity profile of scatterers [19]. To determine a quantitative measure of flow in the vasculature *a priori* information is required for the velocity profile and number of scatterers. Research is ongoing to determine the potential of quantitative flow measurements with LSPI [21]. For the purpose of the work presented in this dissertation only relative flow rates are required.

In biological applications motion can be separated into biological Brownian motion and blood flow where red blood cells act as scatters to blur the pattern [21]. Brownian motion is considered to have a much longer decorrelation time than blood flow [15]. The exposure time of the camera can be set so that the time scale of Brownian motion does not cause fluctuations that blur the contrast pattern while scatterers in blood flow will [22]. With too long an exposure time

25

the pattern will be completely blurred and speckle contrast will approach 0, and with too short an exposure time blood flow will not adequately blur the pattern [15]. Yuan *et al.* have shown that this is accomplished by having an exposure time on the same scale of the expected blood flow decorrelation time [22], and the exposure time is generally set for 1 – 25 msec in biological applications [17, 23]. In this way, changes in the speckle contrast over time are primarily a function of changes in flow patterns providing an index related to the velocity and concentration of red blood cells.

3.3   Experimental Setup

3.3.1   Imaging System

Throughout this dissertation LSPI experiments were performed with the moorFLPI laser speckle perfusion imaging system (moor Instruments, Axminster, UK). The moorFLPI consists of a 785 nm diverging laser source that is used to generate the speckle pattern. The image is captured with a 568x760 pixel CCD camera with a pixel size of ~15 μm [7] at a sampling rate of 25 Hz. The lens is typically positioned ~20 cm away from the surface to be imaged, and a magnifier can be adjusted manually to obtain a viewing window sized from 5mmx7mm up to 15cmx20cm. The specific instrument used in this dissertation had an additional magnifying lens.

The CCD camera captures the raw speckle pattern and the moorFLPI system outputs a flux image that is a function of the speckle contrast determined by a proprietary algorithm. The flux ranges from 0 – 5000 and is inversely related to the speckle contrast: a high flux corresponds to low speckle contrast which corresponds to high flow. Using the moorFLPI there are two options to compute flux, over time or space. Both methods compute speckle contrast over 25 total pixels. Using the time domain approach speckle contrast is computed from 25

temporal samples at each pixel with an output flux image sized 568x760 pixels sampled at 1 Hz. The spatial speckle contrast is computed from 5x5 squares of pixels producing an output flux image sized 113x152 pixels sampled at 25 Hz. The moorFLPI also has 4 settings for exposure time (1, 2, 4, 8 msec), a gain adjustment for the intensity of light captured, and a time constant that can be set for a low-pass filter that can be applied during recording.

3.3.2 Overview of Experiments

LSPI experiments in this dissertation were performed with anaesthetized Long-Evans rats, aged 10 – 14 weeks. Experimental details are reported in each chapter of this dissertation. In brief, rats are anaesthetized with isoflurane and placed on a heated table. A pressure transducer is connected via a cannula in the left femoral artery for continuous blood pressure measurements. A transit time ultrasound flow probe is mounted around the renal artery for continuous RBF measurements. The left kidney is exposed, freed from surrounding fat, and placed in a plastic cup just above the body and anchored to the table. The moorFLPI is positioned approximately 20 cm above the renal surface. A schematic of the data collection procedure is shown in Figure 3.
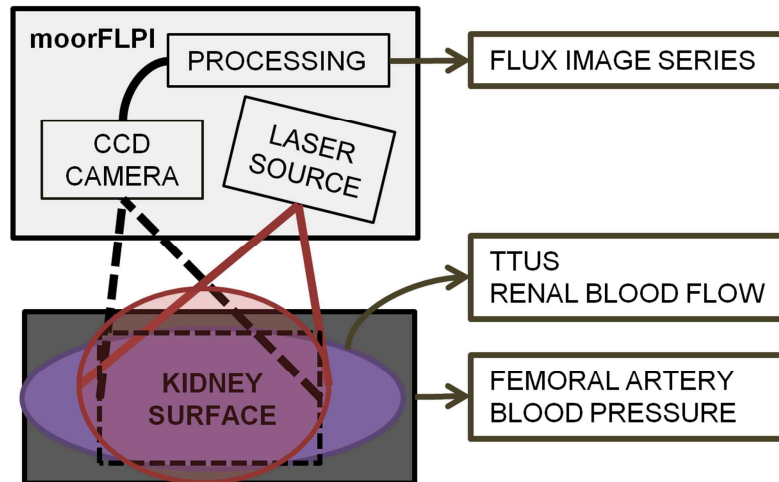
Figure 3.3 - Schematic of experimental setup.
The kidney is positioned in a kidney cup to stabilize physical motion. The moorFLPI illuminates the renal surface with a laser and it is then imaged using the CCD camera. The output of the mooFLPI is a time-stack of flux images. A transit-time ultrasound probe (TTUS) is positioned around the renal artery to continuously record total renal blood flow, and a pressure transducer is positioned in a femoral artery for continuous blood pressure measurements.

3.4   moorFLPI Preliminary Studies

3.4.1   Exposure Time

The moorFLPI offers exposure times of [1, 2, 4, and 8.3 msec]. The output moorFLPI flux sequences are calibrated for the 4 msec exposure time setting, but this is not necessarily the most appropriate for imaging the renal microcirculation. To determine the appropriate exposure time ~100 sec videos of a Long-Evans rat renal surface (N=1) were recorded at each exposure time for the spatial and temporal computation settings. moorFLPI flux values range from 0 – 5000, with 0 rarely being reached in biological systems due to the offset from Brownian motion [10, 24]. Any pixel with an output flux value of 5000 can be declared as saturated from having too low speckle contrast. The average number of saturated pixels (flux = 5000) at each frame was used as an indicator of the exposure time being short enough to reduce the impact of Brownian motion.

28

Figure 4 shows the mean light intensity (light received) and moorFLPI flux as a function of the exposure time for the two computation methods. When the lens is open longer, more light is received so the intensity is increased. With longer exposure times, slower processes are blurring the pattern which increases the flux. It can be seen that the computation method does not influence the light intensity received, as expected, but flux for the spatial computation method is greater than the temporal method at exposure times of 2, 4, and 8 msec.
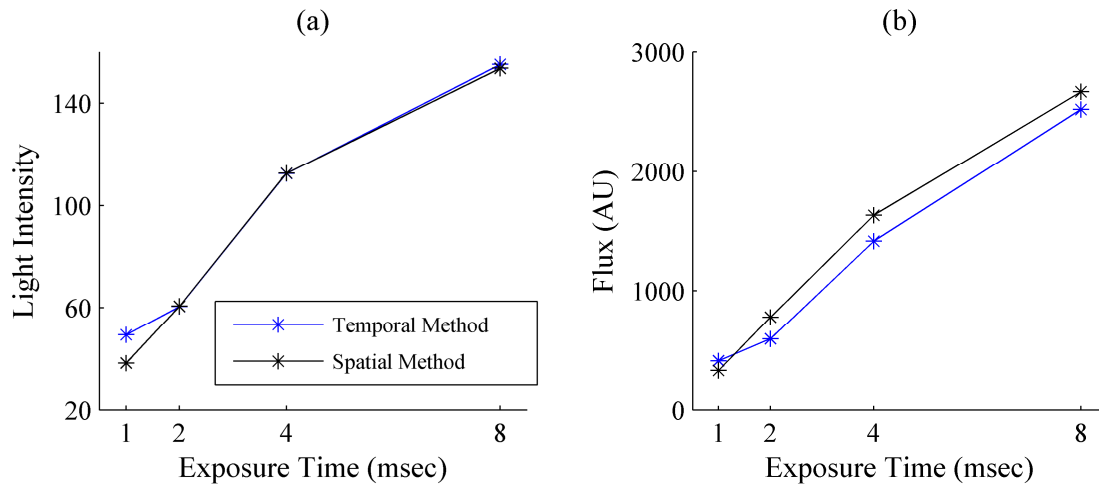
Figure 3.4 - Intensity and flux as a function of exposure time.
(a) Light intensity averaged across the renal surface as a function of the moorFLPI exposure time using the temporal (output of 568x760 pixels at 1 Hz) or spatial (output of 113x152 pixels at 25 Hz) method of flux computation. (b) moorFLPI flux averaged across the renal surface as a function of exposure time for the temporal and spatial computation methods.

A moorFLPI flux surface image is shown in Figure 5a. Figure 5b shows the time-series of flux values from the pixel surrounded by the white diamond in Figure 5a for each of the 4 exposure times. It is clear that as the exposure time is increased saturation increases and the offset increases. This is caused by slower processes than blood flow inducing motion that blurs the speckle patterns. The number of pixels saturated at each frame over the 4 exposure times is shown for both computation methods in Figure 5c.
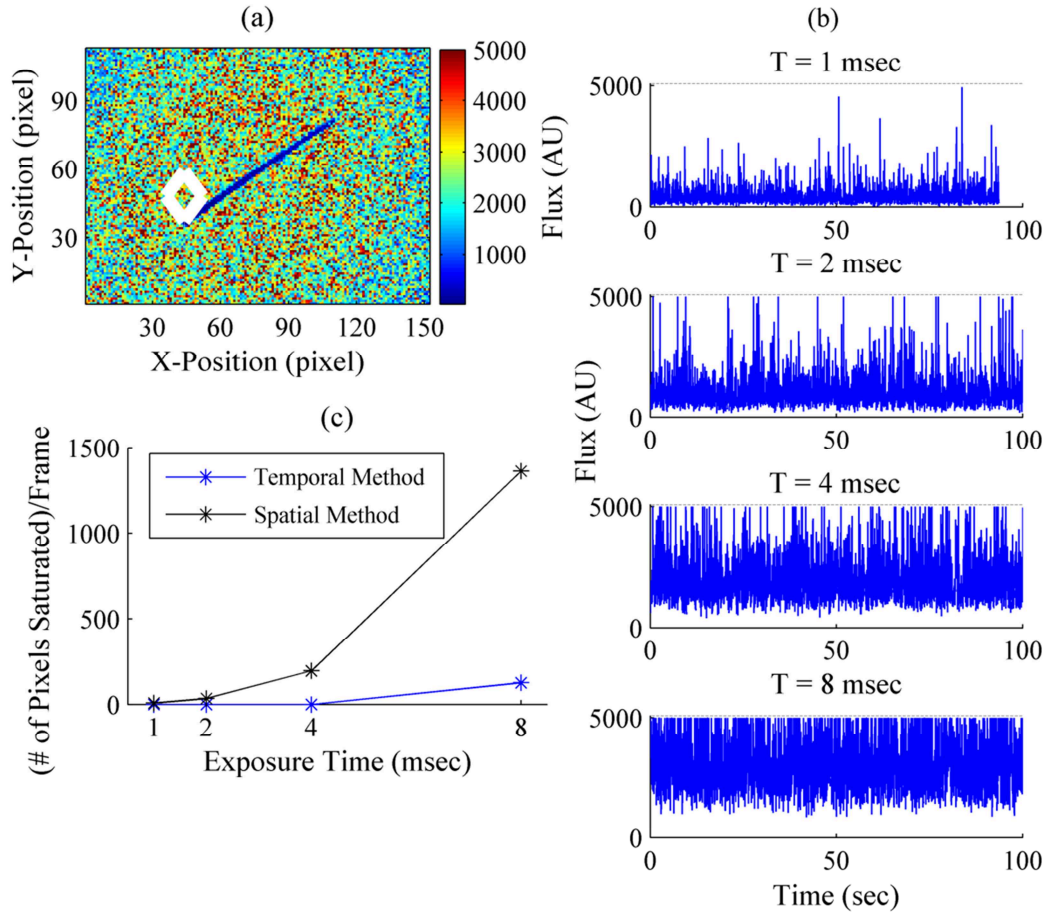
Figure 3.5 - Flux saturation due to exposure time.
(a) Surface image of laser speckle flux from low spatial resolution setting with an exposure time of 8 msec, pixel within the white diamond is used for (b), (b) time-series of moorFLPI flux from pixel location for 4 different exposure times with spatial computation method (25 Hz). The moorFLPI has a maximum flux of 5,000. Any pixel with this value is considered saturated. (c) Average (over ~100 frames) of the number of pixels saturated within the image at each exposure time for the temporal and spatial computation methods.

Significant flux saturation occurs using exposure times of 4 or 8 msec with the spatial computation method or 8 msec with the temporal computation method. Because the system is calibrated for an exposure time of 4 msec, that should be used for the temporal computation when monitoring renal microcirculation and an exposure time of 2 msec for the spatial computation method should be used to minimize flux saturation.

30

3.4.2 Flux and Renal Blood Flow Relationship

Four 25 min recording periods of the rat renal cortex (N=7) to generate 4 different levels of renal perfusion were made using each computation method (4 msec exposure for temporal and 2 msec for spatial). The first recording session was during spontaneous BP under control conditions (CTL). BP was then reduced to 60 mmHg using a servo controlled occluder and maintained for ~25 min. The servo controller was turned off, but the occluder was held so that BP remained at ~60 mmHg for the second recording session. The occluder was then released and BP returned to spontaneous levels. The non-selective NOS inhibitor N^{ω}-nitro-l-arginine methyl ester (L-NAME) (Sigma-Aldrich, Oakville, ON, Canada) was infused at a dose of 10 mg/kg$_{BW}$, and the third recording session occurred during spontaneous BP. The fourth recording session was with BP set at 60 mmHg during infusion of L-NAME. Recordings were repeated for moorFLPI spatial and temporal computation methods.

The mean BP, RBF and flux (computed over a 25x25 pixel region in the center of the LSPI sequences from spatial computation method) over each of the 4 measurement periods were determined for each animal. The Pearson Product Moment correlation coefficient between RBF and flux was determined for each animal over the 4 measurement periods, as well as over all animals and measurement periods. Repeated Measures ANOVA followed by Holm-Sidak post-hoc test was used to compare between the 4 measurement conditions ($P<0.05$ considered significant). Mean BP, RBF, and flux values over the experiments are shown in Fig. 5 with significance levels.

31
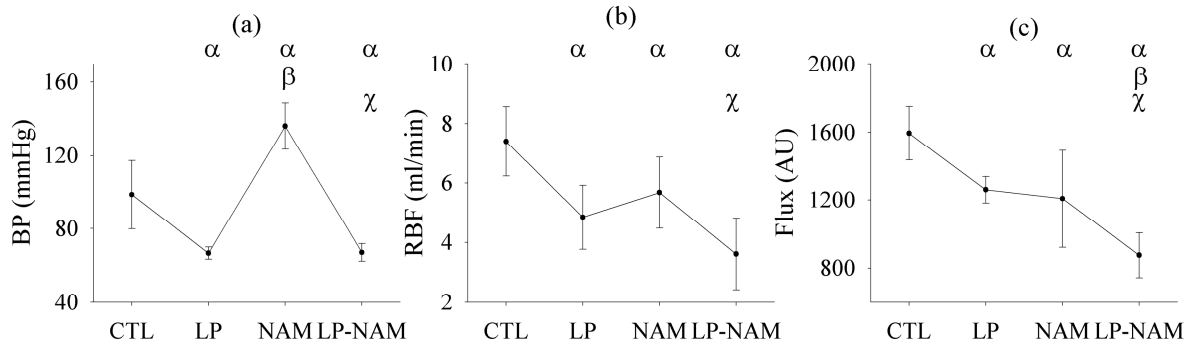
Figure 3.6 - Cardiovascular parameters at 4 perfusion levels.
 Mean (a) blood pressure, (b) renal blood flow, and (c) flux values over 4 conditions generating 4 different levels of perfusion (N=7). (CTL – control, LP – low pressure, NAM – L-NAME) α, β, and χ represent significance (P<0.05) from CTL, LP, LP-NAM, respectively, using the Holm-Sidak correction for multiple comparisons.

Figure 7 shows the linear relationship between flux and RBF for each of the 7 imaged kidneys over 4 monitoring periods. Correlation coefficients ranged from 0.77 to 0.99. The correlation coefficient computed over all animals, all measurement periods was 0.81 (P<0.0001). Within the range of flows in Figure 7, a slope of 182 ± 67 AU/(ml/min) (mean ± SD) with offset of 281 ± 252 (AU) over the 7 animals was found for the relationship between flux and renal blood flow.
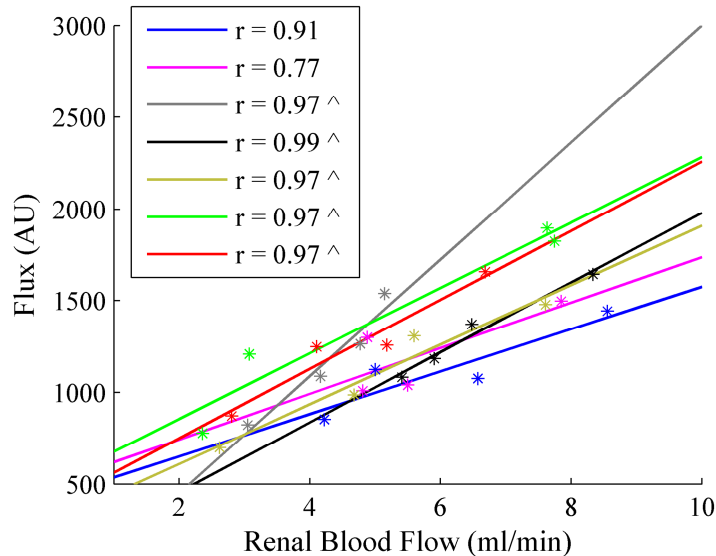
Figure 3.7 - Linearity of flux and renal blood flow.
 Laser speckle flux plotted against renal blood flow measurements for the 7 animals over 4 measurement periods with linear fit for each animal (denoted by color). Correlation coefficients between renal blood flow and laser speckle flux are shown in the legend for each animal, ^ represents P<0.05

32

A significant linear relationship was found using the moorFLPI system in relation to total RBF measurements. We do not expect a perfect correlation of 1 in all cases because the flux (local perfusion) and RBF (total flow) measurements are providing different information. This is in agreement with previous results by Bezemer *et al.* showing a linear relationship with LSPI flux, RBF, and laser Doppler velocimetry measurements (4).

3.4.3   Capturing the Renal Autoregulation Dynamics

We tested if dynamics within the TGF and myogenic response (MR) frequency ranges, 0.02 – 0.05 Hz and 0.1 – 0.3 Hz respectively, were present in the time-series extracted from pixels in the moorFLPI flux image sequences. The time-series extracted from a single pixel is shown by the black line in Figure 8a and the power spectrum of this time-series is shown in Figure 8b. It is difficult to identify any frequency peaks above the noise level in the single pixel power spectrum. A 25x25 pixel region centered at the single pixel used in Figure 8a was averaged at each frame to generate a new signal, red line in Figures 8a. Clear MR and TGF frequencies are present in the spectra for the averaged signal and background noise is greatly reduced. By averaging adjacent pixels beyond the moorFLPI temporal or spatial computation the signal-noise ratio of the renal autoregulation dynamics can be increased.
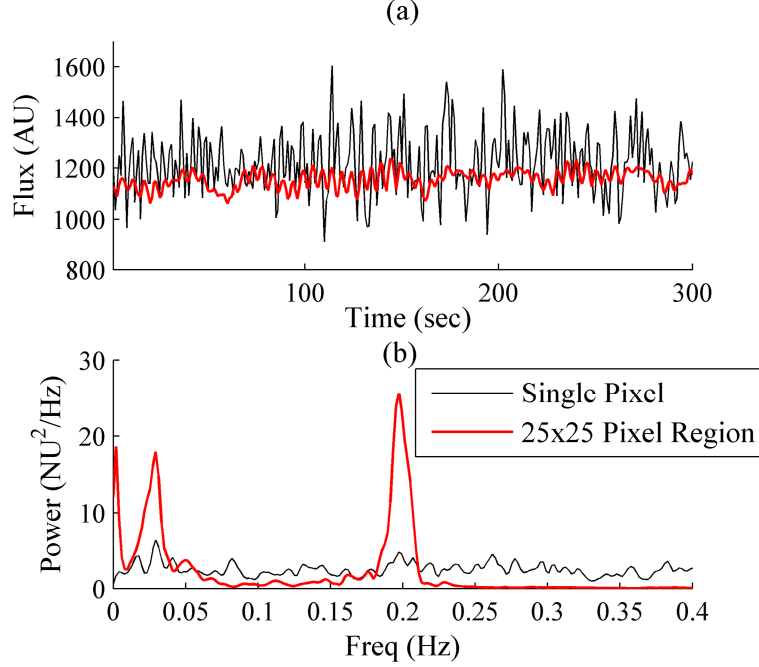
Figure 3.8 - Flux time-series and power spectrum.
(a) Signal extracted from a single pixel of a flux image sequences (black) and average of a 25x25 pixel region at each frame (red). There is a decrease in the signal variance as pixels are averaged together to generate the signal. (b) Power spectra of the two signals in (a). The single pixel signal does not show definitive autoregulation peaks, but by averaging additional pixels together at each frame to generate the signal a strong myogenic peak (~0.2 Hz) and TGF peak (~0.02 Hz) are identified.

The influence of the number of pixels to be averaged for the spatial and temporal computation methods on the signal-noise ratio of the dynamics was studied. To assess the MR and TGF signal strengths relative to the number of pixels averaged, a detection ratio was computed as

$$D = 10 \log_{10} \left(\frac{P_{sig} - \overline{P_{noise}}}{STD(P_{noise})} \right) \tag{3}$$

Here, P_{sig} is the peak power from the power spectrum within either the MR (0.1 – 0.3 Hz) or TGF (0.02 – 0.05 Hz) dynamics. $\overline{P_{noise}}$ is the mean power across frequencies in the noise region (0.3 – 0.5 Hz) and $STD(P_{noise})$ is the standard deviation of power in the noise region. A higer D indicates a signal more detectable above noise fluctuations.

34

Figure 9 shows the detection ratio as a function of the number of pixels averaged during CTL and L-NAME conditions for the MR and TGF frequencies. Results for both the moorFLPI temporal (perfusion data at 1 Hz, 568x760pixels) and spatial (25 Hz, 113x152 pixels) computation methods are shown. Because the spatial flux computation methods uses 5x5 squares each spatial flux pixel corresponds to the space of 25 temporal flux pixels. For equivalency between the spatial and temporal computation methods the total number of pixels averaged assumes each pixel from the spatial computation method contains 25 individual pixels. Therefore, the minimum number of pixels averaged for spatial computation method is 25, corresponding to a single spatial flux pixel.
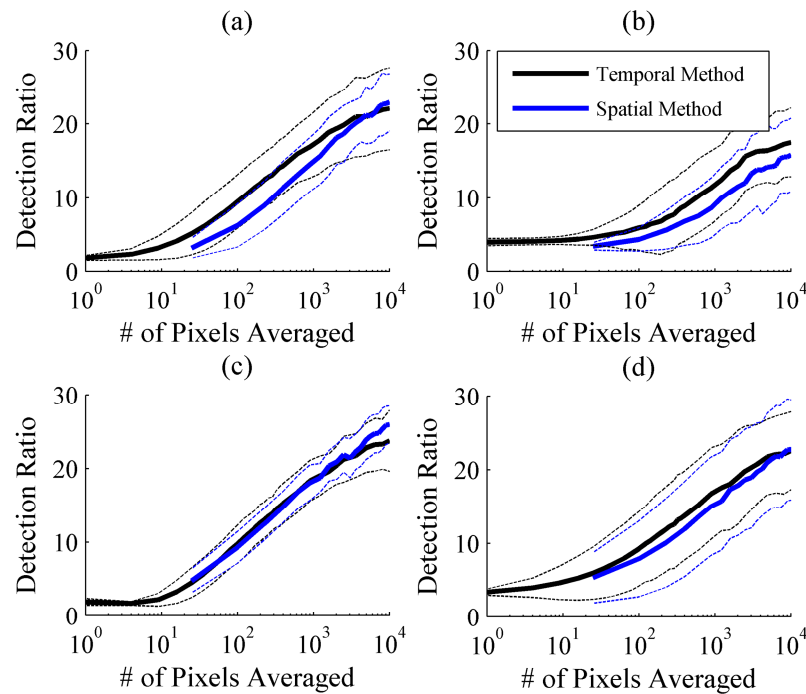
Figure 3.9 - Detection ratios as a function of the number of pixels averaged.
Detection ratios computed for increasing numbers of averaged pixels (10^2 pixels averaged = 10x10 square region) for both the temporal and spatial computation methods. During (a) TGF frequency during control, (b) Myogenic frequency during control, (c) TGF frequency during L-NAME, and Myogenic frequency during L-NAME. Here, we use 1 pixel as being the original 568x760 resolution so that the 25 Hz imaging methods starts with 25 pixels being averaged (5x5 set of pixels to compute perfusion images). Dashed lines represent standard deviations over the 7 animals.

There is a relationship between the number of pixels averaged and the strength of the TGF and MR signals. There is not a significant difference between the total numbers of pixels averaged to receive an equivalent detection ratio using either the temporal or spatial computation approach.

3.4.4   Setting the Spatial Filter

A spatial filter can be applied directly to each frame to average pixels and increase the signal-noise ratio across the renal surface. This operation will blur the flow information across the renal surface. It is therefore necessary to use a spatial filter with known width and to spatially down-sample according to the filter cut-off frequencies after spatially filtering. Side-lobes in the filter response when using square averaging filters will result in uneven distribution of spatial features based on their size. For this reason we use a Gaussian filter set to have an amplitude <0.05 for ripples <4 pixel radius for the spatial computation method. This results in a Gaussian filter with standard deviation of 3.12. The resulting spatially filtered image sequences can then be down-sampled by a factor of 4 to preserve the Nyquist frequency and reduce analysis of redundant information caused by blurring from the spatial filter.

Figure 10 shows an example of spatially filtered flux maps for one experiment collected using the spatial computation method. Figure 10a&c show the spatially filtered surface and down-sampled surface after filtering using a box-car filter, and Figure 10b&d show the same using the Gaussian filter. The dark blue space indicates the region where the hair was placed across the surface. This area was ignored during spatial filtering.
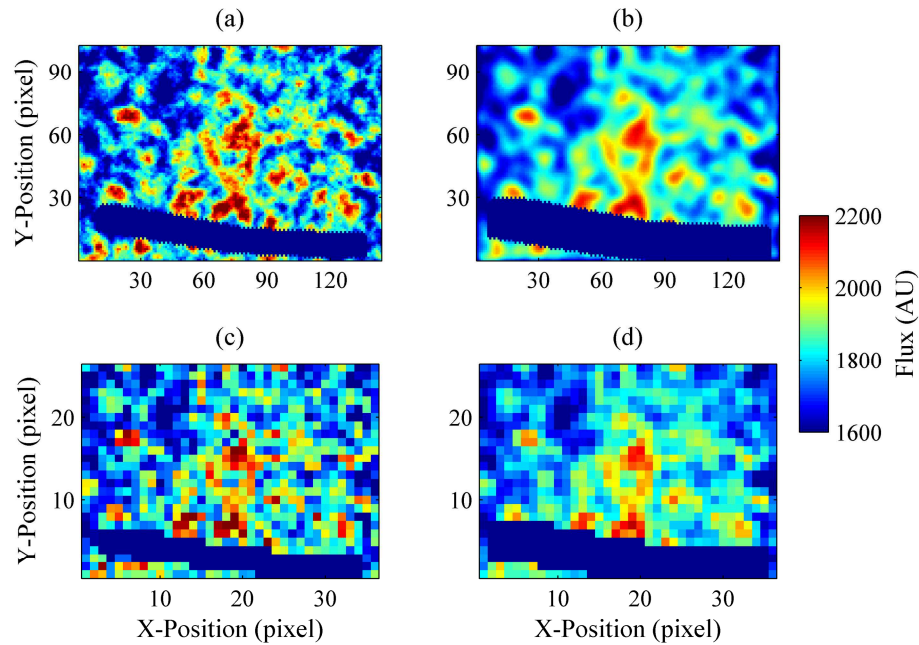
Figure 3.10 - Flux surfaces after spatial filtering.
Surface images of flux after spatially filtering: (a) square filter before down-sampling, (b) Gaussian filter before down-sampling (c) square filter after downsampling, and (d) Gaussian after down-sampling.

The detection ratios for each of the 7 animals during CTL and L-NAME within the TGF and MR frequency ranges are shown in Table 1 after applying the Gaussian filter. The detection ratio was determined for each pixel and averaged across all pixels in the image sequence. The final column represents detection ratios of the calibration block using the same procedure.

		Animal							
		1	2	3	4	5	6	7	CB
TGF	CTL	13.1	10.0	8.5	18.5	21.0	20.0	12.6	4.7
	L-NAME	28.2	21.6	20.2	27.7	23.9	23.3	27.9	
MR	CTL	2.9	7.8	2.7	13.5	4.0	11.3	12.4	4.6
	L-NAME	8.8	24.9	8.8	24.7	10.0	9.4	16.3	

Table 3.1 - Detection ratios after Gaussian filter.
CB is calibration block.

3.5   Summary

Renal autoregulation dynamics can be captured across an imaged region of the renal surface from LSPI using the moorFLPI. Mean flux values varied linearly with RBF, agreeing

with previous reports [10]. Renal autoregulation dynamics have poor signal-noise ratio when analyzing flux time-series extracted from individual pixels. It is therefore necessary to average neighboring pixels to improve the signal-noise ratio. Because the same number of pixels need to be averaged for the same signal-noise ratio using the spatial or temporal computation method, either computation method can be used. The temporal computation approach averages pixels over 25 frames reducing the effective sampling rate to 1 Hz. This approach will not capture higher frequency sources such as heart rate (~5 Hz), respiration rate (~1 Hz) and baroreflex oscillations (~0.7 Hz) that are present in blood flow signals, and we therefore lose control of accounting for their presence due to potential aliasing. It is unclear if the moorFLPI proprietary computation procedure effectively filters out all these components. If the temporal computation method is to be used the moorFLPI recommended 4 msec exposure time is appropriate since flux pixel saturation was not found to occur with these settings. When using the spatial computation method a maximum 2 msec exposure time should be used because at higher exposure times saturation of flux pixels occurred.

3.6 References

[1]   Yip, K.P., N.H. Holstein-Rathlou and D.J. Marsh. Mechanisms of temporal variation in single-nephron blood flow in rats. *American Journal of Physiology. Renal Physiology*. 264:F427-F34, 1993.
[2]   Yip, K.P., N.H. Holstein-Rathlou and D.J. Marsh. Dynamics of TGF-initiated nephron-nephron interactions in normotensive rats and SHR. *American Journal of Physiology. Renal Physiology*. 262:F980-F88, 1992.
[3]   Gorbach, A.M., H. Wang, N.N. Dhanani, F.A. Gage, P.A. Pinto, P.D. Smith, A.D. Kirk and E.A. Elster. Assessment of critical renal ischemia with real-time infrared imaging. *Journal of Surgical Research*. 149:310-18, 2008.
[4]   Gorbach, A.M., H. Wang and E. Elster. Thermal oscillations in rat kidneys: an infrared imaging study. *Philosophical Transactions of the Royal Society A: Mathematical, Physical and Engineering Sciences*. 366:3633-47, 2008.
[5]   Liu, W., J. Meyer, C.G. Scully, E. Elster and A.M. Gorbach. Observing temperature fluctuations in human using infrared imagin. *Quantitative Infrared Thermography Journal*. 8:2011.
[6]   Scully, C.G., W. Liu, J. Meyer, A. Dementyev, K.H. Chon, P. Innominato, F. Levi and A.M. Gorbach. Time-frequency analysis of skin temperature in a patient with a surface tumor

monitored with infrared imaging. *2010 International Conference on Quanitative Infrared Thermography*. 2010.

[7]   O'Doherty, J., P. McNamara, N.T. Clancy, J.G. Enfield and M.J. Leahy. Comparison of instruments for investigation of microcirculatory blood flow and red blood cell concentration. *Journal of Biomedical Optics*. 14:034025-13, 2009.

[8]   Britton, C., P. Cohen, F. Jobsis and B. Schoener. Intracellular oxidation-reduction states in vivo. *Science*. 137:499-508, 1962.

[9]   Raman, R.N., C.D. Pivetti, D.L. Matthews, C. Troppmann and S.G. Demos. A non-contact method and instrumentation to monitor renal ischemia and reperfusion with optical spectroscopy. *Optics Express*. 17:894-905, 2009.

[10]   Bezemer, R., M. Legrand, E. Klijn, M. Heger, I.C.J.H. Post, T.M. van Gulik, D. Payen and C. Ince. Real-time assessment of renal cortical microvascular perfusion heterogeneities using near-infrared laser speckle imaging. *Optics Express*. 18:15054-61, 2010.

[11]   Holstein-Rathlou, N.-H., O.V. Sosnovtseva, A.N. Pavlov, W.A. Cupples, C.M. Sorensen and D.J. Marsh. Nephron blood flow dynamics measured by laser speckle contrast imaging. *American Journal of Physiology. Renal Physiology*. 300:F319-F29, 2011.

[12]   Beeuwkes III, R. Efferent vascular patterns and early vascular-tubular relations in the dog kidney. *American Journal of Physiology*. 221:1361-74, 1971.

[13]   Evan, A.P. and W.G. Dail. Efferent arterioles in the cortex of the rat kidney. *The Anatomical Record*. 187:135-45, 1977.

[14]   Holstein-Rathlou, N.H. and P.P. Leyssac. Oscillations in the proximal intratubular pressure: a mathematical model. *American Journal of Physiology. Renal Physiology*. 252:F560-F72, 1987.

[15]   Boas, D.A. and A.K. Dunn. Laser speckle contrast imaging in biomedical optics. *Journal of Biomedical Optics*. 15:011109-12, 2010.

[16]   Fercher, A.F. and J.D. Briers. Flow visualization by means of single-exposure speckle photography. *Optics Communications*. 37:326-30, 1981.

[17]   Dunn, A.K., H. Bolay, M.A. Moskowitz and D.A. Boas. Dynamic imaging of cerebral blood flow using laser speckle. *Journal of Cerebral Blood Flow & Metabolism*. 21:195-201, 2001.

[18]   Briers, J.D., G. Richards and X.W. He. Capillary blood flow monitoringusing laser speckle contrast analysis (LASCA). *Journal of Biomedical Optics*. 4:164-75, 1999.

[19]   Briers, J.D. and S. Webster. Laser speckle contrast analysis (LASCA): a nonscanning, full-field technique for monitoring capillary blood flow. *Journal of Biomedical Optics*. 1:174-79, 1996.

[20]   Bandyopadhyay, R., A.S. Gittings, S.S. Suh, P.K. Dixon and D.J. Durian. Speckle-visibility spectroscopy: A tool to study time-varying dynamics. *Review of Scientific Instruments*. 76:093110-11, 2005.

[21]   Duncan, D.D. and S.J. Kirkpatrick. Can laser speckle flowmetry be made a quantitative tool? *Journal of the Optical Society of America A*. 25:2088-94, 2008.

[22]   Yuan, S., A. Devor, D.A. Boas and A.K. Dunn. Determination of optimal exposure time for imaging of blood flow changes with laser speckle contrast imaging. *Applied Optics*. 44:1823-30, 2005.

[23]   Ramírez-San-Juan, J.C., Y.C. Huang, N. Salazar-Hermenegildo, R. Ramos-García, J. Muñoz-Lopez and B. Choi. Integration of image exposure time into a modified laser speckle imaging method. *Physics in Medicine and Biology*. 55:6857, 2010.

[24]   Nilsson, G.E., T. Tenland and P.A. Oberg. Evaluation of a laser doppler flowmeter for measurement of tissue blood flow. *Biomedical Engineering, IEEE Transactions on*. 27:597-604, 1980.

Chapter 4: Time-Frequency Approaches for the Detection of Interactions and Temporal Properties in Renal Autoregulation

4.1   Introduction

Physiological systems contain time-varying dynamics which are generated by various sources including coupling between multiple interacting mechanisms and the impact of external stimuli. Such dynamics generate physiologically relevant information, and analysis of these properties can lead to new physiological and pathological insight. Renal autoregulation, the stabilization of renal blood flow (RBF) during fluctuations in blood pressure (BP), is one such phenomenon with time-varying dynamics which are largely due to two interacting systems, tubuloglomerular feedback (TGF) and the myogenic response (MR), that regulate glomerular filtration rate and prevent systemic BP fluctuations from damaging glomeruli [1]. The MR is intrinsic to most arteriole beds and responds to local wall tension by either constricting or dilating vessels to adjust resistance which tends to stabilize RBF. In renal autoregulation, the MR occurs in the afferent arteriole and operates within a frequency range of 0.1 – 0.3 Hz [2]. TGF senses salt concentrations in the distal tubule and transfers this information through release of a mediator to the afferent arteriole, altering resistance to adjust glomerular filtration rate [3]. This mechanism generates limit cycle oscillations within a frequency range of 0.02 – 0.06 Hz. Both mechanisms act on the afferent arteriole, creating an inherent interaction between them [4-6].

The properties and effectiveness of TGF and the MR have been analyzed by monitoring the response in RBF to step changes in BP or by time-invariant frequency domain analysis,

40

including estimation of the input/output transfer function where BP is considered the input and RBF the output [1, 7]. Use of time-invariant methods assumes a stationary system, but because of the need for renal autoregulation to adapt to large BP fluctuations and the interactions between the two autoregulatory mechanisms, as well as other related systems such as the renin-angiotensin system, renal autoregulation exhibits non-stationary behavior [8]. Zou *et al.* used short-time Fourier transforms (STFT) and multi-resolution Wavelet analysis to reveal non-stationary dynamics in RBF [9]. They showed that TGF and the MR dynamics are highly time-varying, and that time-varying properties vary between normotensive and hypertensive rat models, illustrating the need for time-varying analysis to be applied in renal autoregulation studies [9].

Subsequent studies have applied a number of time-varying methods including parametric and non-parametric time-frequency representation (TFR) techniques and time-varying transfer function (TVTF) and coherence functions to renal autoregulation data [8, 10-13]. This has revealed properties such as synchronization between the TGF and MR mechanisms [4, 14], time-varying changes in the interactions between TGF and MR [15], amplitude and frequency modulation (AM and FM, respectively) of both mechanisms [13, 16-19], temporal variability in the system gain [12], and temporal variability in the coherence [10, 11]. In almost every study a different time-varying method was applied, adding complexity to the interpretation of results. Further, to our knowledge no direct quantitative comparison has been performed, thus, it is unknown if any one single method is the best for understanding overall dynamics of renal autoregulation or if a set of different methods is required.

The purpose of this study is to directly compare time-varying methods that have previously been applied to the study of renal autoregulation to determine if different results may

be obtained that could lead to different physiological conclusions depending on the choice of method. We compare the accuracy of AM and FM detection within the TGF and MR frequency ranges using five time-frequency techniques, and we hypothesize that the variable frequency complex demodulation (VFCDM) approach provides the most accurate detection of modulation because it has previously been shown to have one of the highest resolutions when applied to renal autoregulation [20]. In addition, we compare 4 TVTF estimation methods to detect temporal changes in system gains, and we hypothesized that the use of a parametric modeling method would produce the most accurate gain estimates because it estimates only the most significant terms related to the renal autoregulation dynamics. We then apply the methods to analyze time-varying characteristics of renal autoregulation in anesthetized rats.

4.2   Materials and Methods

4.2.1   Time-Frequency Spectral Methods

Five methods were used to estimate time-varying spectra: STFT, continuous Wavelet transform (CWT), smoothed pseudo Wigner-Ville distribution (SPWV), variable frequency complex demodulation (VFCDM), and the time-varying optimal parameter search (TVOPS) for autoregressive parameter estimation. In the following, we briefly describe each of the methods.

Short-Time Fourier Transform

The STFT is computed by using a sliding time-window and computing the Fourier transform over each section expressed as

$$STFT(t, f) = \int_{-\infty}^{\infty} x(u)h^*(u - t)e^{-i2\pi f u} \, du \tag{1}$$

where *x(u)* represents the signal, *h(u-t)* a windowing function, and (*) the complex conjugate. We used a Hamming window of length 64 samples; adjusting the length of the window alters the

42

time and frequency resolution of the STFT. This window size provided a frequency resolution small enough to detect changes in the test signal for frequency modulation.

Continuous Wavelet Transform

The CWT is computed by convolving a wavelet function with a time series as the wavelet function is dilated across scales and translated in time:

$$W(t,s) = \frac{1}{\sqrt{s}} \int_{-\infty}^{\infty} x(\tau)\psi^*\left(\frac{\tau - t}{s}\right) d\tau \tag{2}$$

A wavelet function, ψ, is a zero-mean function that can be localized in time and space [21]. We used the Morlet wavelet, shown in Eq. (3). A center frequency, ω_o, is chosen for the Morlet wavelet to set the relationship between the frequency and each scale, s. ω_o was set to 6, similar to other groups that have used the Morlet wavelet for analyzing renal autoregulation [13, 14, 17, 18].

$$\psi(t) = \pi^{-1/4} e^{i\omega_o t} e^{-t^2/2} \tag{3}$$

Smoothed Pseudo Wigner-Ville

The SPWV distribution is a member of the Cohen's class of time-frequency representations and can be obtained from a signal *x(t)* as

$$SPWV(t,f) = \int_{-\infty}^{\infty} h(\tau) \int_{-\infty}^{\infty} g(s-t)x\left(s+\frac{\tau}{2}\right)x^*\left(s-\frac{\tau}{2}\right) e^{-i2\pi f\tau} ds d\tau \tag{4}$$

using a frequency smoothing window, *h*, and temporal smoothing window, *g* [22]. In this study, we used a Hamming window for both *h* and *g* sized at 64 and 16 data points, respectively. The frequency smoothing window was set to match that used for the STFT. The temporal smoothing window, *g*, was set to minimize the influence of cross-terms introduced into the Wigner-Ville distribution when multiple frequencies are present in a single signal [22]. The size of the

43

temporal smoothing window was set as a compromise to minimize the effect of cross-terms without introducing smoothing to the point where modulation could not be recognized.

Variable Frequency Complex Demodulation

The VFCDM approach is described in detail in Wang *et al.* [20]. It is performed in a two-step procedure as described below. The fixed-frequency approach is used to generate an initial time-frequency estimate, and the dominant frequency components in that estimate are used as backbone frequencies to generate a refined estimate using the variable frequency approach.

Fixed-Frequency Approach: Fixed-frequency complex demodulation (FFCDM) is performed by

1. The signal, *x(t)*, is multiplied by $e^{-i2\pi f_o t}$ at a set of fixed center frequencies f_o [0.01, 0.02…0.49 Hz].

2. The resulting complex demodulate at each center frequency is low-pass filtered (normalized cut-off frequency of 0.01 Hz) breaking the signal into a series of band-pass filtered components.

3. The amplitude and phase of each component are determined and then used to reconstruct each component, *y(t)*, at its center frequency.

$$y(t) = A(t)\cos(2\pi f_o t + \varphi(t)) \tag{5}$$

4. The Hilbert transform is taken of each y(t) to determine the instantaneous amplitude and frequency, and a TFR is constructed by combining the instantaneous amplitudes and frequencies of all components [23].

Variable Frequency Approach: After FFCDM is performed to obtain an initial time-frequency estimate, the dominant frequencies are extracted as the new, now time-varying, center frequencies. VFCDM is performed by

1. The original signal, $x(t)$, is multiplied by $e^{-i\int_0^t 2\pi f_o(\tau)d\tau}$, where $f_o(\tau)$ represents the new set of time-varying center frequencies.

2. A low-pass filter (normalized cut-off frequency of 0.005 Hz) is applied to each variable frequency complex demodulate to generate a series of band-pass filtered components.

3. Amplitude and phases are determined of each component for reconstruction at the time-varying center frequency as

$$y(t) = A(t)\cos\left(\int_0^t 2\pi f_o(\tau)d\tau + \varphi(\tau)\right) \tag{6}$$

4. The Hilbert transform of each band-pass filtered $y(t)$ determines the instantaneous amplitude and frequency, and a refined time-frequency estimate is generated.

Time-varying Optimal Parameter Search

The TVOPS method for autoregressive parameter estimation fits the time-varying model shown in equation 7, where a are the AR parameters at each time index n, y is the signal, and e is the prediction error between the model and the signal. The AR parameters are estimated using TVOPS as described by Zou *et al.* [24] by expanding the system onto a set of basis functions. 5 Legendre basis functions and an initial AR model order of 14 were used. TVOPS is designed to select only the significant model terms from an initial over-determined model order, and has been shown to be more accurate than other model order criteria such as the Akaike Information criterion and minimum description length [25].

$$y(n) = -\sum_{i=1}^{P} a(i,n)y(n-i) + e(n) \tag{7}$$

From the AR parameters, the time-varying spectral representation is generated as

$$S(n, f) = \frac{T}{\left|1 + \sum_{k=1}^{m} a(k,n)e^{-i2\pi fTk}\right|^2}$$
(8)

where T represents the sampling interval and m the model order.

4.2.2 Time-Varying Transfer Function Methods

Non-Parametric Approaches for Time-varying Transfer Function Estimation

Four methods were used for estimating time-varying transfer functions (TVTF). For the non-parametric methods (FFCDM, CWT, and STFT), TVTF estimation is as follows. The time-varying spectra were computed for the input and output signals (S_X for input spectra, S_Y for output spectra) and the cross-spectrum (S_{XY}) was computed using the codrature and quadrature spectra as in equations 9-10. The co- and quadrature spectra were then smoothed in the temporal and frequency dimensions [26]. CWT spectra were smoothed with an adaptive window relative to the size of the Wavelet at each scale, as described by Torrence *et al.* [21] STFT and FFCDM spectra were smoothed with a boxcar window. Cross-spectra were then computed using equation 11, and TVTFs (HXY) were computed using equation 12.

$$CO_{XY}(t, f) = real\{S_X(t, f)S_Y^*(t, f)\}$$
(9)

$$QU_{XY}(t, f) = -imag\{S_X(t, f)S_Y^*(t, f)\}$$
(10)

$$S_{XY}(t, f) = CO_{XY} - iQU_{XY}$$
(11)

$$H_{XY}(t, f) = \frac{S_{XY}(t, f)}{S_X(t, f)}$$
(12)

VFCDM finds the dominant components of a signal, and creates a line graph where only the most dominant frequencies are present. For transfer function analysis the goal is to understand how the input is modified at all frequencies, therefore only FFCDM was used for TVTF analysis.

Time-varying Optimal Parameter Search

The TVOPS technique for TVTF estimation is an extension of that for time-frequency spectral analysis [10]. Autoregressive, *a*, and moving average, *b*, coefficients as presented in equation 13 are estimated using the TVOPS procedure. The time-varying transfer function gain is then determined using both sets of coefficients in equation 14.

$$y(n) = -\sum_{i=1}^{P} a(i,n)y(n-i) + \sum_{j=0}^{Q} b(n,j)x(n-j) + e(n) \tag{13}$$

$$H(n,f) = \frac{\sum_{j=0}^{Q} b(n,j)\, e^{-i2\pi f j}}{\left|1 + \sum_{k=1}^{m} a(k,n)e^{-i2\pi f k}\right|^2} \tag{14}$$

4.2.3   Test Signals

Comparative Test for Frequency and Amplitude Modulation

Two test signals were designed to test the detection of AM and FM sequences present in renal autoregulation using the time-frequency methods. The first test signal, shown in Eq. (15), contains a low frequency (LF) component at 0.025 Hz, representative of TGF, and a high frequency (HF) component at 0.16 Hz, representative of the MR, which are both constant in amplitude and frequency over 1,000 sec.

$$y(t) = \sin(2\pi * 0.025 * t) + \sin(2\pi * 0.16 * t) \tag{15}$$

This signal was designed to determine a significance threshold for when AM or FM do not exist but may be mistakenly identified by either an influence of the time-frequency method or the background noise. 1,000 realizations of Gaussian white noise (GWN) were added to the signal at signal-noise ratios (SNR) of 0 to 10 dB, in 1 dB increments. For each of the 1,000 realizations at each noise level, the time-frequency representation was generated for the 5 time-frequency methods and a threshold was determined for significant modulation for each time-frequency

47

method. From each time-frequency representation, the maximum amplitude and corresponding frequency at each time instant were extracted within the TGF (0.02 – 0.06 Hz) and MR (0.1 – 0.3 Hz) frequency ranges. These constituted the LF and HF AM and FM sequences. Next, the fast Fourier transform (FFT) was computed for each sequence. Statistical thresholds were computed for each of the 4 sequences (LF-AM, LF-FM, HF-AM, HF-FM), as well as for each noise level, as the mean plus two standard deviations of the FFT magnitudes at each frequency over the 1,000 realizations.

The second test signal was designed to test if the methods detect AM and FM when it exists. This signal contains an LF component at 0.025 Hz and an HF component at 0.16 Hz. The LF component contains AM and FM at a frequency of 0.01 Hz, a frequency previously identified in renal autoregulation [16, 27]. The HF component contains AM and FM at 0.025 Hz, representing the interaction previously shown between TGF and the MR [13]. The expression for the second test signal and corresponding AM and FM components are shown in Eqs. (16a-e).

(16.a)

$$y(t) = \left(1 + \text{AM}_{\text{LF}}(t)\right) * \sin\left(2\pi * 0.025 * t + \text{FM}_{LF}(t)\right) + \cdots$$
$$\left(1 + \text{AM}_{\text{HF}}(t)\right) * \sin\left(2\pi * 0.16 * t + \text{FM}_{\text{HF}}(t)\right)$$

$$\text{AM}_{\text{LF}}(t) = 0.25 * \sin(2\pi * 0.01 * t) \tag{16.b}$$
$$\text{AM}_{\text{HF}}(t) = 0.5 * \sin(2\pi * 0.025 * t)$$
$$\text{FM}_{\text{LF}}(t) = 2\pi * 0.005 * \int_0^t \sin(2\pi * 0.01 * \tau)\, d\tau) \tag{16.c}$$
$$\text{FM}_{\text{HF}}(t) = 2\pi * 0.025 * \int_0^t \sin(2\pi * 0.025 * \tau)\, d\tau) \tag{16.d}$$

(16.e)

GWN was added to the test signal at SNRs from 0 to 10 dB, in 1 dB increments. The time-frequency representations were generated using each of the 5 methods, and AM and FM sequences were extracted as described above for the non-modulated signal. The modulation

frequency was found as the peak FFT magnitude within the frequency ranges of 0.005 – 0.02 Hz for the LF sequences and 0.005 – 0.06 Hz for the HF sequences. Modulation peaks were considered significant if greater than the threshold derived from the non-modulated test signal. This statistical test fixes the probability of detecting a false positive (detecting modulation for a non-modulated signal) at 5%.

If significant modulation was found within the modulated test signal at a frequency within ±0.0025 Hz of the set modulation frequency in (16) a true positive was declared, otherwise a missed detection was declared. The probabilities of detecting a true-positive (PD) were computed for each time-frequency method for AM_{LF}, FM_{LF}, AM_{HF}, and FM_{HF} over 1,000 realizations at each noise level. An example of the test for the detection of modulation is shown in Figure 1.
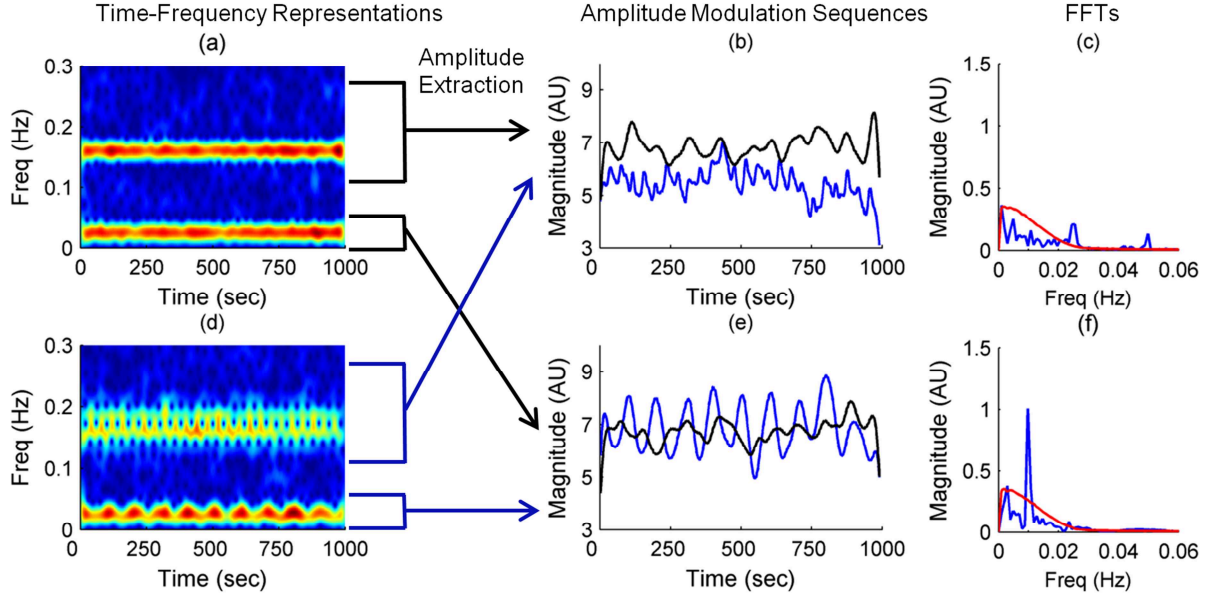
Figure 4.1 - Procedure for detection of amplitude and frequency modulation.
(a) shows the short-time Fourier Transform (STFT) of the non-modulated test signal with GWN added at a signal to noise ratio of 10 dB, the signal contains stationary amplitude and frequency components over time and (d) shows the STFT of the modulated test signal with GWN containing high and low frequency components both with amplitude and frequency modulation. (b) Extracted amplitude sequences from the high frequency region for the non-modulated (black) and modulated (blue) signals. (e) Extracted amplitude sequences from the low frequency region for the non-modulated (black) and modulated (blue) signals. (c) FFT of high frequency amplitude sequence for modulated test signal (blue). Spectral peak at 0.025 Hz on blue represents the frequency of amplitude modulation. For comparison, the high frequency amplitude modulation threshold derived from the non-modulated signal using the STFT with GWN added to the non-modulated signal for 1,000 realizations is shown (red). (f) FFT of low frequency amplitude sequence for modulated test signal (blue). Spectral peak at 0.01 Hz on blue represents the frequency of amplitude modulation for the low frequency component. The threshold derived for the low frequency amplitude modulation is shown (red). The frequency corresponding to the maximum amplitude for the low and high frequency components at each time point is also extracted and the FFT of that sequence is used to determine if frequency modulation exists. This procedure is repeated for each time-frequency representation at SNRs from 0 – 10 dB.

Comparative Test for Identifying Time-Varying Changes in System Gain

A transfer function, represented by the z-transform H(z) in Eq. (17), was designed with an LF (0.04 Hz) and HF (0.18 Hz) peak to represent TGF and the MR, respectively. The parameter A is used to adjust the system gain, shown by the frequency response in Figure 2a.

$$H(z) = A \frac{0.0496z^{-1} - 0.1206z^{-2} + 0.0923z^{-3} - 0.0213z^{-4}}{1 - 2.774z^{-1} + 3.6z^{-2} - 2.727z^{-3} + 0.9727z^{-4}} \tag{17}$$

A 500 sec TVTF was generated by setting a step increase in A at 250 sec, as shown in Figure 2b. TVTFs were designed so that the step increase in gain ranged from 0 to 8 dB in 1 dB increments.

TVTFs were estimated from 1,000 output sequences generated from equation 17 with 1,000 realizations of GWN as the input. The maximum gain within the LF (0.02 – 0.06 Hz) and HF (0.1 – 0.3 Hz) regions were extracted at each time point for each TVTF estimate. A t-test was performed to determine if the gain increase was significant (p<0.05) between the first and last 250 sec. The probability of detecting the change in gain at each step increase was then determined over the 1,000 estimates for each of the four methods.
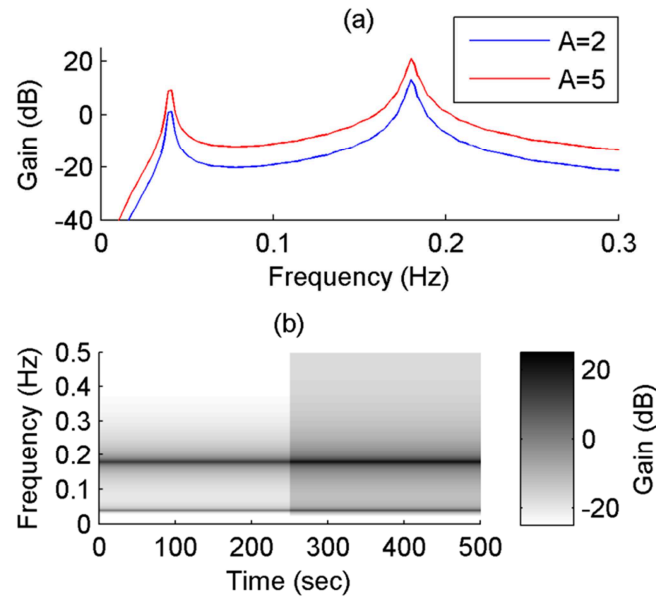
Figure 4.2 - Simulated renal autoregulation transfer function.
(a) Frequency response of the transfer function, H(z), in equation 17 for two different values of the gain parameter A. (b) Time-varying transfer function generated by increasing A at 250 sec.

4.2.4 Renal Autoregulation Data

All experiments were performed at the State University of New York at Stony Brook and approved by the Institutional Research Board (IACUC). Sprague-Dawley rats (SDR, n=7) and spontaneously hypertensive rats (SHR, n=7) were anesthetized with isoflurane (3% intial, 1% maintenance), and then placed on a temperature controlled surgical table to maintain body temperature at 37°C. The left femoral artery was catheterized for measurement of arterial pressure and the left femoral vein was catheterized for saline infusion (PE-50 and PE-10 tubing).

51

The left kidney was isolated and placed in a Lucite cup with a thin plastic film covering the cortical surface to prevent evaporation. A supra-renal aortic clamp was used to control renal perfusion pressure. A laser-Doppler instrument (Transonic, Ithaca, NY) was used to monitor cortical blood flow (CBF) with a blunt 11-gauge needle probe placed on the cortical surface. CBF and BP were recorded continuously during the following protocol: (1) 3 – 5 min spontaneous BP (2) renal arterial pressure was reduced by 20 – 30 mmHg below spontaneous BP by adjusting the aortic clamp (3) CBF was allowed to stabilize at the reduced BP (approximately 1 min) and then the clamp was quickly released (4) CBF and BP were monitored for an additional 3 – 5 min. N^{ω}-nitro-L-arginine methyl ester (L-NAME, Sigma-Aldrich) at 5mg/kg body weight in 5mL normal saline was continuously infused for 1 hour, after which the protocol measurements were repeated with L-NAME present.

CBF and BP data were recorded at 100 Hz (Powerlab, ADInstruments, Mountain View, CA). Data were low-pass filtered with a cutoff frequency of 0.5 Hz to avoid aliasing, and then down-sampled to 1 Hz. Time-frequency spectral (CBF signal) and TVTF (BP as the input signal and CBF as the output signal) methods were applied to the recordings from the entire monitoring protocol after removal of the linear trend. The maximum spectral amplitude and corresponding frequency were extracted for AM and FM detection after release of the aortic clamp from the TFR's for the MR frequencies. Modulation of TGF was not examined due to the 3 – 5 min data length. The maximum gain from the TVTF's was extracted from the 50 sec time point after release of the aortic clamp for the TGF and MR frequencies.

A statistical threshold for modulation was derived for each CBF signal. The SNR for the TGF and Myogenic peaks were determined for each signal from the power spectral density. The TGF power within the range of 0.02 – 0.05 Hz was compared with the power in the assumed

TGF noise region of 0.05 – 0.08 Hz, and the Myogenic power within the range of 0.1 – 0.3 Hz was compared with the power in the assumed Myogenic noise region of 0.3 – 0.5 Hz. A test signal was generated as the sum of two non-modulated sinusoids at the peak TGF and Myogenic frequencies with added GWN and a length equal to that of the data. The power of the TGF and Myogenic peaks relative to the GWN was set to equal the SNR of the data. 1,000 realizations of this signal were generated, and a significance threshold was determined for the mean plus two standard deviations of the FFT of the AM and FM sequences extracted from the TFR's for both frequency ranges. This method tests for modulation in the data compared to a signal without modulation but with the same frequencies, SNR, and data length of the data.

4.2.5 Statistics

Statistical analysis was performed with SigmaStat 3.5 (Systat Software Inc.) with $p<0.05$ considered significant. Renal autoregulation parameters were determined to be non-Gaussian using the Kolmogorov-Smirnov test. Extracted renal autoregulation parameters from after release of the clamp were compared using either the non-parametric Rank Sum test (SDR baseline vs. SHR baseline) or Signed Rank test (SDR baseline vs. SDR during L-NAME). Spearman Rank Order correlation coefficients were used to compare estimated gains between methods.

4.3   Results

4.3.1   Comparison of Methods with Test Signals

Test for Amplitude and Frequency Modulation

Example time-frequency spectra for the modulated signal with added GWN (SNR of 8 dB) for the 5 methods are shown in Figure 3. Only the first 500 sec of the spectra are shown for visualization. Not all methods are able to identify modulation at both LF and HF.
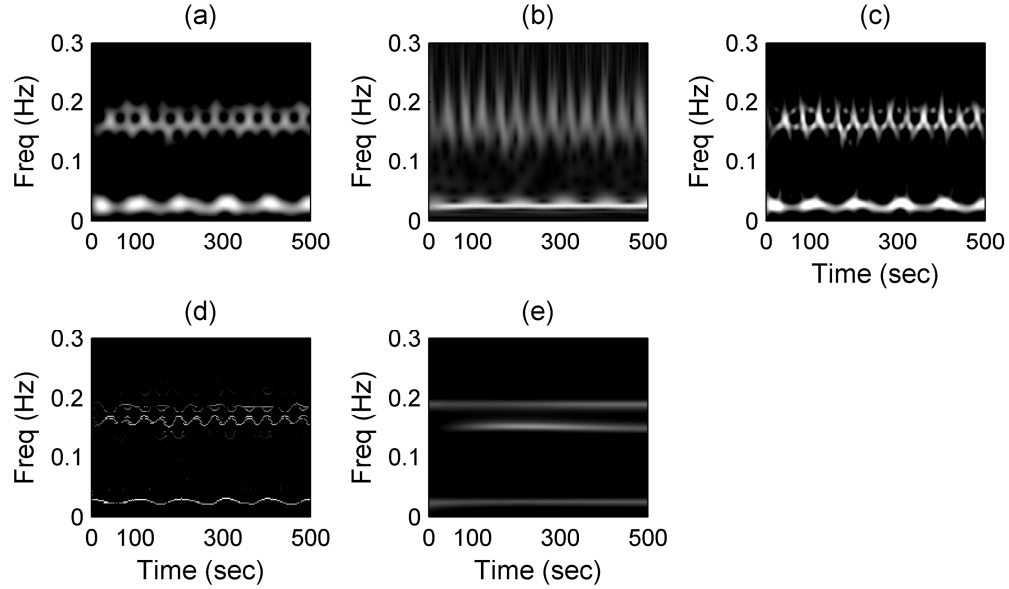
Figure 4.3 - Example time-frequency representations of test signal.
Example time-frequency representations of the modulated test signal with added noise (signal-noise ratio of 8 dB). (a) Short-time Fourier transform, (b) Wavelet transform, (c) smoothed pseudo-Wigner-Ville distribution, (d) variable frequency complex demodulation, (e) time-varying optimal parameter search autoregressive method.

Figure 4 shows the detection probabilities for the modulated test signal at SNRs from 0 to 10 dB. VFCDM, STFT, and SPWV methods had high levels of detection for AM and FM within the LF region across all noise levels. The CWT approach had high detection of modulation within the HF region for low SNR, but the VFCDM method also approached high detection at higher SNR. The TVOPS parametric approach did not accurately identify modulation at any noise level.
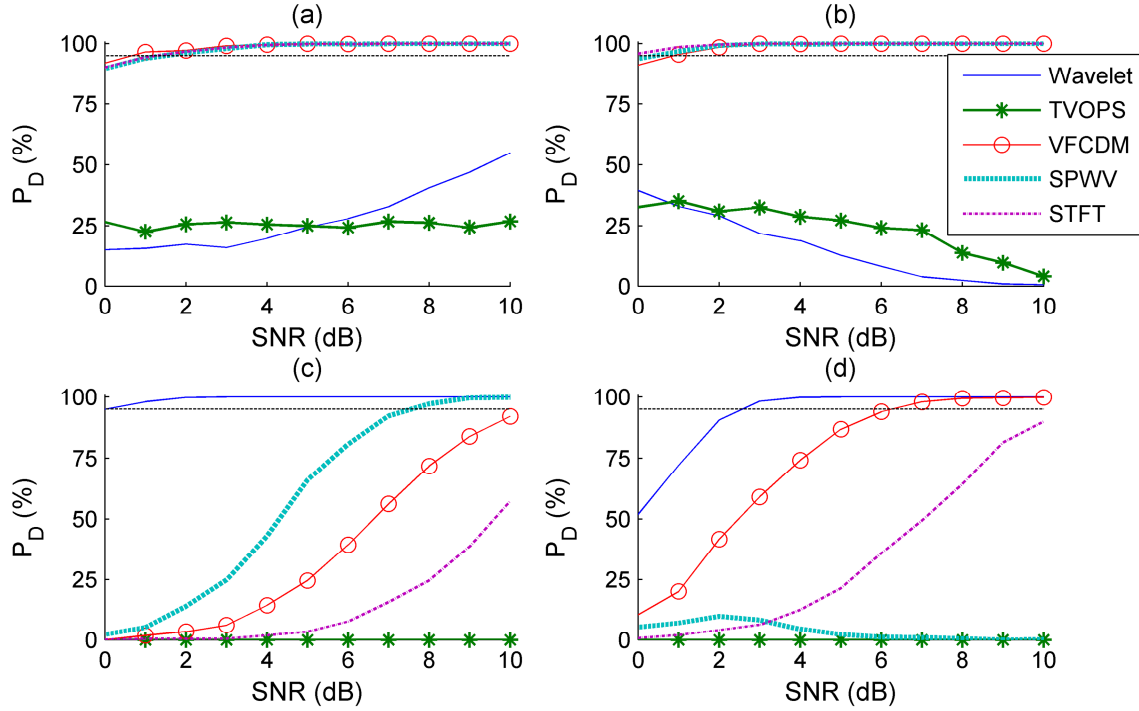
Figure 4.4 - Amplitude and frequency modulation detection results.
Probability of detection (PD) for amplitude or frequency modulation in the simulation signal compared to the threshold levels at signal to noise ratios (SNR) from 0 to 10 dB for five time-frequency methods. (a) Amplitude modulation in the low frequency range, (b) frequency modulation in the low frequency range, (c) amplitude modulation in the high frequency range, (d) frequency modulation in the high frequency range. The dashed black line represents the 95% detection level.

Test for Time-Varying System Gain

Examples of the extracted LF and HF gains averaged over 1,000 realizations are shown in Figure 5a and 5c, respectively, for the estimated TVTFs for an 8 dB step increase in gain at 250 sec. TVOPS accurately estimates the correct gain, while the non-parametric methods underestimate the maximum gain. P_D's for each step increase in gain determined from the 1,000 realizations are presented for the LF and HF gains in Figure 5b and 5d, respectively. In the LF range, the 4 methods have approximately the same P_D at each gain increase. For the HF range, TVOPS had higher P_D than the non-parametric approaches at each step increase in gain.
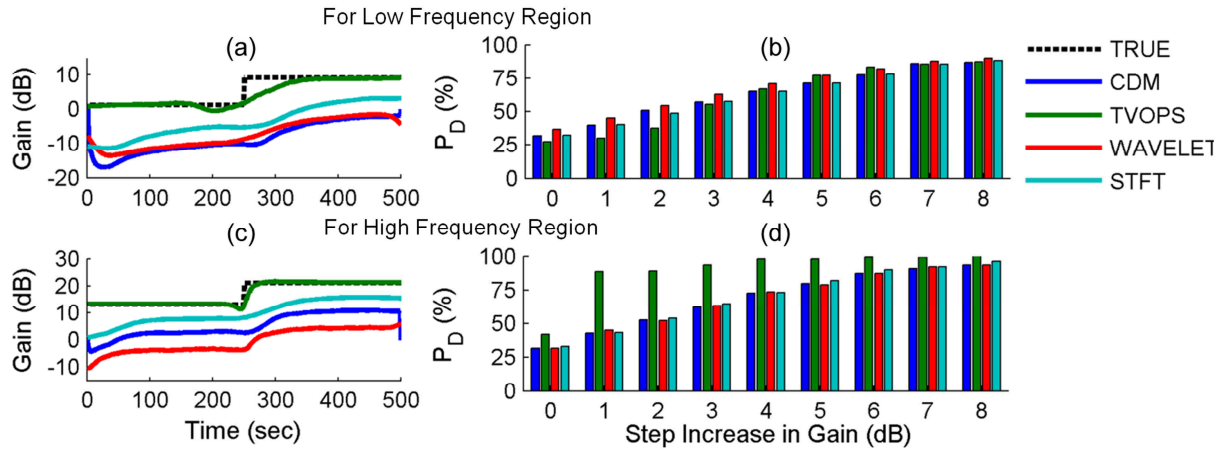
Figure 4.5 - Time-varying gain detection results.
Estimated maximum gains within the low frequency (a) and high frequency (c) regions using the 4 time-varying transfer function methods (mean of 1,000 realizations). (b) Probability of detecting the step increases in gain for the low frequency component over 1,000 realizations of GWN. (d) Probability of detecting the step increases in gain for the high frequency components.

4.3.2 Application to Renal Autoregulation

Detection of Amplitude and Frequency Modulation in Renal Cortical Blood Flow

Figure 6a shows a typical low-pass filtered and down-sampled laser Doppler CBF and arterial BP signal recorded for an SDR after infusion of L-NAME, and the corresponding TFR generated with the VFCDM is shown in Figure 6b.
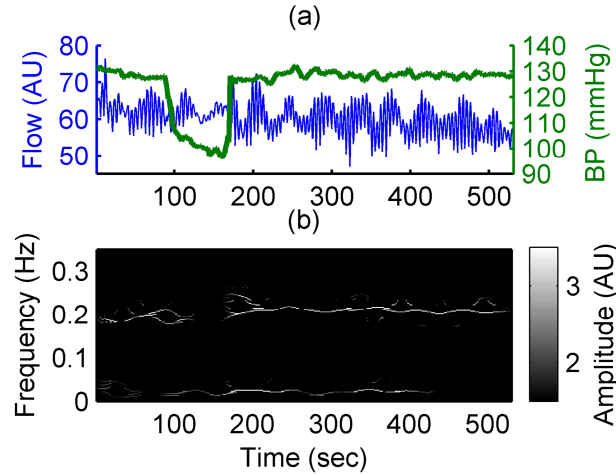
Figure 4.6 - Example laser Doppler data and time-frequency representation.
(a) Example renal data from laser Doppler flow probe (blue) and arterial blood pressure (green) obtained during renal clamping experiment from a Sprague-Dawley rat during infusion of L-NAME. Blood pressure is clamped at approximately 90 sec and held for approximately 90 sec after which the clamp is released. (b) Time-frequency plot generated using variable frequency complex demodulation for flow data in (a) showing the two renal autoregulation dynamics. The myogenic response occurs at approximately 0.2 Hz and TGF occurs at approximately 0.05 Hz.

CBF signals were tested for AM and FM after release of the aortic clamp for the SDR and SHR animals before (baseline) and during L-NAME. Because our simulations showed that only the Wavelet and VFCDM methods reliably detect AM and FM in the MR range, we only present the results for those two methods. The number of signals detected to contain modulation out of the total number tested (7) is shown in Figure 7a for AM and 7c for FM. The frequency at which modulation was detected is presented in Figure 7b and 7d for AM and FM, respectively. AM of the MR was detected during baseline for 4 animals using CWT but was not detected using VFCDM. During L-NAME, modulation was detected for all 7 SDR and 5 out of 7 SHR animals, for both methods. This is in accordance with our simulation results were it was shown that Wavelets had better detection within the HF region at low SNR. The frequency of significant AM ranged from 0.0078 – 0.0244 Hz using CWT and 0.0078 – 0.0498 Hz using VFCDM for SDR, but was limited to 0.0098 – 0.0137 Hz for SHR using both CWT and VFCDM. FM of the MR was detected using either approach, and the frequency detected depended partly upon the

approach used. CWT showed FM at higher frequencies (0.0088 – 0.0352 Hz) than VFCDM (0.0078 – 0.0205 Hz) during L-NAME.
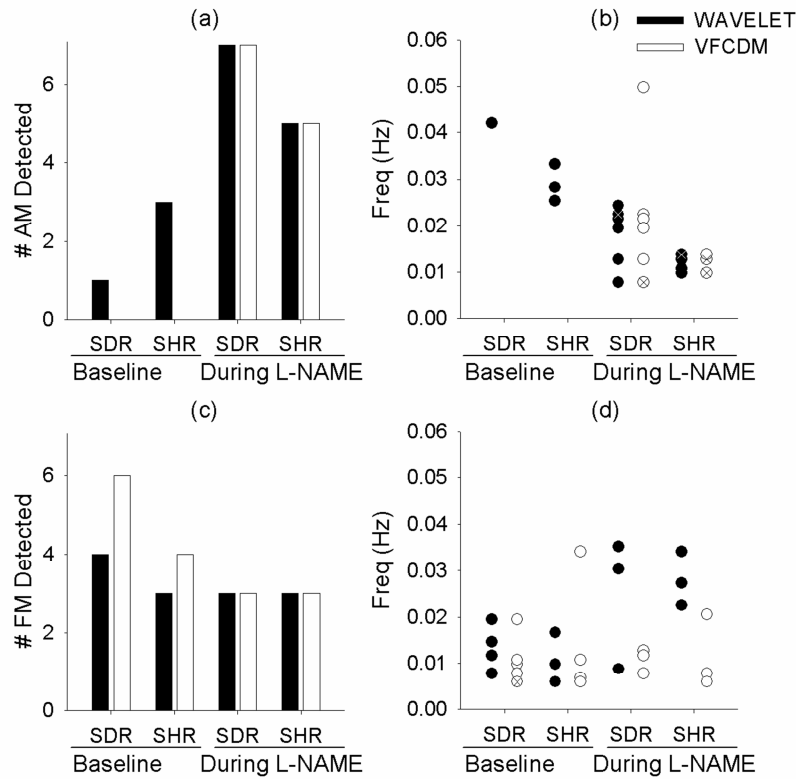
Figure 4.7 - Modulation in experimental data.
(a) Number of experiments with significant myogenic amplitude modulation (out of 7) for SDR and SHR rats after release of the pressure clamp during the baseline condition and during L-NAME. Results are shown for detection with Wavelet (black) and variable frequency complex demodulation (white) time-frequency methods. (b) Frequency at which myogenic amplitude modulation is detected for significant experiments in (a). Each circle represents an animal with significant modulation at that frequency, and an 'x' through the circle represents 2 animals with significant modulation at that frequency. (c) Number of experiments with significant myogenic frequency modulation. (d) Frequency at which the frequency is being modulated at for significant experiments in (c).

Transfer Function Analysis of Renal Blood Flow and Blood Pressure

Examples of the estimated TVTFs from the BP and CBF data in Figure 6a are shown in Figure 8. A peak gain at ~0.2 Hz can be visualized for all four methods corresponding to an MR peak. The TGF peak (~0.05 Hz) strengthens after release of the aortic clamp.
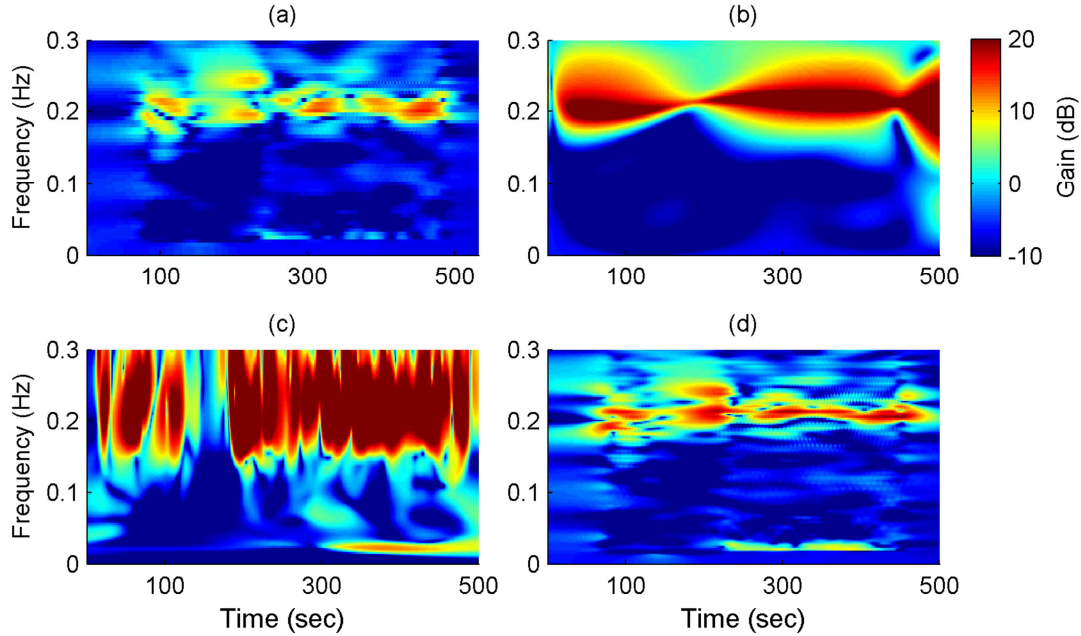
Figure 4.8 - Time-varying transfer functions of laser Doppler flow and arterial pressure data.
(a) fixed-frequency complex demodulation, (b) time-varying optimal parameter search, (c) Wavelet transform, (d) Short-time Fourier transform.

The median and ranges of the gains after release of the aortic clamp using each of the four methods are shown in Table 1. Gain of the MR significantly increased during L-NAME in the SDR group, determined by each of the four methods. The MR gain for SHRs was not significantly different than the SDR gain during baseline for any of the four methods, consistent with previous results [28]. For TGF, SDR gain significantly decreased using the FFCDM method during L-NAME, but was not significantly different using any of the other TVTF methods. SHR animals had significantly reduced TGF peak gain determined by the FFCDM, CWT, and STFT methods, but not TVOPS.

Myogenic

	FFCDM	TVOPS	WAVELET	STFT
SDR – Baseline	1.2	2.7	3.4	4.3
(*n*=7)	-1.6 – 3.5	-1.7 – 5.7	-1.9 – 4.7	0.3 – 6.1
SDR – During L-NAME	8.8 $^\alpha$	16.5 $^\alpha$	19.0 $^\alpha$	13.5 $^\alpha$
(*n*=7)	1.9 – 11.6	12.0 – 33.7	8.6 – 26.1	6.2 – 15.8
SHR – Baseline	-0.05	2.89	0.78	2.9
(*n*=7)	-2.0 – 2.2	-2.0 – 17.0	-1.1 – 17.0	0.1 – 7.3

Tubuloglomerular Feedback

	FFCDM	TVOPS	WAVELET	STFT
SDR – Baseline	-2.7	-6.6	-2.3	-0.6
(*n*=7)	-4.8 – 0.1	-10.0 – 1.7	-8.6 – 4.2	-4.8 – 2.4
SDR – During L-NAME	-4.6 $^\alpha$	-6.74	1.1	-0.9
(*n*=7)	-8.3 – -1.4	-14.0 – -5.8	-12.9 – 8.8	-8.9 – 4.6
SHR – Baseline	-5.5 $^\alpha$	-8.5	-5.2 $^\alpha$	-5.4 $^\alpha$
(*n*=7)	-8.4 – 0.2	-12.1 – 0.6	-9.7 – -2.7	-8.5 – 0.2

Table 4.1 - Experimental transfer function gains.
Estimated transfer function gains (dB) (median, min – max) after release of the clamp for the myogenic and TGF components during baseline and with L-NAME infused. α denotes significance from SDR during baseline conditions, $p < 0.05$.

Spearman Rank Order correlation coefficients estimated for the MR and TGF gains between each pair of methods, Table 2, demonstrate that changes in gain are in accordance between the various methods.

	CDM	TVOPS	WAVELET	STFT
CDM		0.61 $^\alpha$	0.76 $^\alpha$	0.95 $^\alpha$
TVOPS	0.41		0.83 $^\alpha$	0.75 $^\alpha$
WAVELET	0.46 $^\alpha$	0.54 $^\alpha$		0.85 $^\alpha$
STFT	0.81 $^\alpha$	0.50 $^\alpha$	0.82 $^\alpha$	

Table 4.2 - Relationship in gain estimates between methods.
Spearman Rank Order correlation coefficients between the methods for the estimated transfer function peak gains after release of the clamp. The upper triangle (gray) contains the coefficients for the myogenic range, and the lower triangle (white) contains the coefficients for the TGF range. α signifies that the correlation coefficient is significant, $p < 0.05$.

4.4   Discussion

In this study, we investigated analytical methods used for monitoring time-varying renal autoregulation dynamics. Our modulation and time-varying gain tests complement each other in that one is looking for the interaction between autoregulation components [4] and the other is

looking at how the system responds to changes in BP [12]. By detecting multiple properties from the signals we can develop a better understanding of the physical regulation, and in turn how this changes the overall effectiveness of the system. Our test for AM and FM detection showed the VFCDM, STFT, and SPWV to have high PD across noise levels in the LF range, and Wavelet analysis showed the best detection in the HF range across noise levels. The VFCDM produced the best combination of AM and FM detection in the low and high frequency regions. Our test for detecting time-varying changes in system gain showed that the TVOPS estimation technique detected a step increase in gain within the HF region better than the non-parametric methods. These results demonstrate that to fully characterize renal autoregulation a variety of analysis techniques with parameters tuned to the specific component of interest should be used.

We used the same time-frequency analysis parameters for analyzing the MR and TGF frequency ranges. All four non-parametric methods (STFT, CWT, SPWV and VFCDM) identified AM and FM in at least the TGF or MR region for the simulated signals. The difference in the results between the two frequency regions is a function of the selection of the time- and frequency-window settings for each method. For example, by varying the initial parameters that determine the frequency resolution it is possible to alter each method to better identify modulation in the MR and TGF frequency regions. This also implies that using the same parameters for both frequency regions may not be always appropriate. A window containing more samples is required to analyze the TGF than the MR dynamic because TGF operates at a slower frequency. For a window of any given size, more oscillations from the MR will be captured than TGF (since the former has faster frequency dynamics than the latter) and therefore temporal changes will be smoothed at a different rate relative to the oscillation for the two components. Wavelet methods adjust the frequency resolution based on the frequency being

analyzed but concomitantly adjust the temporal resolution. Hence, the Wavelet temporal resolution within the TGF region was not sufficient to identify the temporal changes in the simulated TGF dynamics caused by modulation at 0.01 Hz.

For the SPWV, an AM sequence occurred at an incorrect frequency for the HF region during the modulation test. This resulted in poor detection of the true AM sequence and may be a function of cross terms that exist from the estimation of the SPWV distribution. Increasing the length of the temporal smoothing window will decrease these cross terms but also decrease detection of temporal changes such as modulation. This results in a trade-off between artifacts generated by cross terms and loss of information due to smoothing [22]. TVOPS was not able to resolve the modulation in the spectral analysis because of an insufficient model order. The model order was selected based on optimization for the TVTF analysis, where the TVOPS showed the most accurate results, and was kept constant for the modulation test to show the necessity of selecting the model order based on a particular analysis.

Siu *et al.* used a VFCDM based AM/FM detection procedure to find significant MR modulation by a 0.01 Hz frequency in whole kidney blood flow during telemetric recordings [16]. Sosnovtseva *et al.* used a double Wavelet approach to monitor modulation in tubular pressure of single nephrons, and they initially showed that the MR was modulated by TGF [13, 17, 18]. Later, it was shown that the MR could be modulated by both TGF and a 0.01 Hz frequency [19]. In the present study, we looked for modulation of the MR from 0.005 to 0.06 Hz. We found that the dominant frequency of modulation of MR can range from 0.01 – 0.06 Hz, agreeing with the study by Pavlov *et al.* that the MR amplitude and frequency may be modulated by either a 0.01 Hz mechanism or TGF [19].

Many factors influence the dynamics of renal autoregulation, including nitric oxide (NO) [1]. NO is a vasodilator synthesized by nitric oxide synthase (NOS) from its precursor L-arginine. It plays an important role in regulating glomerular capillary pressure, glomerular plasma flow, and TGF [1]. The role of NO in the control of renal afferent arteriole resistance was studied by Pittner *et al.* [29] using the isolated perfused rat kidney. The afferent arteriole did not autoregulate during the cell-free perfusion of the kidney, however, it did during cell-free perfusion with L-NAME [29]. These results suggest that NO release is related to impaired autoregulation. Since L-NAME is an inhibitor of NOS, we expected enhanced autoregulation [30]. In SDRs, we see that during L-NAME infusion there is an increase in the MR peak gain that is accompanied by significant AM of the MR by either TGF or a 0.01 Hz component. These results agree with those from Shi *et al.* that show augmentation of the MR during inhibition of NOS [30] and Sosnovtseva *et al.* that show increased modulation after infusion of L-NAME [31]. By using analytical methods to detect modulation and track temporal changes in the system gain we are able to identify that changes in the transfer function may be due to changes in the interactions between the MR and TGF. The autoregulation mechanisms are more active after L-NAME [30], so it stands that the interaction between them should be more pronounced given that they both act on the afferent arteriole. It may also represent a change in TGF regulation over the MR after NOS inhibition. Use of multiple analytical methods allows us to better understand how interactions between the MR and TGF may contribute to the overall effectiveness of renal autoregulation.

Without examining coherence we cannot say if changes in transfer function gain of the CBF oscillations are caused by a linear transformation of the input BP signal, as coherence determines the confidence of the transfer function analysis [32]. Coherence has been repeatedly

studied in renal autoregulation [1, 7, 10, 12, 30, 33]. The frequency region >0.1 Hz, containing the Myogenic response, has been reported to have high coherence showing that the Myogenic response is a direct consequence of changes in blood pressure [30, 33]. Time—invariant coherence is often shown to be low in the TGF frequency range [12], contributing to the concept that TGF can be driven by either non-linear self-sustained oscillations or time-varying dynamics [34]. Using time-varying approaches directly accounts for the contribution of non-stationarity as we are now able to look at specific time points when time-varying coherence may be high or low and treat the transfer function results appropriately [12]. In the present study, we did not examine coherence, and the transfer function gain results should be interpreted with this in mind.

We have compared a number of time-varying analysis methods, and it is clear that a single method with fixed parameters cannot uncover all the complex characteristics of the MR and TGF. If one is interested in determining modulation of the dynamics over time between the two control systems, it may be best to use a non-parametric method with settings not fixed for the MR and TGF regions but instead set for each as appropriate. Alternatively, a parametric method such as TVOPS might be the most appropriate for accurate estimation of temporal changes in transfer functions to describe how the system alters its response to BP over time [12]. In this study, we limited our comparisons to AM and FM phenomena and time-varying changes in system gain, but the same type of quantitative comparisons could be made for additional parameters of interest such as coherence and phase relationships.

4.5   Acknowledgements

64

4.6   References

[1]   Cupples, W.A. and B. Braam. Assessment of renal autoregulation. *American Journal of Physiology. Renal Physiology*. 292:F1105-F23, 2007.

[2]   Yip, K.P., N.H. Holstein-Rathlou and D.J. Marsh. Mechanisms of temporal variation in single-nephron blood flow in rats. *American Journal of Physiology. Renal Physiology*. 264:F427-F34, 1993.

[3]   Marsh, D.J., I. Toma, O.V. Sosnovtseva, J. Peti-Peterdi and N.-H. Holstein-Rathlou. Electrotonic vascular signal conduction and nephron synchronization. *American Journal of Physiology. Renal Physiology*. 296:F751-F61, 2009.

[4]   Chon, K.H., R. Raghavan, Y.-M. Chen, D.J. Marsh and K.-P. Yip. Interactions of TGF-dependent and myogenic oscillations in tubular pressure. *American Journal of Physiology. Renal Physiology*. 288:F298-F307, 2005.

[5]   Cupples, W.A. Interactions contributing to kidney blood flow autoregulation. *Current Opinion in Nephrology and Hypertension.* 16:39-45, 2007.

[6]   Sosnovtseva, O.V., A.N. Pavlov, E. Mosekilde and N.H. Holstein-Rathlou. Bimodal oscillations in nephron autoregulation. *Physical Review E*. 66:061909, 2002.

[7]   Bidani, A.K., R. Hacioglu, I. Abu-Amarah, G.A. Williamson, R. Loutzenhiser and K.A. Griffin. "Step" vs. "dynamic" autoregulation: implications for susceptibility to hypertensive injury. *American Journal of Physiology. Renal Physiology*. 285:F113-F20, 2003.

[8]   Cupples, W.A., P. Novak, V. Novak and F.C. Salevsky. Spontaneous blood pressure fluctuations and renal blood flow dynamics. *American Journal of Physiology. Renal Physiology*. 270:F82-F89, 1996.

[9]   Zou, R., W.A. Cupples, K.R. Yip, N.H. Holstein-Rathlou and K.H. Chon. Time-varying properties of renal autoregulatory mechanisms. *Biomedical Engineering, IEEE Transactions on*. 49:1112-20, 2002.

[10]   Zhao, H., S. Lu, R. Zou, K. Ju and K. Chon. Estimation of time-varying coherence function using time-varying transfer functions. *Annals of Biomedical Engineering*. 33:1582-94, 2005.

[11]   Zhao, H., W.A. Cupples, K.H. Ju and K.H. Chon. Time-varying causal coherence function and its application to renal blood pressure and blood flow data. *Biomedical Engineering, IEEE Transactions on*. 54:2142-50, 2007.

[12]   Chon, K.H., Y. Zhong, L.C. Moore, N.H. Holstein-Rathlou and W.A. Cupples. Analysis of nonstationarity in renal autoregulation mechanisms using time-varying transfer and coherence functions. *American Journal of Physiology. Regulatory, Integrative and Comparative Physiology*. 295:R821-R28, 2008.

[13]   Sosnovtseva, O.V., A.N. Pavlov, E. Mosekilde, N.H. Holstein-Rathlou and D.J. Marsh. Double-wavelet approach to study frequency and amplitude modulation in renal autoregulation. *Physical Review E*. 70:031915, 2004.

[14]   Sosnovtseva, O.V., A.N. Pavlov, E. Mosekilde, K.-P. Yip, N.-H. Holstein-Rathlou and D.J. Marsh. Synchronization among mechanisms of renal autoregulation is reduced in hypertensive rats. *American Journal of Physiology. Renal Physiology*. 293:F1545-F55, 2007.

[15]   Raghavan, R., X. Chen, K.-P. Yip, D.J. Marsh and K.H. Chon. Interactions between TGF-dependent and myogenic oscillations in tubular pressure and whole kidney blood flow in both SDR and SHR. *American Journal of Physiology. Renal Physiology*. 290:F720-F32, 2006.

[16]   Siu, K.L., B. Sung, W.A. Cupples, L.C. Moore and K.H. Chon. Detection of low-frequency oscillations in renal blood flow. *American Journal of Physiology. Renal Physiology*. 297:F155-F62, 2009.

[17]   Marsh, D.J., O.V. Sosnovtseva, A.N. Pavlov, K.-P. Yip and N.-H. Holstein-Rathlou. Frequency encoding in renal blood flow regulation. *American Journal of Physiology. Regulatory, Integrative and Comparative Physiology*. 288:R1160-R67, 2005.

[18]   Sosnovtseva, O.V., A.N. Pavlov, E. Mosekilde, N.-H. Holstein-Rathlou and D.J. Marsh. Double-wavelet approach to studying the modulation properties of nonstationary multimode dynamics. *Physiological Measurement*. 26:351, 2005.

[19]   Pavlov, A.N., O.V. Sosnovtseva, O.N. Pavlova, E. Mosekilde and N.-H. Holstein-Rathlou. Characterizing multimode interaction in renal autoregulation. *Physiological Measurement.* 29:945, 2008.

[20]   Wang, H., K.L. Siu, K. Ju and K.H. Chon. A high resolution approach to estimating time-frequency spectra and their amplitudes. *Annals of Biomedical Engineering*. 34:326-38, 2006.

[21]   Torrence, C. and G.P. Compo. A practical guide to wavelet analysis. *Bulletin of the American Meteorological Society*. 79:61-78, 1998.

[22]   Hlawatsch, F. and G.F. Boudreaux-Bartels. Linear and quadratic time-frequency signal representations. *Signal Processing Magazine, IEEE*. 9:21-67, 1992.

[23]   Powers, E.J., H.S. Don, J.Y. Hong, Y.C. Kim, G.A. Hallock and R.L. Hickok. Spectral analysis of nonstationary plasma fluctuation data via digital complex demodulation. *Review of Scientific Instruments*. 59:1757-59, 1988.

[24]   Zou, R., H. Wang and K.H. Chon. A robust time-varying identification algorithm using basis functions. *Annals of Biomedical Engineering*. 31:840-53, 2003.

[25]   Sheng, L., J. Ki Hwan and K.H. Chon. A new algorithm for linear and nonlinear ARMA model parameter estimation using affine geometry [and application to blood flow/pressure data]. *Biomedical Engineering, IEEE Transactions on*. 48:1116-24, 2001.

[26]   Whitcher, B., P.F. Craigmile and P. Brown. Time-varying spectral analysis in neurophysiological time series using Hilbert wavelet pairs. *Signal Processing*. 85:2065-81, 2005.

[27]   Just, A. and W.J. Arendshorst. Dynamics and contribution of mechanisms mediating renal blood flow autoregulation. *American Journal of Physiology. Regulatory, Integrative and Comparative Physiology*. 285:R619-R31, 2003.

[28]   Wang, X. and W.A. Cupples. Interaction between nitric oxide and renal myogenic autoregulation in normotensive and hypertensive rats. *Canadian Journal of Physiology and Pharmacology*. 79:238-45, 2001.

[29]   Pittner, J., M. Wolgast, D. Casellas and A.E.G. Persson. Increased shear stress-released NO and decreased endothelial calcium in rat isolated perfused juxtamedullary nephrons. *Kidney International*. 67:227-36, 2005.

[30]   Shi, Y., X. Wang, K.H. Chon and W.A. Cupples. Tubuloglomerular feedback-dependent modulation of renal myogenic autoregulation by nitric oxide. *American Journal of Physiology. Regulatory, Integrative and Comparative Physiology*. 290:R982-R91, 2006.

[31]   Sosnovtseva, O.V., A.N. Pavlov, O.N. Pavlova, E. Mosekilde and N.H. Holstein-Rathlou. The effect of L-NAME on intra- and inter-nephron synchronization. *European Journal of Pharmaceutical Sciences.* 36:39-50, 2009.

[32]   Pinna, G. and R. Maestri. Reliability of transfer function estimates in cardiovascular variability analysis. *Medical and Biological Engineering and Computing*. 39:338-47, 2001.

[33]   Pires, S.L.S., C. Barrès, J. Sassard and C. Julien. Renal Blood Flow Dynamics and Arterial Pressure Lability in the Conscious Rat. *Hypertension*. 38:147-52, 2001.

[34]   Holstein-Rathlou, N.H., A.J. Wagner and D.J. Marsh. Tubuloglomerular feedback dynamics and renal blood flow autoregulation in rats. *American Journal of Physiology. Renal Physiology*. 260:F53-F68, 1991.

Chapter 5: Detecting Physiological Systems with Laser Speckle Perfusion Imaging of the Renal Cortex

5.1   Introduction

At least 5 dynamics generated by various physiological systems are present within renal blood flow, and measured perfusion signals can be used to study the systems and the interactions between them [1, 2]. The 5 dynamics include global signatures generated outside the kidney such as flow pulse representing the heart rate (HR), respiratory-induced oscillations (RO), and baroreflex components (BRC) generated in the mesenteric circulation [3] as well as the local renal autoregulation signatures generated within the renal vasculature including the myogenic response (MR) and tubuloglomerular feedback (TGF). Each of the 5 systems operates within a distinct frequency range, Table 1, and using spectral analysis the slower renal autoregulation signatures can be separated from the faster global signatures.

	f_1 (Hz)	f_2 (Hz)
Tubuloglomerular feedback (TGF)	0.02	0.05
Myogenic response (MR)	0.1	0.3
Baroreflex component (BRC)	0.35	0.7
Respiratory oscillations (RO)	0.8	1.2
Heart rate (HR)	4	7

Table 5.1 - Frequency bands for physiological systems

Dynamics are identified in total renal blood flow (RBF) signals from transit time ultrasound measurements at the renal artery, in which the dynamics from ~30,000 nephrons are averaged together, or from single laser Doppler or tubule pressure recordings providing information from a single point on the surface or in a single nephron [2, 4, 5]. However, it has been shown in experimental as well as modeling studies that nephron dynamics are not

homogenous, and attributes of synchronization and coupling between nephrons are missed using the univariate measurements such as total RBF or tubule pressure [6-8].

Laser speckle perfusion imaging (LSPI) measures perfusion changes at points within an imaging window with high temporal and spatial resolution and has found success in imaging skin, cerebral, and renal vascular beds [9-12]. In LSPI, a speckle pattern is generated by imaging a laser-illuminated surface. Red blood cells act as scatterers and blur the pattern, allowing quantification of perfusion changes in the imaged region from the captured pixel statistics. Bezemer *et al.* demonstrated that during occlusion of the renal artery, changes in RBF could be observed using LSPI and spatial heterogeneity in renal perfusion was identified [12]. Recently, there has been increasing interest in processing LSPI sequences to monitor dynamic changes in vascular perfusion signals [10]. Analysis on single laser speckle signals has shown that time-series extracted from individual pixels do not match those of laser Doppler flowmetry, but by increasing the number of pixels averaged to determine a perfusion index the properties could become usable much the same way laser Doppler flowmetry has been used to monitor single point dynamics [13, 14]. Bricq *et al.* showed the cardiac pulse in forearm blood flow could effectively be monitored within an LSPI imaging window by increasing the number of pixels averaged [9]. In renal perfusion, Holstein-Rathlou *et al.* investigated synchronization in TGF dynamics between LSPI signals extracted from nephron locations identified by imaging the vasculature [6].

In this study, we investigate if signals acquired from points on the renal cortex using LSPI contain information pertaining to renal perfusion dynamics beyond that acquired from RBF measurements in anaesthetized rats. We hypothesize that dynamics related to the cardiac pulse, respiratory-induced oscillations, and baroreflex oscillations generated outside of the kidney will

correlate with RBF and be homogenous across the renal cortex whereas renal autoregulation dynamics will demonstrate spatial variance because they are generated locally. In addition, we compare transfer function analysis under forced blood pressure during intrarenal infusions to enhance and inhibit renal autoregulation.

5.2   Materials and Method

5.2.1   Experiments

All experiments were approved by the Animal Care Committee of Simon Fraser University, in accordance with the guidelines of the Canadian Council on Animal Care. Male Long-Evans rats (Harlan, Livermore, CA, USA), aged 10-14 weeks, were housed in pairs and given standard chow and distilled water ad libitum prior to the experiment. Twenty minutes prior to each experiment, the rat was given buprenorphine (0.02 mg/kg i.p.). Anaesthesia was induced with 4% isoflurane in inspired gas (30% O2, 70% air, 750mL/min) and reduced to 2% thereafter. Animals were placed on a heated table (35°C) to maintain body temperature. The trachea was cannulated and animals were ventilated by a small animal respirator (TOPO, Kent Scientific, Torrington, CT, USA) operating in timed respiration mode and adjusted to match the natural breathing rate of each animal (~60 breaths per minute). The left femoral vein was cannulated (PE-50) for infusion of saline containing 2% bovine serum albumin (1% body weight per hour) to replace surgical volume losses. The left femoral artery was cannulated (PE-90 with narrowed tip) and connected to a pressure transducer (TRN050) and amplifier (TRN005, Kent Scientific, Torrington, CT, USA) for blood pressure (BP) measurements. The left kidney was exposed by a subcostal flank incision. Once freed from surrounding fat, the kidney was mounted in a plastic cup anchored to the table. Stopcock grease (Dow Corning, Midland, MI, USA) was placed in the

69

cup to prevent motion and position the kidney towards the LSPI camera. The renal artery was stripped of fat and renal nerves. A Teflon cannula tip was inserted in the left femoral artery and then positioned in the renal artery for intrarenal infusions. RBF was measured with a transit time ultrasound flow probe (TS420, Transonic Systems, Ithaca, NY, USA) mounted on the renal artery and secured with acoustic coupling gel (Surgilube and Nalco 1181). There was a 1-hr post-surgery equilibration period during which the anaesthetic concentration was reduced to ~1.5% or the lowest concentration that prevented responses to toe-pinching.

Experiments were performed during spontaneous BP fluctuations (N=7) and, on a separate set of animals, during broad band forcing of BP (N=8). For the BP forcing experiments, a motorized occluder was placed around the aorta above the left renal artery. The occluder was controlled by a program in Matlab, in the same manner as a previous reported system [2]. The program drops renal perfusion pressure to a set pressure ~10% below spontaneous BP, and the pressure is then randomly changed by ±5% at 2 Hz iterations by adjusting the occluder throughout the forcing measurement period.

RBF and BP measurements were recorded continuously at 500 Hz. 25 min LSPI measurements were made during control (CTL) conditions. Intrarenal infusion of the non-selective nitric oxide synthase inhibitor Nω-nitro-l-arginine methyl ester (L-NAME) (Sigma-Aldrich, Oakville, ON, Canada) was then initiated at 10 µg/min for 20 min followed by 3 µg/min. After an ~25 min waiting period, another recording (L-NAME) was made. Next, the rho-kinase inhibitor Y-27632 (Cedarlane Labs, Burlington, ON, CA) [15] was infused intrarenally to achieve 10µmol/L in RBF [2], and after another ~25 min waiting period a final 25 min measurement (Y) was made.

70

LSPI was performed with the moorFLPI laser speckle contrast imager (Moor Instruments, Axminster, UK) with an increased optical zoom and exposure time set to 2 msec. The moorFLPI illuminates the target surface with a 775 nm laser and captures the resulting speckle image with a 568x760 pixel CCD camera at a sampling rate of 25 Hz. The moorFLPI has the option of computing perfusion images by determining the statistics of a set of pixels over either temporal or spatial dimensions. We used a spatial set of pixels resulting in perfusion images sized 113x152 pixels at a sampling rate of 25 Hz (statistics computed for 5x5 squares of pixels at each frame). The moorFLPI translates the speckle contrast value into a relative perfusion unit termed flux. Assuming red blood cells are the primary source of motion in the kidney, a higher flux corresponds to increased velocity and/or concentration of red blood cells. Prior to each 25 min recording period, an ~4 mm hair was placed on the renal surface, and the moorFLPI was positioned to include the full hair in the viewing window resulting in the lens being ~20 cm from the renal surface. Recorded images of the hair were used to estimate the physical pixel size. A black out curtain was positioned around the experimental area to block interference from ambient light.

5.2.2   Data Analysis

moorFLPI sequences were loaded into Matlab r2011b (The Mathworks, Natick, MA, USA) and a mask was drawn around any surface objects to ignore during analysis. To align LSPI sequences with RBF and BP measurements, RBF signals were low-pass filtered using a forwards-backwards non-causal filter to 12.5 Hz and down-sampled to 25 Hz, matching that of the laser speckle signals. Mean laser speckle flux and RBF signals were then aligned by cross-correlation.

5.2.3 Identifying the Physiological Systems

For the dataset recorded during spontaneous BP fluctuations, the power spectrum of the 25 Hz signals was computed using Welch's periodogram method with 8192 sample segment size and 50% overlap after linearly detrending the signals. Identification of the operating frequency of 5 physiological mechanisms was determined by finding the maximum amplitude from the power spectrum within the relevant frequency range (Table 1).

LSPI sequences were spatially filtered using a Gaussian filter (σ = 3.12), to improve signal-noise ratios at each pixel [9]. The 4 exterior pixels around the edge of the image were removed after filtering because of edge effects caused by the filtering process. Because high resolution spatial features are removed by the Gaussian filters, the filtered images were spatially down-sampled by a factor of 4 resulting in 27x37 pixel resized image sequences at 25 Hz. Power spectra of extracted time-series from each pixel were computed and peak frequencies identified within each frequency region. This produced surface maps of the peak frequency at each pixel within each dynamic range. The coefficient of variation (*CV*) was computed as the standard deviation (σ) over the mean (μ) of the peak frequencies across the entire surface as a measure of surface heterogeneity. To account for variations in sizes of the 5 frequency bands, *CV* was normalized by the theoretical *CV* of a uniform distribution over each frequency band (f_1 to f_2) as derived in Appendix A, denominator in Eq. 1.

$$CV_{norm} = \frac{CV}{\frac{(f_2 - f_1)}{\sqrt{3}(f_2 + f_1)}} \tag{1}$$

A *CV_norm* close to 1 represents a uniform distribution of frequencies across the specified range.

The error of peak frequency estimates from LS_{mean} relative to RBF estimates was determined by computing the relative percent error between them, Eq. 2.

$$Percent\ Error = \frac{|f_{LS} - f_{RBF}|}{f_{RBF}} \times 100 \qquad (2)$$

5.2.4 Functional Analysis

The dataset recorded during broad-band forcing of BP was used to characterize the functional aspects of renal autoregulation. Signals were band-pass filtered between 0.004 and 1 Hz using a forwards-backwards non-causal elliptic filter and down-sampled to 2 Hz. Transfer function and mean-squared coherence estimates were computed using Welch's periodogram method using a 512 sample segment size with 50% overlap. Transfer functions were computed for each experiment with BP as the input and either RBF or LS_{mean} (spatial average at each frame) as the output.

To quantify functional aspects of renal autoregulation, 4 parameters were computed from the transfer function and coherence estimates. The mean coherence between $0.05 - 0.08$ Hz was used as a measure of the non-linearity between the flow and BP measurements [2]. Mean gain in the low frequency region ($0.005 - 0.02$ Hz) represents the ability of renal autoregulation to reduce BP fluctuations in the flow signals. The slope computed from $0.05 - 0.15$ Hz represents the gain reduction from high to low frequencies, and the phase angle at 0.1 Hz describes the delay between frequencies in BP and those in flow signals at this frequency. Although the specific frequencies of operation may vary from animal to animal, we utilized strict frequency limits to perform pixel-by-pixel analysis from LSPI measurements.

5.2.5 Time-varying Transfer Functions

Time-varying transfer functions were determined with continuous Wavelet transforms to determine temporal changes in renal autoregulation function. Signals were first passed through a 500 sec moving average filter to remove slow changes in the mean during the infusions. The

wavelet transform ($W(t,s)$), Eq. 3, was found for both input (BP) and output (perfusion) signals by convolution with a zero-mean Morlet wavelet function, ψ, Eq. 4, that is dilated across scales, s, and shifted across time. The Morlet wavelet was set with a center frequency, ω_o, of 6.

$$W(t,s) = \frac{1}{\sqrt{s}} \int_{-\infty}^{\infty} x(\tau)\psi^* \left(\frac{\tau - t}{s}\right) d\tau \tag{3}$$

$$\psi(t) = \pi^{-1/4} e^{i\omega_o t} e^{-t^2/2} \tag{4}$$

To compute transfer function characteristics, the co- (Eq. 5) and quadrature (Eq. 6) spectra were determined with W_x (input signal Wavelet transform) and W_Y (output signal Wavelet transform). An adaptive smoothing procedure was used to smooth the Wavelet transforms co- and quadrature spectra [16]. The cross-spectrum was determined as Eq. 7, and the time-varying transfer function, used to find system gain and phase angle, and the time-varying coherence function were determined using Eqs. 8 and 9, respectively [17].

$$CO_{XY}(t,f) = real\{W_X(t,f)W_Y^*(t,f)\} \tag{5}$$

$$QU_{XY}(t,f) = -imag\{W_X(t,f)W_Y^*(t,f)\} \tag{6}$$

$$W_{XY}(t,f) = CO_{XY} - iQU_{XY} \tag{7}$$

$$H_{XY}(t,f) = \frac{W_{XY}(t,f)}{W_X(t,f)} \tag{8}$$

$$C_{XY}(t,f) = \frac{|W_{XY}(t,f)|^2}{W_X(t,f)W_Y(t,f)} \tag{9}$$

Data are displayed as mean ± standard error (SE). Statistical analysis was performed using SPSS Statistics 17.0. CV_{norm} values were compared using two-way repeated measures ANOVA across experimental conditions and the five frequency bands. Differences in the transfer function parameters between infusion periods were analyzed with one-way repeated

measures ANOVA (with Greenhouse-Geiser correction if failed sphericity assumption). The Sidak post-hoc test was used for pairwise comparisons (P<0.05 considered significant).

5.3   Results

Using the 4mm hair measurement, the size of a single pixel was measured as 37 ± 6 μm and 41 ± 3 μm on a side for the spontaneous and forcing datasets, respectively, and after spatially filtering and down-sampling pixel sizes were 150 ± 9 μm and 163 ± 12 μm. The sizes of the imaged regions were ~4.2 x 5.6 mm and ~4.6 x 6.2 mm for the spontaneous and forcing data sets, respectively. A series of flux images is output from the moorFLPI where the value at each pixel location is a relative perfusion index. Fig. 1a shows an example renal perfusion image for the mean over the entire record at each pixel. High and low areas of perfusion can be identified, and high flux areas likely correspond to individual nephrons [6]. Time-series extracted from individual pixels contain significant noise (gray line in Fig. 1d&e), but by averaging pixels together the noise can be reduced as shown by the blue line in Fig. 1d&e which corresponds to a 3x3 pixel average [9]. In the 3x3 pixel average the background noise across all frequencies is reduced, but the signatures of the dynamics are still buried within the noise. Fig. 1b shows the same renal perfusion image as in Fig. 1a after applying the Gaussian spatial filter across each frame, and the time-series extracted from the same pixel have noise significantly reduced noise from the unfiltered perfusion series as well as the 3x3 pixel average, Figs. 1d&e. The Gaussian spatial filter blurs the renal surface, so the series are down-sampled to reduce redundant analysis, Fig. 1c. Subsequent analysis performed on a pixel-by-pixel basis uses the down-sampled Gaussian spatial filter series. Single signal analysis with LS_{mean}, red line in Fig. 1d&e, was used to compare with RBF signals.
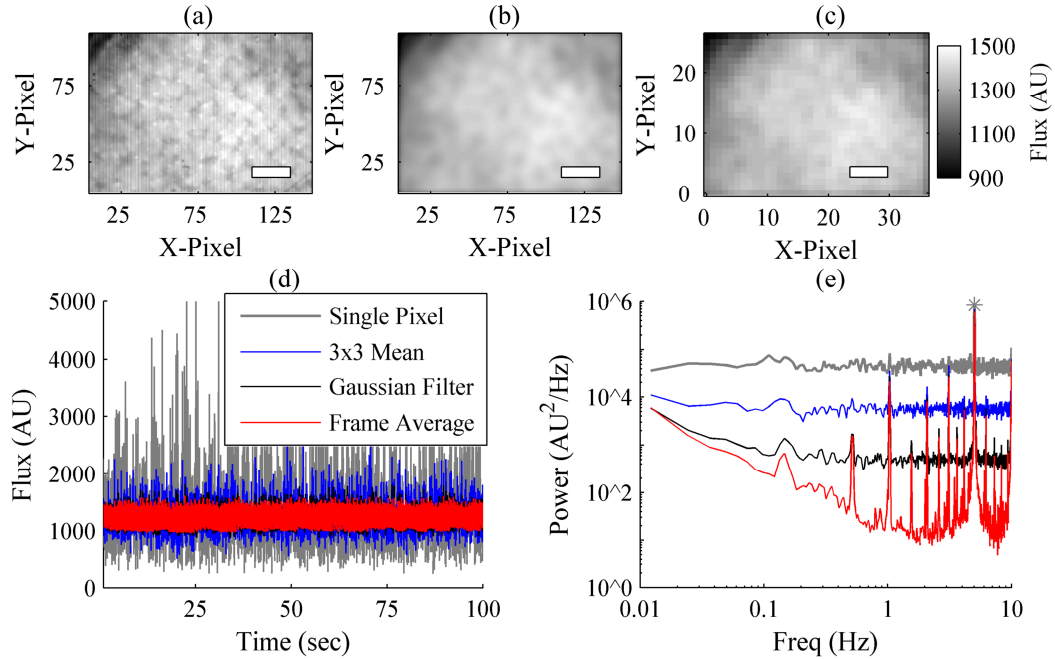
Figure 5.1 - Laser speckle imaging of the renal cortex.
(a) Flux image obtained by averaging the time-series at each pixel. The white rectangle is 1 mm long. (b) Flux image after applying the Gaussian spatial filter at each frame. (c) Flux image after spatially down-sampling the spatially filtered series at each frame. (d) 100 sec of signals extracted from the flux image series. The gray line represents the time-series extracted from a single pixel, the blue line is a 3x3 pixel average around the same pixel, the black line is the pixel time-series after applying the spatial filter at each frame, and the red line is the average of all pixels within each frame. (e) Power spectra of the signals in (d). Beyond the cardiac component (identified by the gray star on the single pixel spectrum), no frequencies can be identified above the noise level from the time-series extracted from the single pixel. Noise is reduced by taking a 3x3 pixel average, and further reduced with additional signals appearing after applying the Gaussian spatial filter. Noise continues to diminish by averaging the entire frame.

5.3.1 Identification of Physiological Components

Example spectra of total BP, RBF, and LS$_{mean}$ are shown in Fig. 2a,b&c, respectively, during CTL, L-NAME, and Y-27632 conditions under spontaneous BP. Many frequencies can be identified from the signals, with respiratory related oscillations (RO) and heart rate (HR) components at the high frequency end (with respiration harmonics > 1 Hz due to mechanical ventilation also present). Baroreflex components (BRC) (~0.4 Hz) [3] are present during CTL and L-NAME conditions in all three signals but are not present during Y-27632. Frequencies in the MR range (>0.1 Hz) appear only on the RBF and LS spectra during CTL and L-NAME and are not apparent after infusion of the rho-kinase inhibitor, showing that the MR is an active

76

component in the renal vasculature. During Y-27632, low frequency power increased, due to a lack of autoregulation. RBF and LS$_{mean}$ spectra are similar in the high frequency ranges containing the global parameters, but at the low frequency band spectral differences exist in the MR and TGF characteristics.
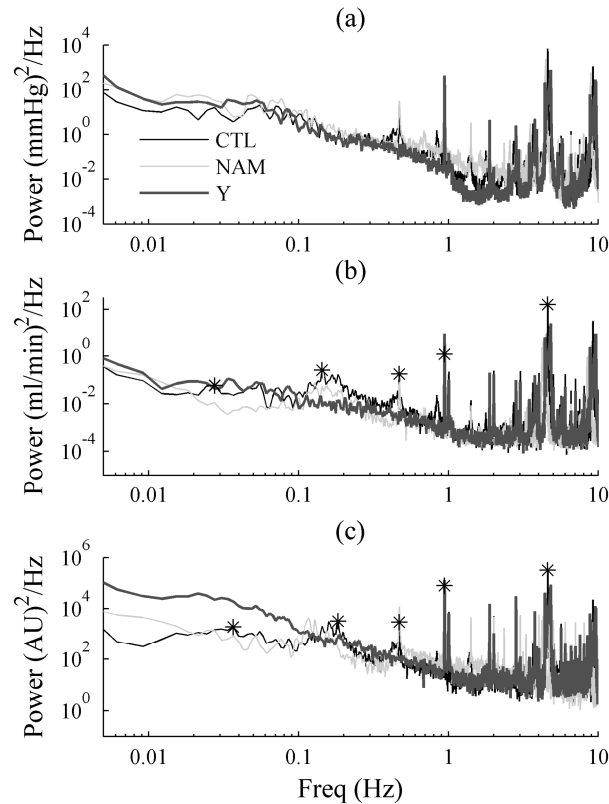
Figure 5.2 - Frequency spectra during three conditions.
Power spectra for (a) blood pressure, (b) renal blood flow, and (c) laser speckle flux signals acquired during control (CTL, black), L-NAME infusion (NAM, light gray), and Y-27632 infusion (Y, thick dark gray). 5 frequency peaks are noted by the black stars on the CTL spectra for renal blood flow and laser speckle flux: the highest magnitude frequency (~5 Hz) corresponds to the cardiac pulse and at ~1 Hz is the frequency associated with respiratory oscillations. The peak at ~0.4 Hz corresponds to a baroreflex signature. Renal autoregulation mechanisms have frequencies at ~0.15 Hz and ~0.03 Hz for the myogenic response and tubuloglomerular feedback, respectively. Peaks within the same frequency ranges can be identified in renal blood flow and laser speckle flux spectra.

Peak frequencies were identified for each region during CTL and L-NAME conditions, Y-27632 period was not included since vasomotion was not apparent and no dominant frequency could be identified for TGF and the MR during this period. Identified frequencies from RBF and LS$_{mean}$ were compared within each frequency range, Fig. 3. BRC, RO, and HR frequencies all showed

high correlations whereas renal autoregulation mechanisms identified in RBF and LS_{mean} did not correlate significantly in the identified operating frequencies. The percent error between the LS_{mean} and RBF estimates were determined for each frequency region over CTL and L-NAME conditions. Table 2 shows the median error with for each frequency region. Median errors between the two signals are less than 1% for the BRC, RO, and HR estimates but much higher for TGF (33%) and the MR (25%) estimates.
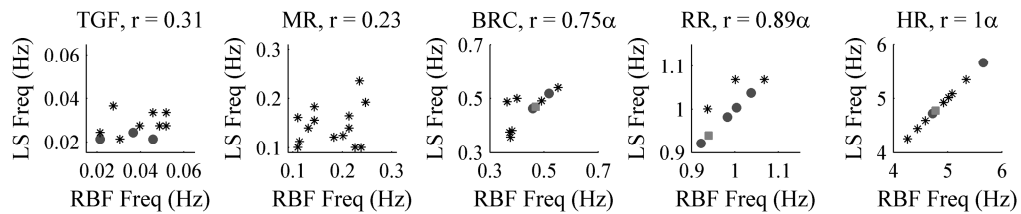
Figure 5.3 - Identified frequencies in laser speckle signals compared to renal blood flow.
Estimates of renal blood flow and laser speckle flux peak frequencies within each band during CTL and L-NAME (*n*=14 for the two conditions). Overlapping data points were grouped together for visualization purposes: stars indicate unique data points, filled circles indicate 2 estimates at that location, and squares indicate 3 estimates at that location. Correlation coefficients (r) between the renal blood flow and laser speckle flux peak frequency estimates are presented for each frequency band. High correlations are identified from the cardiac pulse (HR), respiration (RO) and baroreflex components (BRC). Frequencies identified in the MR and TGF ranges are not correlated between renal blood flow and laser speckle flux signals. α indicates significant correlation.

Median Error (*n=14*), (10th, 90th) percentiles	
TGF	33%, (0, 53)%
MR	25%, (0, 56)%
BRC	1%, (0, 26)%
RO	0%, (0, 7)%
HR	0%, (0, 0)%

Table 5.2 - Peak frequency estimation error between laser speckle flux and renal blood flow.

Using the spatially filtered and down-sampled image series, power spectra were determined at each pixel location, and peak amplitudes within the 5 frequency ranges were determined and corresponding frequencies mapped back to their pixel location. This produced frequency surface maps as in Fig. 4 where the 5 columns represent the 5 frequency regions and the 3 rows represent the infusion conditions.
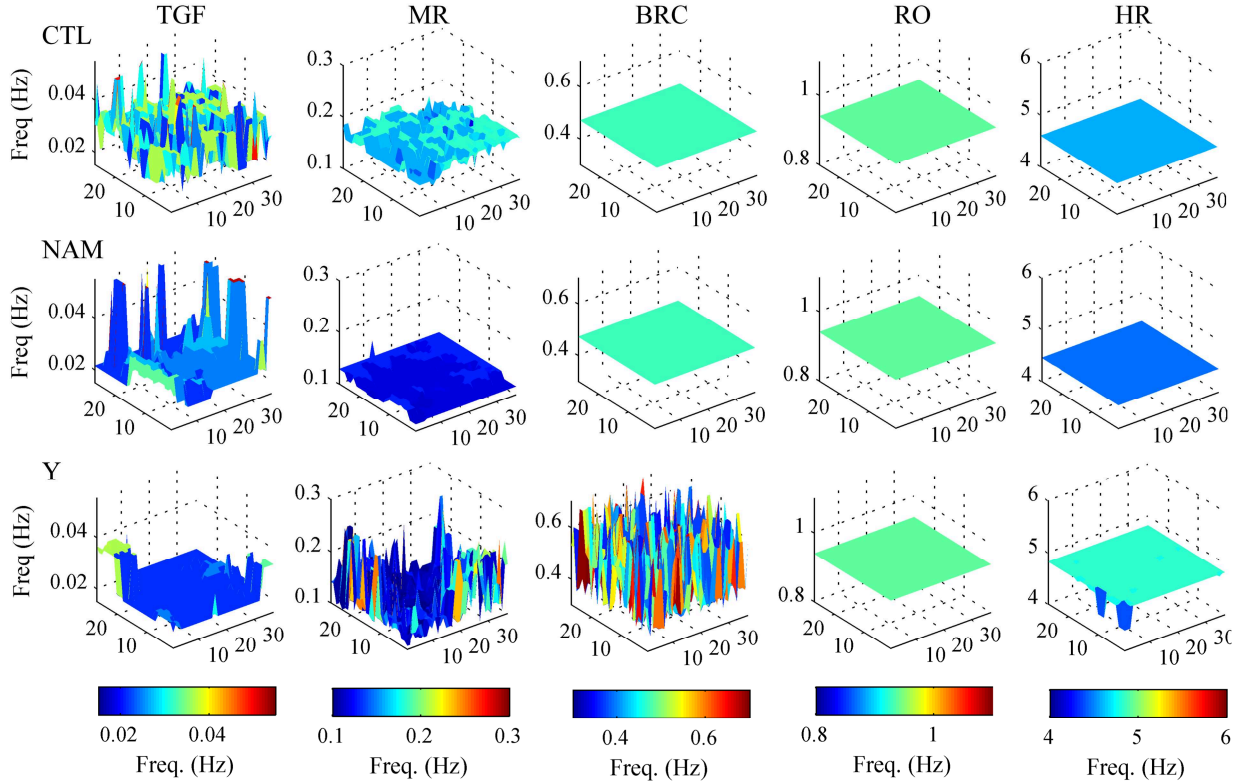
Figure 5.4 - Frequencies across the renal surface.
Surface maps of the identified frequencies for the 5 regions during CTL (top row), NAM (middle row) and Y (bottom row) for one animal. In all cases respiration (RO) and heart rate (HR) frequencies are consistent across the surface. The baroreflex component (BRC) is consistent during CTL and L-NAME, but random during Y. MR and TGF frequencies are heterogeneous relative to the three global parameters during CTL and L-NAME. The x- and y-axes specify the pixel location after down-sampling.

During all 3 conditions, RO and HR components were homogenous in their frequency distribution across the surface. The BRC frequency was constant for CTL and L-NAME. The BRC was not evident in the BP spectra in Fig. 2a during Y-27632, and therefore could not be identified in RBF or LS$_{mean}$. The MR and TGF both show heterogeneity in their frequency distribution during CTL and L-NAME. The MR frequency distribution appears random during Y-27632, as vascular smooth muscle activity is paralyzed and an MR signal can no longer be identified. During Y-27632, the TGF frequency map shows a frequency identified at 0.02 Hz, the low end of the TGF range, across much of the surface. Without vascular smooth muscle activity

to generate a TGF component, there is increased spectral power at low frequencies in a 1/f manner causing the lowest frequency within the TGF range to have the maximum amplitude.

To compare spatial heterogeneity between frequency regions, CV_{norm} was computed for each frequency surface during CTL and L-NAME conditions (Table 3). There was no significant difference in CV_{norm} between CTL and L-NAME. HR, RO and BRC CV_{norm} were all significantly lower than those of TGF and the MR, indicating a more heterogeneous distribution of frequencies for the renal autoregulation components.

		n	TGF	MR	BRC	RO	HR
CV_{norm}	CTL	7	202 ± 26	162 ± 27	108 ± 37	8 ± 8	1 ± 1
$(x10^{-3})$	L-NAME	7	224 ± 30	207 ± 19	41 ± 25 $^{\alpha,\beta}$	4 ± 4 $^{\alpha,\beta,\gamma}$	33 ± 18 $^{\alpha,\beta,\gamma}$

Table 5.3 - Normalized coefficient of variations of surface frequency distributions.
Mean ± SE, P<0.05 $^{\alpha}$ (from TGF), $^{\beta}$ (from MR), $^{\gamma}$ (from BRC) over the 2 conditions. No significant difference existed between CTL and L-NAME.

5.3.2 Functional Analysis of the Renal Autoregulation Mechanisms

Transfer function plots using either total RBF or LS_{mean} as the output during BP forcing are shown in Fig. 5. Under CTL and L-NAME conditions, both sets of transfer functions show the hallmarks of renal autoregulation with system gain < 0 dB at frequencies < 0.05 Hz and increasing gain between ~0.05 – 0.15 Hz [2, 18, 19]. The phase angle was > 0 rad between ~0.02 – 0.1 Hz and drops close to 0 rad in higher frequencies, indicating faster oscillations are not being altered by active elements within the kidney. Transfer function results are consistent with previously published reports showing impaired renal autoregulation after infusion of Y-27632 [1, 2, 20]. Table 4 contains the parameters used to quantify autoregulation for both sets of transfer functions.

80
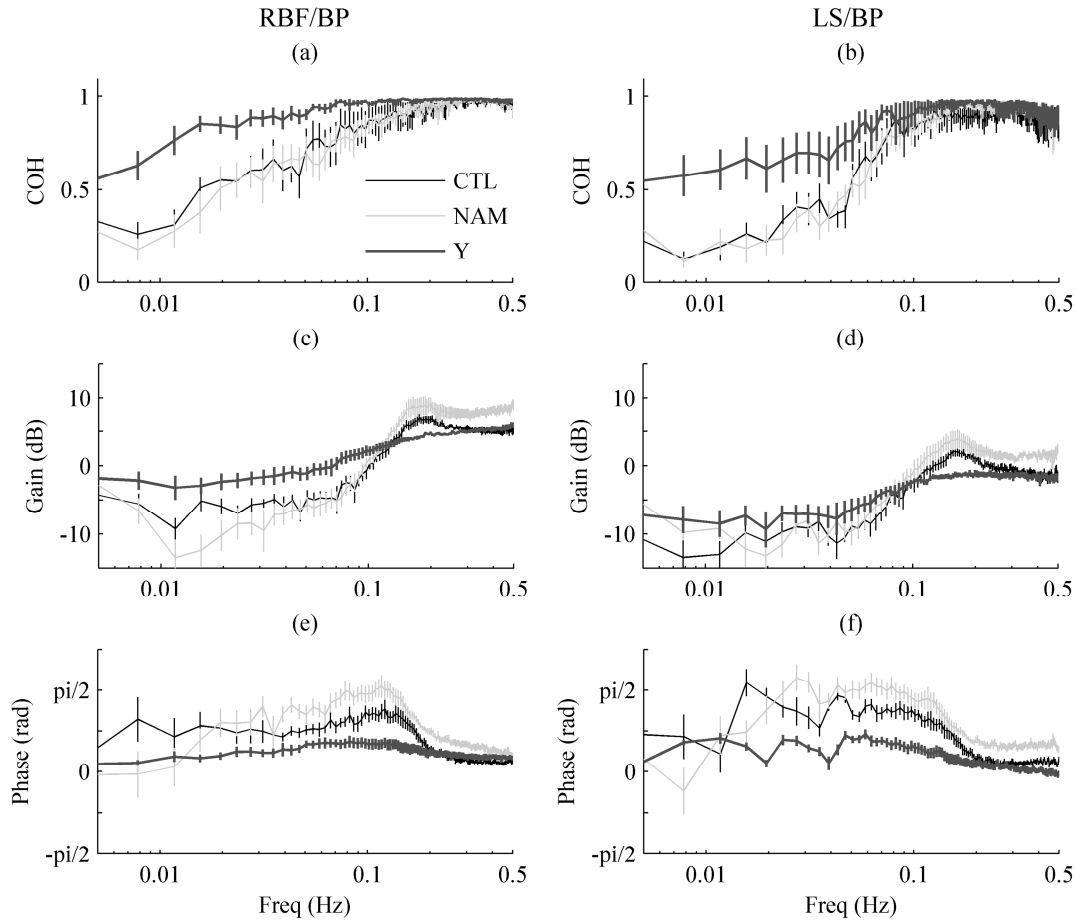
Figure 5.5 - Transfer function analysis.
Mean-squared coherence, transfer function gain and phase angle computed for blood pressure as the input signal and renal blood flow as the output signal are shown in (a), (c), and (e), respectively (control (black), L-NAME infusion (blue) and Y-27632 infusion (red), n=8 for each condition). Transfer functions were also computed using the mean laser speckle flux signal as the output in (b), (d) and (f).

	n	BP (mmHg)	COH $_{0.05 - 0.08 \text{ Hz}}$	Gain $_{0.005 - 0.02 \text{ Hz}}$ (dB)	Slope $_{0.05 - 0.15 \text{ Hz}}$ (dB/decade)	Phase $_{0.1 \text{ Hz}}$ (rad)
			Renal Blood Flow as Output Signal			
CTL	8	104 ± 3	0.78 ± 0.09	-6.6 ± 1.1	22.5 ± 3.2	1.08 ± 0.13
L-NAME	8	107 ± 3	0.72 ± 0.06	-10.2 ± 1.9	29.1 ± 4.1	1.50 ± 0.16
Y-27632	8	101 ± 6	0.95 ± 0.02 [β]	-2.5 ± 1.2 [α, β]	10.3 ± 1.6 [α, β]	0.53 ± 0.10 [α, β]
			Laser Speckle Flux as Output Signal			
CTL	8		0.71 ± 0.08	-11.4 ± 1.9	22.1 ± 3.5	1.09 ± 0.16
L-NAME	8		0.68 ± 0.06	-11.2 ± 1.3	27.8 ± 6.7	1.36 ± 0.23
Y-27632	8		0.86 ± 0.07 [β]	-8.0 ± 1.7	10.1 ± 3.2 [α, β]	0.47 ± 0.15 [α, β]

Table 5.4 - Transfer function parameters.
Mean ± SE, P<0.05 [α] (from CTL), [β] (from L-NAME).

Videos showing gain, coherence, and phase variations at each pixel over the range of frequencies from 0 – 0.5 Hz are available in *online supplementary data* for CTL, L-NAME and Y-27632 periods for one animal. The 4 parameters in Table 4 were extracted from the transfer function at each pixel, and example surface maps of the parameters under each condition are shown in Fig. 6. The values are not constant across the renal surface, suggesting heterogeneity in renal autoregulation function within the imaged area.
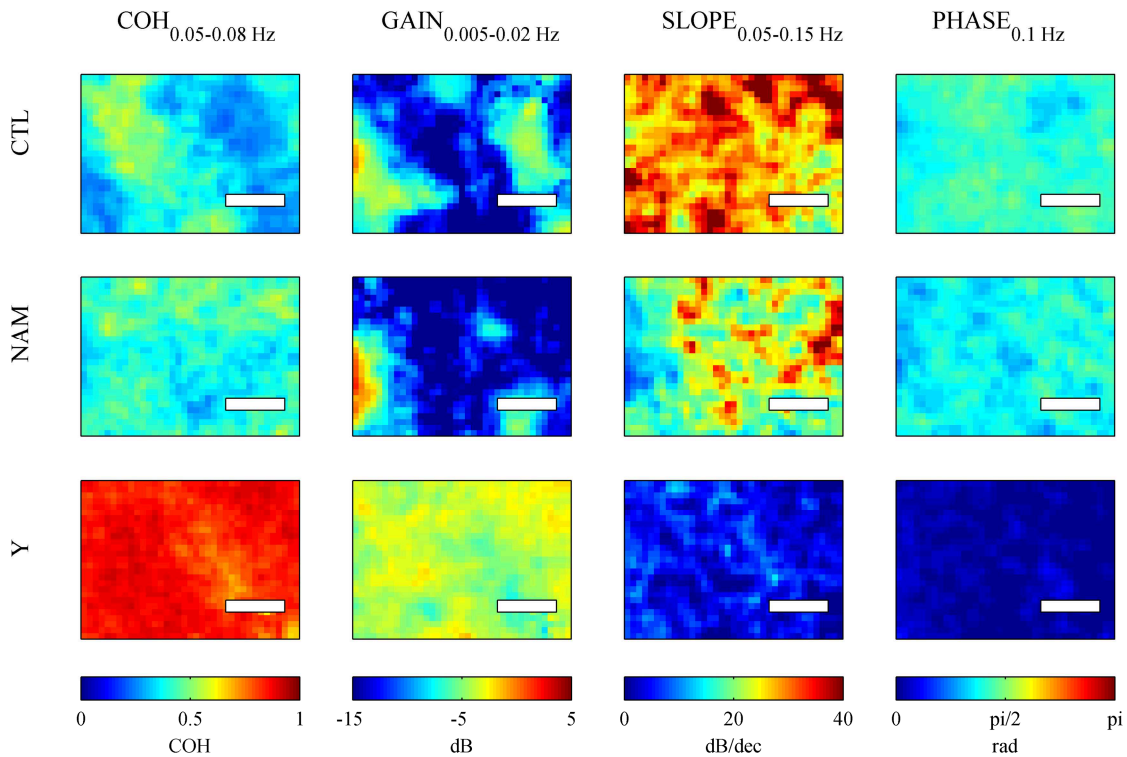
Figure 5.6 - Transfer function parameters across the renal surface.
Transfer function parameters at each pixel location during CTL (top row), NAM (middle row) and Y (bottom row) for one animal. The white rectangle is 1.28 mm long. The first column represents mean coherence from 0.05 – 0.08 Hz. Low frequency gain, gain slope reduction, and system phase at 0.1 Hz are shown in the second, third, and fourth columns, respectively.

Functional analysis was extended to monitoring system changes over time. Fig. 7 shows the results for a forcing data set where 2 additional recording periods were made during initiation of L-NAME infusion and initiation of Y-27632 infusion. The top signal traces in Fig. 7 show

LS$_{mean}$ across the 5 monitoring periods as well as the BP recording throughout the experiment.

Below the top traces are time-varying transfer function characteristics for each period.
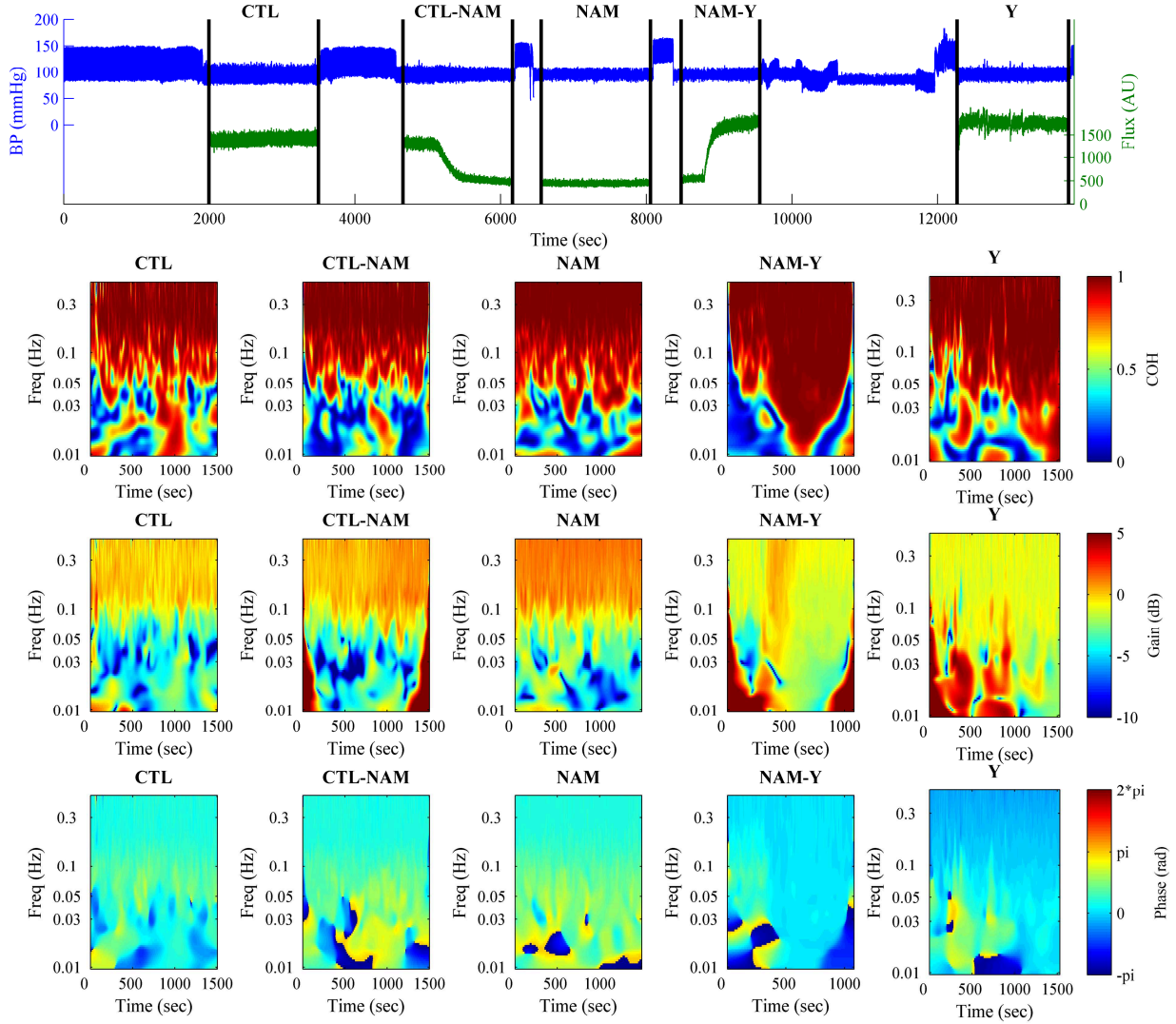
Figure 5.7 - Time-varying transfer function analysis of the mean laser speckle signal.
The top signal traces show blood pressure (blue) and flux (green) signals over time, black vertical lines indicate the start and stop monitoring times for each of the 5 sections (CTL, CTL-NAM transition period, NAM, NAM-Y transition period, and Y). Below are the time-varying coherence functions (top row), time-varying transfer function gain (middle row) and time-varying transfer function phase (bottom row) for each of the 5 periods. The gray area is the 'cone of influence' caused by edge effects in the wavelet transform.

As previously described [21], even under CTL conditions there are not consistent features as non-stationarities occur throughout the recordings. System gain in the high frequency region and phase angle in the low frequency region both moderately increase during the CTL-L-NAME

transition period and decrease along with an increase in coherence during the L-NAME-Y-27632 transition period.

The time-varying transfer functions were extended to the signals extracted from each pixel. Videos in the *online supplementary data* show changes at each pixel location in the transfer function parameters over time during CTL-L-NAME and L-NAME-Y-27632 transition periods. These demonstrate how functional renal autoregulation analysis can be extended from a single signal to both spatial and temporal dimensions and could allow identification of differences in the temporal response across a surface. Fig. 8 shows transfer function analysis from 3 time points (150 sec before, 100 sec after and 350 sec after initiation of intrarenal Y-27632 infusion) at 2 specific locations in the time-varying transfer function during the L-NAME-Y-27632 infusion period. The systems identified using the transfer functions are changing over time as Y-27632 is being infused and active vasomotion is reduced in the vasculature at both locations.
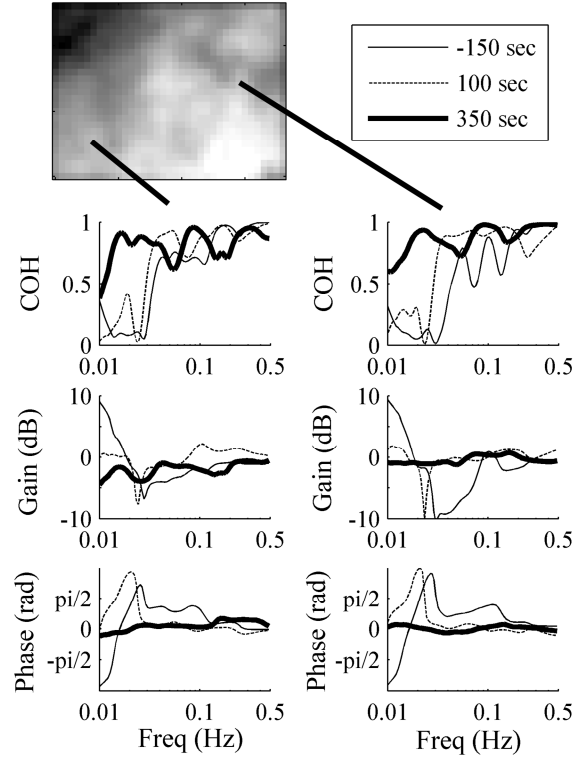
Figure 5.8 - Capturing time-varying dynamics at points across the renal surface.
Coherence, gain and phase spectra at 2 different locations during the NAM-Y transition recording at 3 time points extracted from time-varying transfer functions. The time points are 150 sec prior, 100 sec after, and 350 sec after initiation of Y infusion. At 350 sec after Y infusion has begun, coherence has increased in low frequencies, while gain and phase spectra have flattened at both locations. For any of the pairs of time points, the transfer functions from the 2 locations are similar but not identical.

5.4   Discussion

We have shown that analysis of LSPI sequences provides insight into renal perfusion dynamics across spatial and temporal dimensions. LSPI captured cardiac, respiration and baroreflex dynamics at all imaged locations, and high correlations were found between the frequencies identified in RBF and LS_{mean}. These are global parameters that are expected to occur throughout the cardiovascular system, so minimal differences between the frequency components in total RBF and extracted laser speckle signals are expected. The renal autoregulation components were identified in LSPI sequences, but their frequencies did not correlate with those in RBF measurements. RBF and LSPI are measuring perfusion from

different anatomical locations and an exact reproduction of what is found in RBF is not expected in LSPI. RBF is the average of ~30,000 nephrons [22], while LSPI, when averaged across the whole imaging window, may be looking at surface perfusion from ~100 nephrons, and when being considered on a pixel-by-pixel basis is providing information on a minimal number of local neighboring nephrons [6].

We found heterogeneity in the spatial distribution of dominant frequencies within the imaged region for renal autoregulation components but not the global parameters. CV_{norm} s of HR and RO are expected to be low, since they are global parameters that should present identically in the perfusion dynamics at all locations. Respiration was the most stable frequency across the surface as measured by CV_{norm} because animals were kept on mechanical ventilation at a fixed breathing rate. We found low variability in the baroreflex component between locations suggesting identification of a single neurogenic source with no indication of local variations. This is expected since we performed renal denervation because it has been shown that baroreflex oscillations present in renal blood flow are generated in the mesenteric circulation and baroreflex activity does not influence the renal blood flow dynamics [3, 23, 24]. In contrast to the flow oscillations generated outside the kidney, TGF and the MR are local vasomotion operations that can be heterogeneous in their frequency distribution [6]. The MR and TGF showed variability in their frequency distribution across the surface relative to the 3 other components during CTL and L-NAME, but no dominant frequency could be identified for the renal autoregulation dynamics during rho-kinase inhibition due to an inability of vessels to contract [2].

Our transfer function results agreed with previous studies looking at the impact of intrarenal L-NAME and Y-27632 infusion on renal autoregulation [2]. The shape in gain curves between RBF and LS_{mean} were similar, but gain using LS_{mean} as the input had an ~-5dB offset

from RBF. This offset is probably caused by two confounding factors. BP fluctuations may already be somewhat damped when they reach the arteriolar level [25], resulting in an overestimate of the BP fluctuations compared to the local flow generating the laser speckle signal. Additionally, as with laser Doppler flowmetry, laser speckle imaging results in a non-zero flux signal under no flow conditions [12, 26]. Because of this offset in flux, we underestimate the fluctuations in LS_{mean} resulting in a reduced gain at all frequencies. This offset is purely technical and does not affect the shape of the gain curves, phase angles, or coherence. Phase angles were also similar between RBF and LS_{mean} signals telling us that the systems respond to the changes induced by L-NAME and Y-27632 infusion similarly, although the phase angle and coherence both decrease as the frequency approaches 0.5 Hz. This may be a result of imperfect timing between the laser speckle and BP recordings that were not synchronized through the instrumentation. This becomes evident at high frequencies where a partial-second difference can have a significant impact on the phase angle between BP and laser speckle measurements. While total RBF based transfer functions describe how renal autoregulation is operating at the whole system level, the local LSPI data tell us how a subpopulation of superficial nephrons inside of the kidney is responding.

To quantify parameters we used time-invariant frequency and transfer function analysis, but it has been shown that renal autoregulation dynamics are time-varying [21, 27, 28]. By applying time-varying transfer functions we can begin to study the response of these system properties over time, and from our videos in the online supplementary data we can visualize temporal as well as spatial changes. Fig. 8 highlights how we are able to monitor changes in the transfer functions at all locations as Y-27632 impacts the system and we see the results of increased coherence and a flattened gain and phase spectra. This analysis could be used to

87

understand how regions of nephrons in the renal cortex operate together, or independently, and what interventions might change these interactions.

5.4.1 Laser Speckle Imaging Advantages and Limitations

Laser Doppler flowmetry has previously been shown to be a successful method for analyzing renal autoregulation signals from a point on the renal surface containing information provided from 10's to 100's of nephrons [5, 22, 29]. The advantage LSPI provides is that we are able to monitor perfusion at all locations across a surface simultaneously which enables us to study the dynamics at all points [6]. With a sampling rate of 25 Hz, the moorFLPI is capable of identifying frequencies up to the cardiovascular dynamics. Using an increased magnification moorFLPI system, we were able to have an imaging window of ~5x7 mm in size, allowing an extension of previous studies analyzing temporal signals in renal autoregulation that were limited to 2 or 3 simultaneous single nephron measurements [4, 8, 30].

Studies have shown the importance of the number of pixels in computing accurate laser speckle statistics to obtain perfusion values [14, 31]. The moorFLPI provides two options to compute perfusion values: temporally at each pixel over 25 frames (perfusion sequences sampled at 1 Hz) or spatially at each frame over a 5x5 region of neighboring pixels (perfusion sequences sampled at 25 Hz). In either mode, the number of pixels used for computation is fixed at 25. We used the spatial computation method to sample at a rate sufficient to capture the cardiac dynamics and avoid aliasing of cardiac and respiration components when analyzing renal autoregulation mechanisms. Single pixel flux measurements of renal perfusion from the moorFLPI have low signal to noise ratios, and we therefore average flux values between neighboring pixels to receive adequate signals. This reduces our effective spatial resolution by the number of pixels averaged. To account for blurring introduced by the spatial filter we down-

sample each frame by a factor of 4, increasing the physical width captured with each pixel from ~40 μm/pixel to ~160 μm/pixel. We are not able to identify specific nephrons using this method but rather have cortical perfusion signals from locations across the renal surface.

A drawback to LSPI is that the depth of the tissue where blood flow is providing information is not precisely known [32, 33]. LSPI has an advantage over laser Doppler in that the depth of imaging will be shallower even though LSPI generally uses a more powerful laser because it uses a diverging laser source that spreads the power across the surface [33] while laser Doppler focuses the laser at a single location [22, 29]. Depending on the specific instrument and area being imaged, the penetration depth for laser Doppler flowmetry may be at least 3x greater than LSPI [33]. In the highly vascularized renal cortex our predominant signal should be from scatterers (red blood cells) in the most superficial layers of the cortex (~100 μm deep) [12], which is ideal to examine blood flow in only the most superficial nephrons [34, 35]. LSPI appears well suited for studying spatial and temporal variations in flow.

5.4.2   Perspectives and Significance

By performing functional analysis at points across the spatial imaged region we are able to compare how renal autoregulation is functioning at multiple points in the superficial layer of the renal cortex which has not been possible using traditional single point measurements. Holstein-Rathlou *et al.* showed how this type of information can be used to understand the interactions between spatial locations [6]. By using transfer function analysis across the renal surface, we have shown how this technology could be used to identify regions in the renal cortex that lack effective autoregulation. By visualizing the slope of gain reduction at all locations, we can see the systemic changes across the surface when the vasculature is unable to respond to BP fluctuations. By combining spatial perfusion imaging with time-varying analysis, we are able to

determine which regions have properly functioning autoregulation and track the system properties over time. This technique could be used to study the temporal response of the system under various conditions, or potentially to identify regions of nephrons that may have failing autoregulation over time. This type of analysis could be extended to other vascular beds to study vasomotion at many points within a region of interest.

5.5   Appendix: Coefficient of Variation for a Uniform Distribution

The theoretical mean and standard deviation of a continuous uniform distribution over a band [f_1, f_2] are defined as $\mu_{uniform}$ and $\sigma_{uniform}$ in Eqs. A.1 and A.2, respectively.

$$\mu_{uniform} = \frac{(f_1 + f_2)}{2} \tag{A.1}$$

$$\sigma_{uniform} = \sqrt{\frac{(f_2 - f_1)^2}{12}} \tag{A.2}$$

The dimensionless coefficient of variation (*CV*) of a probability distribution is defined as the standard deviation over the mean, A.3.

$$CV = \frac{\sigma}{\mu} \tag{A.3}$$

Substituting the theoretical mean and standard deviation of a uniform distribution into A.3 produces the theoretical coefficient of variation of a uniform distribution, A.4.

$$CV_{uniform} = \frac{(f_2 - f_1)}{\sqrt{3}(f_2 + f_1)} \tag{A.4}$$

5.6   Acknowledgements

from the American Heart Association. B. Braam is a Heart and Stroke Foundation of Canada New Investigator.

5.7   References

[1]   Cupples, W.A. and B. Braam. Assessment of renal autoregulation. *American Journal of Physiology. Renal Physiology.* 292:F1105-F23, 2007.

[2]   Shi, Y., X. Wang, K.H. Chon and W.A. Cupples. Tubuloglomerular feedback-dependent modulation of renal myogenic autoregulation by nitric oxide. *American Journal of Physiology. Regulatory, Integrative and Comparative Physiology.* 290:R982-R91, 2006.

[3]   Abu-Amarah, I., D.O. Ajikobi, H. Bachelard, W.A. Cupples and F.C. Salevsky. Responses of mesenteric and renal blood flow dynamics to acute denervation in anesthetized rats. *American Journal of Physiology. Regulatory, Integrative and Comparative Physiology.* 275:R1543-R52, 1998.

[4]   Holstein-Rathlou, N.H. Synchronization of proximal intratubular pressure oscillations: evidence for interaction between nephrons. *Pflügers Archiv European Journal of Physiology.* 408:438-43, 1987.

[5]   Smedley, G., K.P. Yip, A. Wagner, S. Dubovitsky and D.J. Marsh. A laser Doppler instrument for in vivo measurements of blood flow in single renal arterioles. *Biomedical Engineering, IEEE Transactions on.* 40:290-97, 1993.

[6]   Holstein-Rathlou, N.-H., O.V. Sosnovtseva, A.N. Pavlov, W.A. Cupples, C.M. Sorensen and D.J. Marsh. Nephron blood flow dynamics measured by laser speckle contrast imaging. *American Journal of Physiology. Renal Physiology.* 300:F319-F29, 2011.

[7]   Marsh, D.J., A.S. Wexler, A. Brazhe, D.E. Postnov, O.V. Sosnovtseva and N.-H. Holstein-Rathlou. Multinephron dynamics on the renal vascular network. *American Journal of Physiology. Renal Physiology.* 2012.

[8]   Yip, K.P., N.H. Holstein-Rathlou and D.J. Marsh. Dynamics of TGF-initiated nephron-nephron interactions in normotensive rats and SHR. *American Journal of Physiology. Renal Physiology.* 262:F980-F88, 1992.

[9]   Bricq, S., G. Mahé, D. Rousseau, A. Humeau-Heurtier, F. Chapeau-Blondeau, J. Rojas Varela and P. Abraham. Assessing spatial resolution versus sensitivity from laser speckle contrast imaging: application to frequency analysis. *Medical and Biological Engineering and Computing.* 50:1017-23, 2012.

[10]   Humeau-Heurtier, A., P. Abraham, S. Durand, G. Leftheriotis, D. Henrion and G. Mahé. Clinical use of laser speckle techniques: beyond the sole mapping. *Medical and Biological Engineering and Computing.* 50:1001-02, 2012.

[11]   Dunn, A.K., H. Bolay, M.A. Moskowitz and D.A. Boas. Dynamic imaging of cerebral blood flow using laser speckle. *Journal of Cerebral Blood Flow and Metababolism.* 21:195-201, 2001.

[12]   Bezemer, R., M. Legrand, E. Klijn, M. Heger, I.C. Post, T.M. van Gulik, D. Payen and C. Ince. Real-time assessment of renal cortical microvascular perfusion heterogeneities using near-infrared laser speckle imaging. *Optics Express.* 18:15054-61, 2010.

[13]   Humeau-Heurtier, A., G. Mahe, S. Durand and P. Abraham, Multiscale entropy study of medical laser speckle contrast images. *Biomedical Engineering, IEEE Transactions on.* 60(3):872-9, 2013.

[14]   Humeau-Heurtier, A., G. Mahe, S. Durand, D. Henrion and P. Abraham. Laser speckle contrast imaging: Multifractal analysis of data recorded in healthy subjects. *Medical Physics.* 39:5849-56, 2012.

[15] Uehata, M., T. Ishizaki, H. Satoh, T. Ono, T. Kawahara, T. Morishita, H. Tamakawa, K. Yamagami, J. Inui, M. Maekawa and S. Narumiya. Calcium sensitization of smooth muscle mediated by a Rho-associated protein kinase in hypertension. *Nature*. 389:990-94, 1997.

[16] Torrence, C. and P.J. Webster. Interdecadal changes in the ENSO-Monsoon system. *Journal of Climate*. 12:2679-90, 1999.

[17] Whitcher, B., P.F. Craigmile and P. Brown. Time-varying spectral analysis in neurophysiological time series using Hilbert wavelet pairs. *Signal Processing*. 85:2065-81, 2005.

[18] Wang, X. and W.A. Cupples. Interaction between nitric oxide and renal myogenic autoregulation in normotensive and hypertensive rats. *Canadian Journal of Physiology and Pharmacology*. 79:238-45, 2001.

[19] Wang, X., F.C. Salevsky and W.A. Cupples. Nitric oxide, atrial natriuretic factor, and dynamic renal autoregulation. *Canadian Journal of Physiology and Pharmacology*. 77:777-86, 1999.

[20] Cupples, W.A. and R.D. Loutzenhiser. Dynamic autoregulation in the in vitro perfused hydronephrotic rat kidney. *American Journal of Physiology. Renal Physiology*. 275:F126-F30, 1998.

[21] Chon, K.H., Y. Zhong, L.C. Moore, N.H. Holstein-Rathlou and W.A. Cupples. Analysis of nonstationarity in renal autoregulation mechanisms using time-varying transfer and coherence functions. *American Journal of Physiology. Regulatory, Integrative and Comparative Physiology*. 295:R821-R28, 2008.

[22] Wang, H., K. Siu, K. Ju, L.C. Moore and K.H. Chon. Identification of transient renal autoregulatory mechanisms using time-frequency spectral techniques. *Biomedical Engineering, IEEE Transactions on*. 52:1033-39, 2005.

[23] Malpas, S.C., R.G. Evans, G.A. Head and E.V. Lukoshkova. Contribution of renal nerves to renal blood flow variability during hemorrhage. *American Journal of Physiology. Regulatory, Integrative and Comparative Physiology*. 274:R1283-R94, 1998.

[24] Just, A., U. Wittmann, H. Ehmke and H.R. Kirchheim. Autoregulation of renal blood flow in the conscious dog and the contribution of the tubuloglomerular feedback. *The Journal of Physiology*. 506:275-90, 2004.

[25] Heyeraas, K.J. and K. Aukland. Interlobular arterial resistance: influence of renal arterial pressure and angiotensin II. *Kidney International*. 31:1231-39, 1987.

[26] Nilsson, G.E., T. Tenland and P.A. Oberg. Evaluation of a laser Doppler flowmeter for measurement of tissue blood flow. *Biomedical Engineering, IEEE Transactions on*. 597-604, 1980.

[27] Cupples, W.A., P. Novak, V. Novak and F.C. Salevsky. Spontaneous blood pressure fluctuations and renal blood flow dynamics. *American Journal of Physiology. Renal Physiology*. 270:F82-F89, 1996.

[28] Scully, C.G., K.L. Siu, W.A. Cupples, B. Braam and K.H. Chon. Time–frequency approaches for the detection of interactions and temporal properties in renal autoregulation. *Annals of Biomedical Engineering*. 41:172-84, 2013.

[29] Yip, K.P., N.H. Holstein-Rathlou and D.J. Marsh. Mechanisms of temporal variation in single-nephron blood flow in rats. *American Journal of Physiology. Renal Physiology*. 264:F427-F34, 1993.

[30] Chen, Y.M., K.P. Yip, D.J. Marsh and N.H. Holstein-Rathlou. Magnitude of TGF-initiated nephron-nephron interactions is increased in SHR. *American Journal of Physiology. Renal Physiology*. 269:F198-F204, 1995.

[31] Skipetrov, S.E., J. Peuser, R. Cerbino, P. Zakharov, B. Weber and F. Scheffold. Noise in laser speckle correlation and imaging techniques. *Optics Express*. 18:14519-34, 2010.

[32] Boas, D.A. and A.K. Dunn. Laser speckle contrast imaging in biomedical optics. *Journal of Biomedical Optics.* 15:011109-12, 2010.

[33]   O'Doherty, J., P. McNamara, N.T. Clancy, J.G. Enfield and M.J. Leahy. Comparison of instruments for investigation of microcirculatory blood flow and red blood cell concentration. *Journal of Biomedical Optics*. 14:034025-13, 2009.

[34]   Beeuwkes, R. Efferent vascular patterns and early vascular-tubular relations in the dog kidney. *American Journal of Physiology*. 221:1361-74, 1971.

[35]   Beeuwkes, R. and J. Bonventre. Tubular organization and vascular-tubular relations in the dog kidney. *American Journal of Physiology*. 229:695-713, 1975.

Chapter 6: Segmentation of Renal Surface Perfusion Signals into Clusters with Phase Synchronized Renal Autoregulation Dynamics

6.1   Introduction

Renal blood flow is regulated by at least 2 feedback systems that operate within a nephron, the functional unit of the kidney, and its arterioles to protect the glomerular capillaries and maintain glomerular filtration rate during blood pressure fluctuations by constricting and dilating the afferent arteriole in a process known as renal autoregulation. The 2 feedback mechanisms, the myogenic response (MR) and tubuloglomerular feedback (TGF), generate self-sustained oscillations in normotensive rats within ranges of [0.1 – 0.3 Hz] and [0.02 – 0.05 Hz], respectively [1]. A human kidney contains ~1,000,000 nephrons (~30,000 in a rat). Although each nephron can be thought of as an independent unit, they are connected by a vascular tree stemming from the renal artery which branches into increasingly smaller vascular segments till reaching the afferent arteriole preceding each nephron [2]. Synchronization in the dynamics has previously been reported between neighboring nephrons in tubule pressure signals [3, 4] and renal perfusion signals obtained by laser speckle perfusion imaging (LSPI) [5]. The vascular tree that connects nephrons provides a cable for the transfer of information [6], and modeling studies have shown that vascular conduction can synchronize dynamics between nephrons [7, 8]. Such synchronization may contribute to renal autoregulation by the development of vascular resistance and spatial and temporal smoothing of blood flow [9].

Evidence examining synchronization on a wide scale requires imaging approaches to monitor flow with sufficient spatial and temporal resolution. LSPI provides information about temporal perfusion changes in the superficial vasculature across an imaged region [10]. We

investigated LSPI for measuring renal perfusion across the cortex and found time-series could be extracted that contain the relevant autoregulation dynamics [11]. The operating frequencies of the MR and TGF can be tracked at each location as they vary over time. Correlations in the time-varying dynamics between any 2 locations can then be analyzed to detect synchronization in the form of phase coupling. When 2 oscillators have constant phase relationships over a period of time it may be that a physical coupling maintains that relationship, while 2 independent oscillators would be expected to have phase relationships vary over time [12].

Phase coherence (PC), defined as the exponential difference between the instantaneous phases of two signals, is a robust measure for quantifying phase relationships over time between a pair of oscillators [13]. PC is bound by 0 (no coupling) and 1 (complete coupling), but what constitutes significant phase coupling between these extremes can be open ended. Surrogate data that maintains the characteristics of the signal but destroys the phase relationship with another signal can provide a threshold for each pair of signals [12]. With PC values between all pairs of pixels, clustering analysis can then be applied to identify phase-coupled regions [14].

We present a method for segmenting laser speckle image sequences of the renal cortex into regions with phase-coupled dynamics. Our two-step procedure first uses phase coherence with a significance test to identify pairs of pixels with significant phase coupling, and these estimates are then clustered to identify phase-coupled regions. The method is illustrated with LSPI of the renal cortex of an anaesthetized rat. The paper is organized as follows: II – experimental data acquisition is described and data presented to set the problem, III – estimation of phase coherence and the significance level are described and applied to renal perfusion data, IV – three different clustering approaches are presented, compared and applied, V –

segmentation results for the renal surface of 6 animals are presented, VI – benefits and limitations of the approach are discussed.

6.2   Experimental Methods

Experiments were performed in accordance with the guidelines of the Canadian Council on Animal Care and approved by the Animal Care Committee of Simon Fraser University. A single, male, Long-Evans rat (Harlan, Livermore, CA, USA) was given buprenorphine (0.02 mg/kg i.p.) 20 min. prior to being placed under anaesthesia with 4% isoflurane in inspired gas, then reduced to 2%. The animal was placed on a heated table (35°C), and the trachea cannulated for ventilation by a small animal respirator (TOPO, Kent Scientific, Torrington, CT, USA). The left kidney was exposed, freed from surrounding fat, and secured in a kidney cup anchored to the table. Grease was placed in the cup around the kidney to minimize motion. An additional set of experiments were performed with Long-Evans rats (N=6) after bolus infusion of the nitric-oxide synthase inhibitor N^{ω}-nitro-l-arginine methyl ester (L-NAME) (Sigma-Aldrich, Oakville, ON, Canada) at 10 mg/kg$_{BODY\text{-}WEIGHT}$.

LSPI was performed 1 hr after kidney preparation using the moorFLPI laser speckle contrast imager (Moor Instruments, Axminster, UK). The moorFLPI illuminates the target surface with a 785 nm laser providing flow information for the most superficial nephrons in the renal cortex ~100 – 500 μm deep [15]. The resulting speckle pattern is captured with a CCD camera at a frame rate of 25 Hz. Flow changes in the tissue alter the speckle pattern such that higher flow blurs the pattern reducing the contrast and lower flow increases the contrast [16]. Contrast statistics of the pattern were computed over a spatial set of pixels resulting in a relative perfusion index mapped across the surface at 113 x 152 pixels and 25 Hz [5]. The lens was positioned ~20 cm away from the kidney resulting in an imaging window of ~5 x 7 mm. An ~4

mm hair was placed on the renal surface to determine the pixel length, and the renal surface was monitored for ~300 sec for each animal.

After acquisition, flux image series were loaded into Matlab r2011b (The Mathworks, Natick, MA) for processing. A Gaussian spatial filter (width of 8 pixels corresponding to -10 dB cutoff) was applied to each frame to increase the signal-noise ratio of the time-series at each pixel [17], and the filtered images were spatially downsampled by a factor of four to reduce redundant information at adjacent pixels caused by the spatial filter. Time-series extracted from each pixel were low-pass filtered (0.5 Hz cutoff frequency) and downsampled to 1 Hz because the pertinent autoregulation frequencies are in the 0.01 – 0.3 Hz frequency range [1].

Fig. 1a shows the time-averaged flux at each downsampled pixel for the single animal without L-NAME bolus infusion, and Fig. 1b shows the flux spectra from the four white star locations in Fig. 1a. Locations were selected to demonstrate the approach with 2 locations each sharing the same frequency. Frequencies between 0.1 and 0.2 Hz in Fig. 1b can be identified as the MR signature. Two signals have a dominant frequency around 0.13 Hz and the other two signals have a dominant frequency >0.15 Hz. It might be expected that signals sharing the same frequency are coupled, but this alone does not guarantee coupling since renal autoregulation dynamics are highly time-varying and instantaneous phase changes may be uncorrelated between the two signals [18, 19]. For this reason we test for phase coupling by evaluating the temporal variations in the phase difference between the two signals using PC and a significance test.
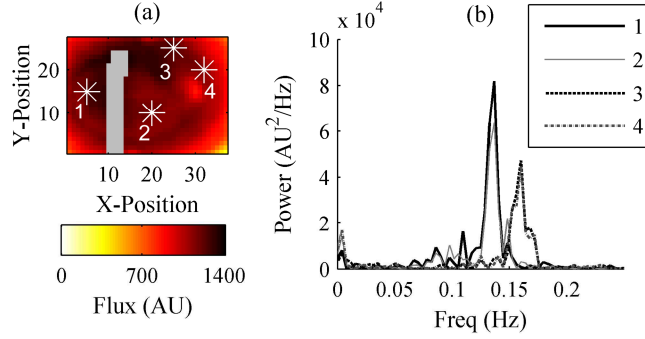
Figure 6.1 - Example laser speckle perfusion imaging data.
(a) Time-averaged laser speckle perfusion image of the renal cortex. The gray bar represents the 4mm hair placed across the renal cortex. (b) Frequency spectra of the extracted time-series from the 4 locations denoted by a star in (a).

6.3   Detecting Phase Coherence

6.3.1   Estimation of Phase Coherence

Our method uses the time-series extracted from each pixel within the LSPI videos and analyzes the changes in the temporal relationships in renal autoregulation dynamics between pixels. The first step is to estimate PC for the MR or TGF dynamic between every pixel pair. To the extent that perfusion dynamics from two locations are coupled, the phase difference between the two should remain constant over time. A significance threshold derived from surrogate data is then used to determine if the observed PC is statistically different from the PC values of two signals with similar time-varying dynamics but with phase relationships destroyed.

To determine PC between two signals the instantaneous phases for each are first estimated. Each signal is band-pass filtered for either the MR or TGF range using a forwards-backwards Butterworth filter to preserve phase relationships in the signals. For the MR frequency range, a 16th order filter with low- and high-cutoff frequencies of 0.09 and 0.32 Hz, respectively, is used to isolate the dynamic. After band-pass filtering, the Hilbert transform is applied to find the analytic signal and subsequently determine the instantaneous frequency at all

time points, *f(t)*. Ideally the instantaneous frequency will remain between the cutoff frequencies of the band-pass filters, but when noise is present in the data phase slips can occur that cause the frequency to jump outside of the range of the band-pass filter. Locations where the instantaneous frequency has extended beyond the band-pass filter cutoff frequencies are identified and linearly interpolated to ensure that all instantaneous frequencies are within the pass-band of the filters [12]. The instantaneous phase, *φ(t)*, is the integral of the instantaneous frequency and wrapped between -π and π. PC is then computed between two signals, *m* and *j*, as the mean over *N* data points of their exponential difference in phase, (1) [13].

$$PC_{mj} = \left| \frac{1}{N} \sum_{l=1}^{n} e^{i\left(\varphi_{jl} - \varphi_{ml}\right)} \right|$$

(1)

The PC statistic gives a value between 0 and 1, where 0 represents no phase-locking between two signals and 1 represents complete phase-locking as would be expected from computing PC between a signal and itself, in the case *m = j*. To determine the significance of values between the extremes, we apply a surrogate data-derived threshold to test the null hypothesis that the instantaneous phase relationships between the signals are independent in time [12]. The instantaneous frequency of one of the two signals is circularly shifted a random distance in time (*n*) to destroy phase relationships between the two signals as

$$f_{surr}(t) = \begin{cases} f(t-n) & n+1 \le t \le N \\ f(N-n+t) & 1 \le t \le n \end{cases}$$

(2)

f_{surr}(t) is used to estimate the surrogate instantaneous phases, *φ_{surr}(t)*. This procedure removes phase relationships between the two signals but maintains the signal dynamics [20]. PC is then estimated between *φ_{surr}(t)* and *φ(t)* from the signal the surrogate procedure is not performed on. Fifty surrogate PC estimates are made, and the significance threshold is set as the mean plus 2 standard deviations of the surrogate PC estimates. Two signals are declared as having significant

PC if greater than the threshold. This approach for estimating PC and determining the significance of the estimate is repeated for all pairs of signals extracted from the image sequences.

6.3.2 Application to Renal Autoregulation Data

Table 1 reports PC and significance threshold estimates between the pairs of signals identified in Fig. 1 for the animal under control conditions. Between signals 1&2 a PC greater than the threshold exists indicating that these two signals are phase coupled. The same is true for signals 3&4. All other pairs have PC less than the threshold indicating those pairs are not phase coupled.

Signal		Phase	Significance
m	j	Coherence	Threshold
1	2	0.81*	0.27
1	3	0.10	0.28
1	4	0.05	0.32
2	3	0.10	0.30
2	4	0.07	0.36
3	4	0.86*	0.33

Table 6.1 - Phase coherence and significance thresholds.
*Indicates significant phase coupling, the estimated phase coherence between signals m and j is greater than the significance threshold generated from 50 pairs of surrogate data.

PC and significance level estimates are determined between the time-series from all pixel pairs and maps of PC between each pixel and all others are generated. Figs. 2a-d show PC maps for the 4 example locations. In each frame of Fig. 2, PC between the time-series from every pixel and the pixel identified with the white star is displayed. Combinations of pixels that do not have significant PC are set as white.
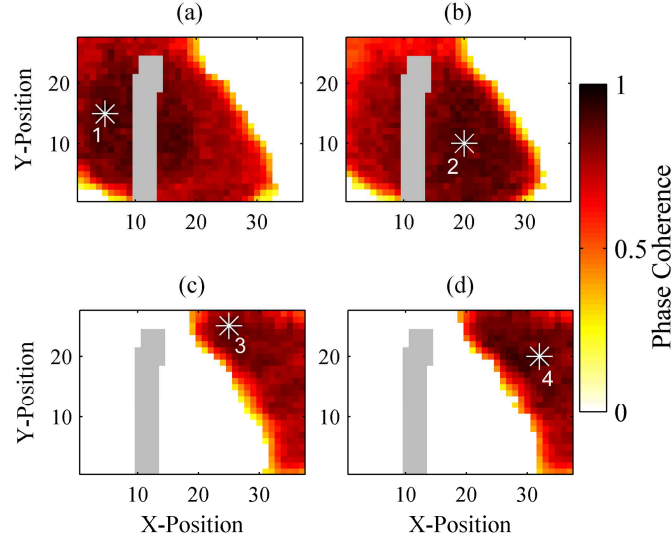
Figure 6.2 - Phase coherence across the renal surface.
(a) Represents phase coherence between signal 1, marked by the white star, and all other pixels. The gray bar represents the wire placed on the surface, and white space indicates non-significant phase coherence as determined by the surrogate significance threshold. (b-d) contain phase coherence estimates relative to the pixel marked by the white star in each frame. The stars and numbers correspond with the locations in Fig. 1.

Fig. 2a shows that signal 1 has significant PC with all other pixels within the large colored region. From Fig. 2b, we see that signal 2 is also phase coupled with the same pixels as signal 1 and this large colored area corresponds to a phase coupled cluster. In Figs. 2c&d, we see that signals 3&4 are phase coupled together within a second cluster. Visualizing these surface maps is useful to gain an understanding of the PC distribution across the surface, and clustering analysis can be applied to find groups of phase-coupled pixels [21].

6.3.3   Impact of Signal Characteristics

Meaningful estimates of PC and the significance level depend on appropriate signal length and strength of the dynamic relative to background noise, and therefore what is meaningful can vary based on the signal characteristics. To demonstrate the influence of these characteristics, we selected 100 pairs of signals within the large coupled region in Fig. 2a&b, and another 100 pairs where one of the signals belongs to the coupled region in Fig. 2a&b and the

other belongs to the region in Fig. 2c&d. The signals were selected from locations evenly dispersed across each region. This provided pairs of phase coupled and non-coupled signals.

PC and significance levels were determined between each pair for data lengths increasing from the first 50 sec of the signals up until the full data length (340 sec). Mean and 95% confidence intervals over the pairs of coupled and non-coupled signals were determined for the PC and significance levels, Fig. 3a.
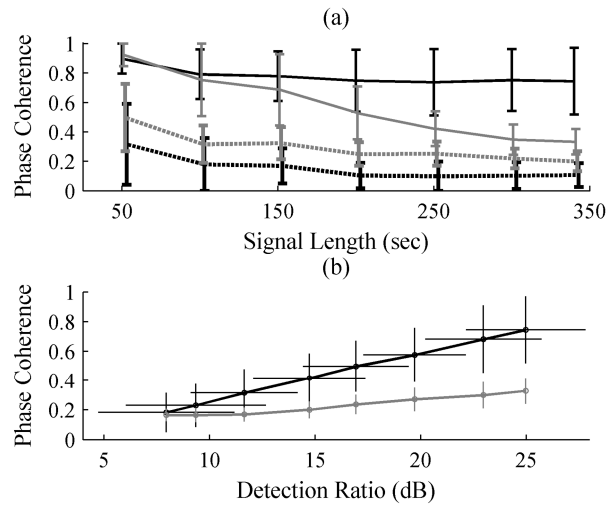
Figure 6.3 - Phase coherence as a function of signal characteristics.
Fig. 3. (a) Impact of data length on phase coherence and significant thresholds. Solid lines are mean and 95% confidence intervals for 100 pairs of signals belonging to the same coupled region. Dashed lines are the same for 100 pairs of signals belonging to different regions (non-phase coupled signals). Black lines represent the phase coherence and gray lines significance levels. (b) Impact of white noise on phase coherence. Solid black line is phase coherence computed between pairs of pixels expected to belong to same cluster for varying levels of noise added with the 95% confidence intervals on phase coherence (vertical error bars) and detection ratio (horizontal error bars). The gray line represents the significance thresholds with 95% confidence levels over the 100 pairs.

PC and significance levels are increased at short data lengths, and there is decreased separation between the true PC and surrogate-derived significance levels as the data length is decreased. As the data length increases to >250 sec there is clear identification of the phase coupled pairs. For uncoupled pairs, dashed lines in Fig. 3a, the separation between significance levels and PC is relatively constant at data lengths greater than 150 sec.

The peak power of the MR dynamic relative to background noise was computed using the detection ratio, (3). In (3), P_{sig} is the peak power of the dynamic within the MR frequency range, 0.1 – 0.3 Hz, from the power spectrum. P_{noise} is power of the noise region, 0.3 – 0.5 Hz.

$$DR = 10\log_{10}\left(\frac{P_{sig} - \overline{P}_{noise}}{STD(P_{noise)}}\right) \tag{3}$$

White noise was added in increasing amplitudes [0, 0.5, 1, 1.5, 2, 3, 4, 5] to the signals after normalization by the signal variance. PC and significance levels were estimated at each noise level as was the detection ratio for each signal plus noise combination. The detection ratio was averaged between the two signals in each pair. Mean and 95% confidence intervals are shown in Fig. 3b of PC and significance levels as functions of the detection ratio for increasing noise levels for the phase coupled pairs. Horizontal error bars represent 95% confidence intervals of the detection ratio for the 100 signal pairs. With no noise added, the MR dynamic has a detection ratio of ~25 dB between all pairs of signals. As the detection ratio decreases due to added noise, PC and significance levels decrease. At detection ratios <10 dB there is poor separation between PC and significance levels, and accurate estimates of significant PC cannot be made. Results are not shown for the uncoupled signal pairs as PC and significance levels had insignificant changes for increasing levels of added noise. As the signal characteristics change from data length and noise PC values vary. Using the surrogate data allows us to adapt the significance threshold to the changing signal characteristics.

6.4   Identification of Synchronized Clusters

Allefeld *et al.* proposed a method for identifying clusters from a group of oscillators with bivariate synchronization indices by finding the dominant eigenvectors of a synchronization matrix [14]. Allefeld and Bialonski proposed an alternative method based on spectral clustering

concepts that improved on some of the limitations of the former approach including the influence of PC present between locations that are not clustered, intercluster PC [21]. We compare these two methods and a non-negative matrix factorization approach using a fixed cluster model representative of data expected from LSPI of the renal cortex. All three clustering approaches use PC and significance levels between pixels without spatial information.

The three methods are briefly described below with references for further descriptions of each. In all approaches, the first step is to transform the PC maps for every pixel location, as in Fig. 2, into a single synchronization matrix. The synchronization matrix, R, contains the bivariate synchronization indices, PC, between all pairs of pixels. R_{mj} is the PC between pixel m and j. If pixels m and j did not have significant PC determined by the threshold R_{mj} was set to 0.

6.4.1 Clustering Approaches

6.4.1.A Eigendecomposition

From the synchronization matrix, R, we use the clustering algorithm described by Allefeld *et al.* to find the cluster that pixel j belongs to corresponding to the maximum participation index, *PI* [14]. The normalized eigenvectors, v, and eigenvalues, λ, of R determine the participation index, PI_{jk} for pixel j and eigenvector k, (4).

$$PI_{jk} = \lambda_k v_{jk}^2 \tag{4}$$

PI_{jk} describes the engagement of pixel j in the component corresponding to cluster k. Each pixel is set to belong to the cluster where it has the maximum *PI*, signifying the cluster the signal has the strongest involvement with. All pixel pairs that do not belong to the same cluster have their PC set to 0 in the synchronization matrix. The eigenvalues and eigenvectors are then determined again and clusters reassigned using (4).

6.4.1.B Spectral Clustering

To improve upon limited accuracy of the eigendecomposition method in the presence of intercluster PC, Allefeld and Bialonski proposed to identify clusters from the synchronization matrix based on the concepts of spectral clustering. We outline the approach here and full details can be found in [21].

The first step is to normalize R with the L_1 norm to derive the matrix P, where the denominator is the sum of the jth column elements in R.

$$P_{mj} = \frac{R_{mj}}{\sum_w R_{wj}},$$

(5)

Clusters are defined based on the connectivity within the matrix P over τ time steps determined through the eigenvalue decomposition of P. The eigenvalues and right and left eigenvectors (p and A, respectively) of P are determined, and the transition matrix over τ steps is found as P^τ using the spectral representation

$$P^\tau = \sum_k \lambda_k^\tau p_k A_k.$$

(6)

As τ increases, all eigenvalues go towards 0, except for the strongest that will always be equal to 1. A τ is desired that sends all eigenvalues to 0 except for the r strongest, where r is the number of clusters. Allefeld and Bialonski suggest determining the number of clusters by finding r that leaves the largest last remaining eigenvalue, λ_{r-1}^τ [21]. This is done by finding the time-scale factor F for the number of clusters, r.

$$F(r) = \frac{\ln|\lambda_r|}{\ln|\lambda_{r-1}|}$$

(7)

Once the appropriate time-scale is determined an eigenvector space is developed from (8), and k-means clustering is applied to this space to assign the clusters.

$$\vec{o}(j) = \left(|\lambda_k|^\tau A_{kj} \right), \quad k = 1,...q - 1. \tag{8}$$

6.4.1.C Non-Negative Matrix Factorization

Non-negative matrix factorization (NMF) reduces an *n* x *m* matrix V into two matrices W (*n* x *r*) and H (*r* x *m*) using an iterative computation subject to the constraint that all values in W and H are ≥ 0 [22]. In our study, V is the *n* x *n* symmetric synchronization matrix containing PC values all between 0 and 1, so that W and H will be of size *n* x *r* and *r* x *n*, respectively. *r* represents the rank of the reduced matrices to be determined. By varying the rank *r*, the number of clusters to be identified can be adjusted.

$$V \approx WH \tag{9}$$

NMF was performed with update equations based on the squared error between V and WH, (10), [23].

$$D = \left\| V - WH \right\|^2 \tag{10}$$

We used 100 initial starting points and varied *r* from 1 to 10. The difference in (10) for increasing the rank by one was used as the criterion for determining the cluster number [24]. When the result of increasing *r* by one was a change in the residual error ($|D_{r+1} - D_r|$) of less than 0.01 the number of clusters was set to *r*.

Because W and H are positive, only additive combinations are possible which can lead to sparse components being generated. This is applicable for our scenario where we want to identify independent clusters within the data, and is in contrast to the eigenvector approach which can have negative values with components that must be orthogonal.

To assign clusters, W is generally used to represent bases that can be used to reconstruct V from the encoding in H for a particular subject [25]. We have symmetry in the synchronization

106

matrix, making it unclear how W and H should be used to assign clusters. Therefore, we take the cluster that makes up the largest contribution of the data at each pixel to determine the cluster assignments, (11), where j represents the pixel and r the cluster. In this way, each pixel is assigned to the cluster that makes up the largest additive portion of the original PC. If W and H are sparse and there is separation between clusters, then the additive component from the strongest cluster should have a significant contribution.

$$Cluster(j) = \arg\max_r (W_{jr} H_{rj}) \tag{11}$$

6.4.2 Simulation Comparison

The simulation was designed to portray the expected features within our LSPI data. This consists of a 25 x 35 image containing 5 clusters, Fig. 4a. All pixels within a cluster have significant PC with one another at a fixed value of 0.9. Intercluster PC was then added between all pairs of pixels not belonging to the same cluster with a magnitude related to the distance between the two pixels in Fig. 4a.

From our data, we observe a relationship between PC and the distance between two pixels, and use that to represent the intercluster PC in our simulation. A group of 20 pixels from the PC maps of the LSPI data were selected and a 2nd order polynomial was fit to the PC values with all other pixels as a function of the distance between them. To determine the accuracy of the clustering methods for varying levels of background noise, the 2nd order polynomial was multiplied by 0 to 1 in steps of 0.2. For an offset of 0.8, the synchronization matrix containing the fixed PC values within clusters and intercluster PC is shown in Fig. 4b.
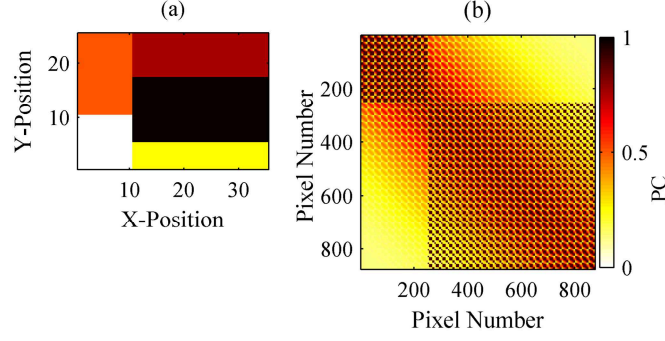
Figure 6.4 - Cluster map and synchronization matrix for simulation.
(a) Configuration of the cluster map for the simulation. Each color represents a cluster. (b) Synchronization matrix obtained by setting phase coherence between pairs of pixels belonging to the same cluster equal to 0.9. Phase coherence between all other pixel pairs was set as a function of the distance between the 2 pixels in (a).

The 3 clustering methods were applied to the synchronization matrix in Fig. 4b as the level of intercluster PC was varied. The residual error from NMF at each rank is plotted in Fig. 5a. The error reaches an approximate minimum at the correct cluster number, 5, until intercluster PC reaches 1.0. The difference in the residual error for adding one more cluster is plotted in Fig. 5b, where again it can be seen that the difference in error has little change after increasing the rank beyond the correct cluster number. We used a threshold of less than a 0.01 change in the residual error from adding one additional cluster to set the cluster number.
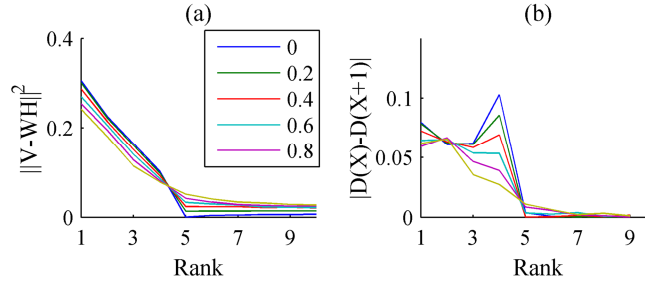
Figure 6.5 - Residual error for increasing rank in cluster simulation.
(a) Residual error (D) from non-negative matrix factorization for the selected rank. Each line represents the noise level. (b) Absolute value of the difference in residual error for increasing the number of clusters by 1.

Fig. 6a shows the number of clusters identified using the 3 methods. Spectral clustering and NMF approaches provide the correct number of clusters until intercluster PC is greater than the fixed within-cluster PC.

108
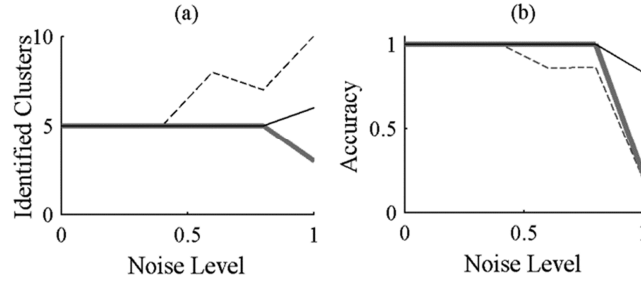
Figure 6.6 - Cluster simulation results.
(a) The number of unique clusters identified for increasing levels of intercluster PC using three clustering methods (thin dashed line: eigenvector decomposition, thick gray line: spectral clustering, thin black line: non-negative matrix factorization). (b) The ratio of the number of pixels assigned to the correct cluster using each of the 3 methods.

Fig. 6b shows the accuracy of each approach, defined as the number of pixels correctly assigned to its respective cluster out of the total number of pixels. If two clusters merged into a single cluster, only the larger of the two was said to be correctly assigned. Spectral clustering and NMF correctly assign all clusters until the noise level is greater than the within-cluster PC, but the eigendecomposition approach loses accuracy at a low level of intercluster PC.

6.4.3 Detection of Clusters in Renal Perfusion Data

PC values as determined in section III.B between all pairs of pixels from our LSPI data of the renal cortex were transformed into a single synchronization matrix and the three clustering methods were applied. Fig. 7a shows the frequency with the maximum spectral power in the MR frequency range for the time-series extracted from each pixel. Fig. 7b-e displays cluster maps using each of the approaches. NMF results are shown for 2 and 3 clusters. For all approaches, clusters <9 adjacent pixels in size are ignored, as this size can correspond to the Gaussian spatial filter. All methods separate the two groups of PC values seen in Fig. 2 similar to the frequency distribution in Fig. 7a. The two large clusters take up areas corresponding to ~8.12 mm^2 and 17.2 mm^2. Eigendecomposition identified a 3rd cluster in the lower left hand corner that is not

identified using spectral clustering or NMF. When increasing the NMF to rank 3, the larger of the 2 clusters divides into 2 clusters.
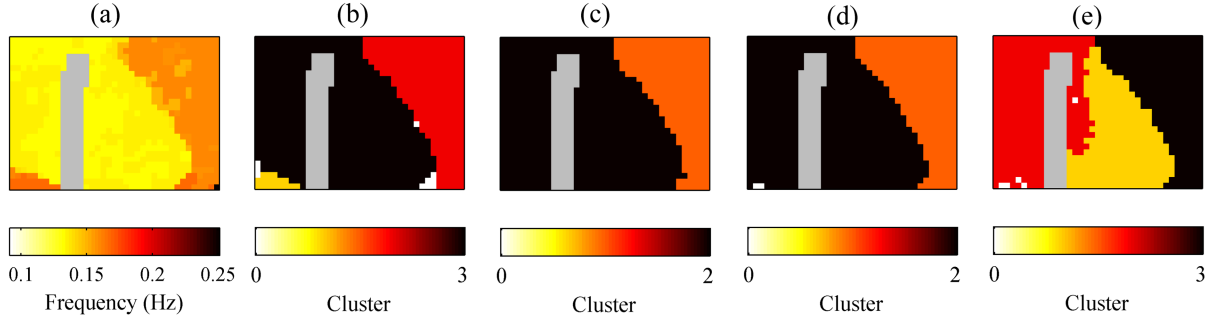
Figure 6.7 - Clustering approaches applied to renal perfusion data.
(a) Frequency with the highest spectra power within the myogenic response range (0.09 – 0.3 Hz) at each pixel location. Cluster maps identified with: (b) eigendecomposition, (c) spectral clustering, (d) non-negative matrix factorization with rank of 2, (e) non-negative matrix factorization with rank of 3. Pixels with the same color are assigned to the same cluster. Data are for same animal as in Fig. 1 and 2.

6.5 Experimental Results

LSPI was acquired for a set of 6 animals after L-NAME infusion for ~5 min each. L-NAME is a vasoconstrictor that has been shown to increase the amplitude of the MR [26, 27]. Figs. 8a&b show the dynamic characteristics, dominant frequency and detection ratio respectively, of the MR signal at each pixel for one animal. To demonstrate the unique information that is obtained by using PC to cluster compared to only frequency information, Fig. 8c presents the clusters formed using the expectation-maximization algorithm [28] on the frequency map in Fig. 8a. Fig. 8d presents the clusters formed by the PC statistics and NMF clustering. In each clustering map, two white stars are marked that share the same dominant frequency. Using frequency based clustering, Fig. 8c, these two locations belong to the same cluster but using PC statistics they belong to different clusters. Fig. 9a&b show PC maps for the 2 locations. The two locations do not have significant PC with each other, and the locations they do have significant PC with correspond to the PC cluster map in Fig. 8d. It has previously been shown that the renal autoregulation dynamics are highly time-varying [18], and the time-variance

110

for the two locations can be visualized in the time-frequency representations, generated by Variable Frequency Complex Demodulation [29], in Figs. 9c&d. Even though the locations share the same dominant frequency the time-variance of each differs and therefore PC, which tracks how consistent the phase relationships are over time, is not significant between the two. Although two renal perfusion signals may share the same dominant frequency this is not enough to determine if they are coupled.
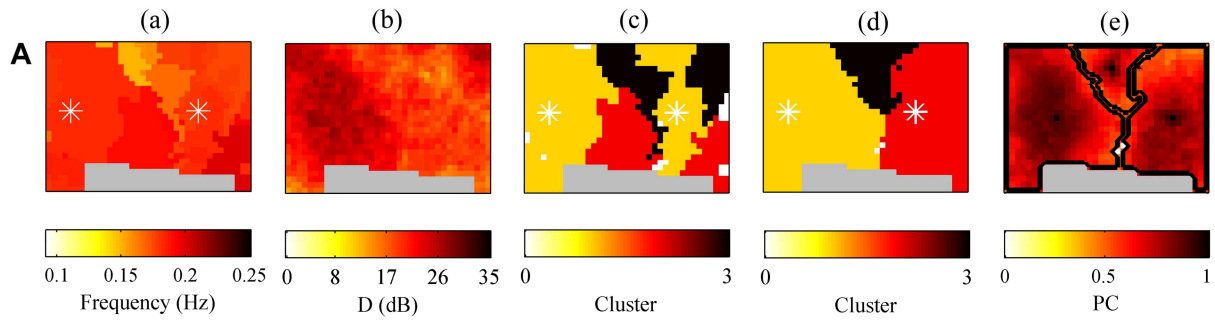
Figure 6.8 - Dynamics across the surface.
(a) Myogenic response frequency at each pixel location. (b) detection ratio of myogenic signal (c) clustering of frequency map in (a) using expectation-maximization algorithm, (d) clustering of same data using phase coherence with non-negative matrix factorization, (e) phase coherence map for clusters in (d) with phase coherence between each pixel and the pixel at the geometric centroid of the cluster it belongs to.
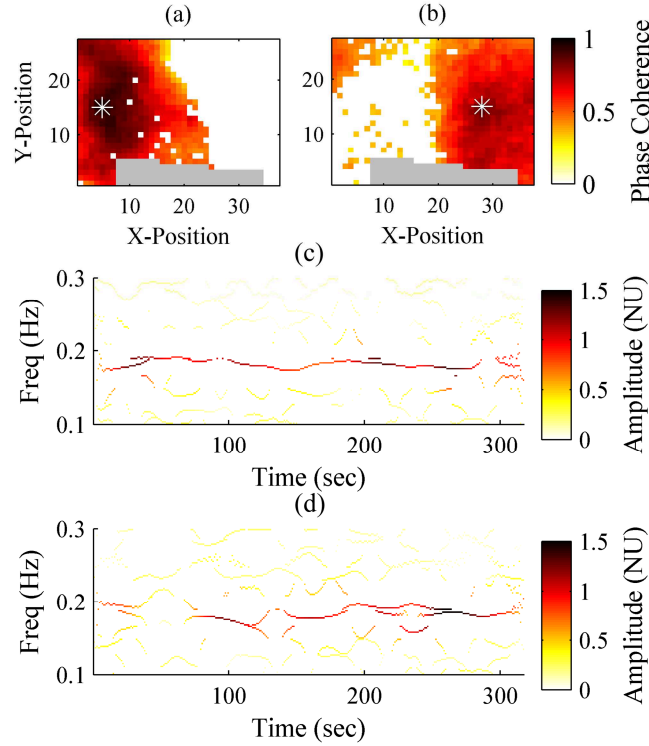
Figure 6.9 - Time-variance in renal autoregulation dynamics.
(a) Phase coherence between time-series from pixel marked by the white star and all other pixel time-series. White space indicates locations that do not have significant phase coherence with the white star location. (b) Phase coherence between pixel with white star and all other pixels. (c) Time-frequency spectrum in the myogenic response frequency range for the time-series from the white star location in (a). Time-frequency spectra in the myogenic response frequency range for the time-series from the white star location in (b).

The MR dynamic characteristics across the surface and PC with NMF clustering results are shown in Fig. 10 for the remaining 5 animals. Each row represents a different animal labeled by a letter. The first animal for this group (A) is shown in Fig. 8. Each row contains the dominant frequency in the MR range mapped at each pixel, detection ratio of that frequency, clustering map, and PC for each pixel with the pixel at the geometric centroid of the cluster it belongs to.
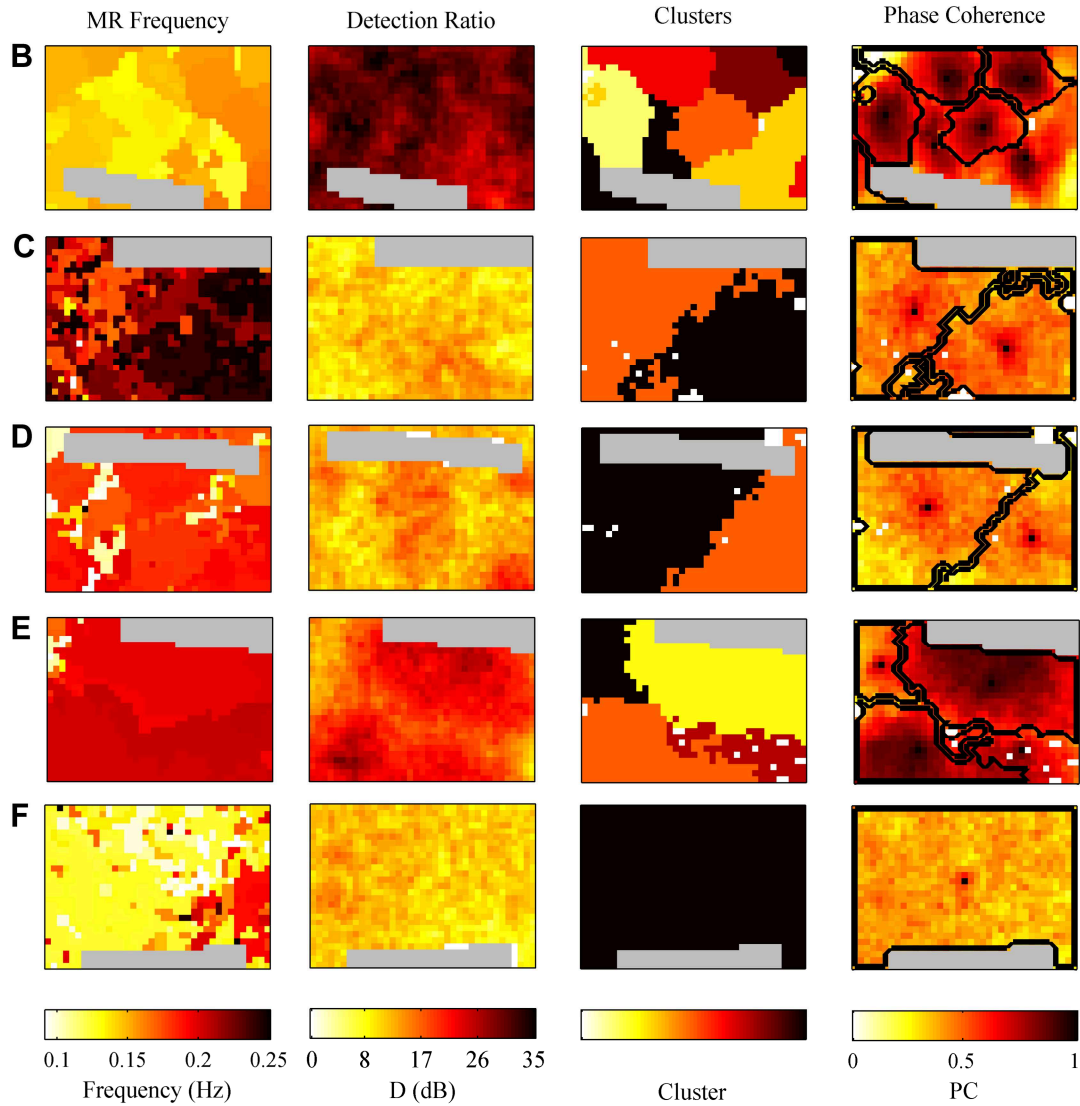
Figure 6.10 - Signal characteristics and identification of phase synchronized regions.
Characteristics of the myogenic response signal and phase coherence based clustering for the 5 remaining animals (rows B-F) during L-NAME infusion. The first column contains the peak myogenic response frequency, second column the detection ratio for that frequency relevant to background noise, third column are the maps of clusters determined using non-negative matrix factorization, and the fourth column are maps of the phase coherence relative to the signal at the geometric centroid of each cluster.

Characteristics of the clusters were quantified and compared to the detection ratios of the dynamics in Fig. 11. PC averaged between all pairs of pixels within each cluster (PC_{MEAN}) is shown on the y-axis in Fig. 11a with the x-axis representing the detection ratio averaged across all pixels within that cluster. It is seen that a higher detection ratio tends to correspond to higher

113

PC$_{MEAN}$. The approximate physical areas (mm^2) corresponding to each cluster are presented in Fig. 10b against the detection ratio.
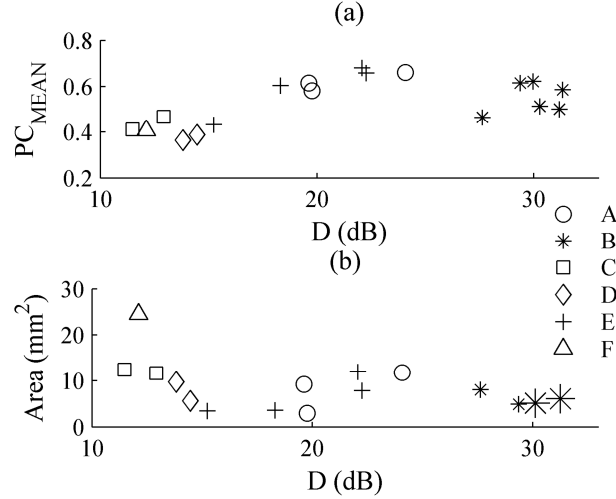
Figure 6.11 - Characteristics of the identified clusters for the 6 animals after L-NAME infusion. Each animal is designated by a different symbol labeled by the letter corresponding to the row in Figs. 7&9 and the results are plotted for each cluster from that animal. (a) Average phase coherence within each cluster versus the detection ratio averaged over all time-series from the pixels within that cluster. (b) Measured physical area of each cluster versus the average detection ratio. The larger stars represent 2 overlapping data points.

Animals A, B, and E form the most clusters with the highest PC$_{MEAN}$. These animals also have the strongest detection ratios. Animal B forms more clusters than A or E, but the field of view is larger for B and clusters are similar in physical size.

6.6 Discussion

We have presented an approach for identifying phase synchronized regions in LSPI of the renal cortex by clustering phase coupling coefficients between all pairs of pixels. A surrogate data threshold was applied to determine if pairs of pixels had significant PC. Three clustering methods were compared and when intercluster PC was low any of the methods provided accurate detection of clusters in our simulation. As intercluster PC increased, the eigendecomposition approach failed but both spectral clustering and NMF were able to identify the correct clusters

until a high background level of PC was present. When applying the method to renal autoregulation data, clusters with phase synchronized MR dynamics were identified.

Holstein-Rathlou *et al.* showed that with LSPI the TGF dynamics in the superficial vasculature could be tracked across the renal cortex [5]. They clustered the time-varying dynamics across the surface using hierarchical clustering [5] to find signal pairs with similar time-variance. In the present study we extended the analysis of phase coupling across the renal surface to identify phase coupled regions and generate an image of the segmentation of perfusion dynamics across the surface. The applied clustering algorithms utilize only the PC coefficients without any spatial information. Even so, clusters were identified amongst adjacent pixels.

The dynamics present in LSPI are representative of flow patterns in renal cortical blood flow and the renal autoregulation dynamics generated in the preglomerular vasculature are present in such signals [11]. Synchronization between pairs of nephrons connected in the preglomerular vasculature across distances up to 600 μm has previously been reported [3]. Our identified phase synchronized regions are larger than this. Efferent arterioles leave the glomerulus and approach the renal surface where they can diverge into a series of vessels producing a 'star' structure [2]. Efferent vessels from a single nephron can take up an area ~500um diameter across the renal surface in dog kidneys and travel some distance (~1 mm) from the glomerulus they originate from [2]. Efferent 'star' vessels contain renal autoregulation oscillations generated in the nephron [30]. From the penetration depth of the lasers in this study and placement of 'star' vessels in the subcapsule region they are likely the predominant contributors to laser Doppler and speckle signals of renal cortical blood flow [5, 31]. In this way, two nephrons connected by preglomerular vasculature at a distance up to 600 μm may have efferent star vessels that take up a significantly larger space on the renal surface that we are

115

capturing with LSPI. It is likely that additional nephrons synchronize their activity so that clusters are formed beyond the pairs previously studied as many afferent arterioles branch off of a single cortical radial artery. Using LSPI and the presented approach allows us to explore the extent of phase synchronization in renal cortical blood flow across a larger scale than previously available. The functional information that can be obtained from LSPI as presented in this report does not provide us with the structure of the underlying vasculature but we can determine that phase coupled surface perfusion regions exist and map their distribution. By combining our approach with anatomical imaging, such as by microtomography, clusters could be traced back to determine the configuration of the connecting vasculature.

The detectable cluster size is bound by our effective pixel resolution and field of view allowed by the moorFLPI imaging system. In this study our field of view was set at ~5mm x 7mm corresponding to approximately one-third of the posterior surface of the kidney. Holstein-Rathlou *et al.* identified 50-60 superficial star vessels across the full renal surface [5], so that within our current field of view 15-20 star vessels may be present. By reducing the zoom we could capture the entire surface, but in doing so would increase the size of our effective spatial resolution. As presented, this resolution is set to capture flow in efferent star vessels related to individual nephron dynamics that are considered to be the independent unit contributing to clusters.

Because of the noise in a single flux pixel it is necessary to average additional pixels [17] to acquire the autoregulation dynamics which reduces our effective spatial resolution. Without a high detection ratio we generate low PC estimates, Fig. 3b. When low detection ratios were present in real data, Fig. 9 C, D, and F, the surfaces were segmented into 1 or 2 clusters with low PC amongst the pixels in each cluster. These clusters should not be interpreted as being phase

coupled, as the PC is low and without a strong signal the coupling coefficients are more representative of noise than anything related to the MR. Signal quality must be considered when interpreting clusters.

PC has been widely applied for comparing the synchronization between two signals with known frequency content [13]. In renal autoregulation this is appropriate because we have two distinct frequency ranges of interest, those of the MR and TGF. We can band-pass filter over either frequency range to isolate the dynamic of interest and compute PC. Although PC is bound between 0 and 1, those values are rarely reached with real data and the interpretation of what value signifies significant phase coupling between these points is unclear [12]. For this reason, we used the concept of surrogate data to determine what the expected level of PC would be for uncoupled signals with the same time-varying dynamics. This preserves the power spectrum and statistical properties of the signal and provides a threshold for when it is known that there is no consistent phase relationship over time between the two signals [12]. We found it takes at least 20 oscillations to determine significant PC using the surrogate data approach. This translates to ~3 – 5 min of data for the MR or ~20 – 25 min for TGF. For this reason, we only investigated the MR in this paper. Given longer data sets, phase coupling in the TGF region can be estimated alongside the MR.

The eigendecomposition approach proposed by Allefeld *et al.* [14] for clustering bivariate synchronization indices provided accurate results when intercluster PC was limited. By applying the surrogate data threshold we can, in many instances, limit intercluster PC by setting the value to 0 when it does not pass the significance test. Intercluster PC can come from clusters having weak coupling with each other, signals that may have similar dynamics but without any physical coupling, or background noise. The surrogate data approach should remove pairs that have

coupling with similar dynamics or background noise. What to do in the case of weak coupling between clusters depends on the intent of any particular study.

We investigated multiple clustering approaches in the presence of high intercluster phase coherence. Our simulations showed that as intercluster PC increases the spectral clustering approach or NMF accurately detect clusters when eigendecomposition fails. As with any clustering problem, the question is then determining the correct cluster number. Using 3 clusters in NMF resulted in the larger of the 2 clusters in Figure 7 splitting into 2. This is expected since the PC is higher between neighboring pixels, even within the same cluster, so that the error will be lower by breaking large clusters into more localized components. This can be interpreted as over fitting to a higher number of clusters than actually present.

6.7   Conclusion

We have presented an approach to segment perfusion signals from across the renal surface generated by LSPI into phase synchronized clusters. From our experimental data, the renal surfaces were segmented into regions with high coupling when strong dynamics were present. Dynamics present in surface perfusion signals are generated by the renal autoregulation mechanisms at the nephron level and synchronization across a large region of the renal surface signifies coupled activity among a number of nephrons. It is known that electrotonic and hemodynamic coupling can exist between nephrons, but the extent of such coupling and the role coupling plays in renal autoregulation are largely unknown. LSPI provides functional information about renal cortical blood flow patterns and combining this technique with anatomical imaging would lead to better descriptions of the vascular components that contribute to clusters. The presented approach can be used as a research tool to enable studies to determine

the factors that influence phase synchronization across the renal surface and understand how

synchronization of nephrons contributes to the regulation of kidney blood flow.

6.8   References

[1]   Cupples, W.A. and B. Braam. Assessment of renal autoregulation. *American Journal of Physiology. Renal Physiology*. 292:F1105-F23, 2007.

[2]   Beeuwkes III, R. Efferent vascular patterns and early vascular-tubular relations in the dog kidney. *American Journal of Physiology*. 221:1361-74, 1971.

[3]   Yip, K.P., N.H. Holstein-Rathlou and D.J. Marsh. Dynamics of TGF-initiated nephron-nephron interactions in normotensive rats and SHR. *American Journal of Physiology. Renal Physiology*. 262:F980-F88, 1992.

[4]   Holstein-Rathlou, N.H. Synchronization of proximal intratubular pressure oscillations: evidence for interaction between nephrons. *Pflügers Archiv European Journal of Physiology*. 408:438-43, 1987.

[5]   Holstein-Rathlou, N.H., O.V. Sosnovtseva, A.N. Pavlov, W.A. Cupples, C.M. Sorensen and D.J. Marsh. Nephron blood flow dynamics measured by laser speckle contrast imaging. *American Journal of Physiology. Renal Physiology*. 300:F319-F29, 2011.

[6]   Marsh, D.J., I. Toma, O.V. Sosnovtseva, J. Peti-Peterdi and N.-H. Holstein-Rathlou. Electrotonic vascular signal conduction and nephron synchronization. *American Journal of Physiology. Renal Physiology*. 296:F751-F61, 2009.

[7]   Postnov, D., D. Postnov, D. Marsh, N.H. Holstein-Rathlou and O. Sosnovtseva. Dynamics of nephron-vascular network. *Bulletin of Mathematical Biology*. 1-22, 2012.

[8]   Marsh, D.J., A.S. Wexler, A. Brazhe, D.E. Postnov, O.V. Sosnovtseva and N.-H. Holstein-Rathlou. Multinephron dynamics on the renal vascular network. *American Journal of Physiology. Renal Physiology*. 304:F88-F102, 2013.

[9]   Cupples, W.A. Interactions contributing to kidney blood flow autoregulation. *Current Opinion in Nephrology and Hypertension*. 16:39-45, 2007.

[10]   Boas, D.A. and A.K. Dunn. Laser speckle contrast imaging in biomedical optics. *Journal of Biomedical Optics*. 15:011109-12, 2010.

[11]   Scully, C.G., N. Mitrou, B. Braam, W.A. Cupples and K.H. Chon. Detecting physiological systems with laser speckle perfusion imaging of the renal cortex. *American Journal of Physiology. Regulatory, Integrative and Comparative Physiology*. 304(11): R929-39, 2013.

[12]   Hurtado, J.M., L.L. Rubchinsky and K.A. Sigvardt. Statistical method for detection of phase-locking episodes in neural oscillations. *Journal of Neurophysiology*. 91:1883-98, 2004.

[13]   Mormann, F., K. Lehnertz, P. David and C. E Elger. Mean phase coherence as a measure for phase synchronization and its application to the EEG of epilepsy patients. *Physica D: Nonlinear Phenomena*. 144:358-69, 2000.

[14]   Allefeld, C., M. Müller and J. Kurths. Eigenvalue decomposition as a generalized synchronization cluster analysis. *International Journal of Bifurcation and Chaos*. 17:3493-97, 2007.

[15]   Bezemer, R., M. Legrand, E. Klijn, M. Heger, I.C. Post, T.M. van Gulik, D. Payen and C. Ince. Real-time assessment of renal cortical microvascular perfusion heterogeneities using near-infrared laser speckle imaging. *Optics Express*. 18:15054-61, 2010.

[16]   O'Doherty, J., P. McNamara, N.T. Clancy, J.G. Enfield and M.J. Leahy. Comparison of instruments for investigation of microcirculatory blood flow and red blood cell concentration. *Journal of Biomedical Optics*. 14:034025-13, 2009.

[17]   Bricq, S., G. Mahé, D. Rousseau, A. Humeau-Heurtier, F. Chapeau-Blondeau, J. Rojas Varela and P. Abraham. Assessing spatial resolution versus sensitivity from laser speckle contrast

imaging: application to frequency analysis. *Medical and Biological Engineering and Computing*. 50:1017-23, 2012.

[18] Chon, K.H., Y. Zhong, L.C. Moore, N.H. Holstein-Rathlou and W.A. Cupples. Analysis of nonstationarity in renal autoregulation mechanisms using time-varying transfer and coherence functions. *American Journal of Physiology. Regulatory, Integrative and Comparative Physiology*. 295:R821-R28, 2008.

[19] Scully, C.G., K.L. Siu, W.A. Cupples, B. Braam and K.H. Chon. Time–frequency approaches for the detection of interactions and temporal properties in renal autoregulation. *Annals of Biomedical Engineering*. 41:172-84, 2013.

[20] Siu, K.L. and K.H. Chon. On the efficacy of the combined use of the cross-bicoherence with surrogate data technique to statistically quantify the presence of nonlinear interactions. *Annals of Biomedical Engineering*. 37:1839-48, 2009.

[21] Allefeld, C. and S. Bialonski. Detecting synchronization clusters in multivariate time series via coarse-graining of Markov chains. *Physical Review E*. 76:066207, 2007.

[22] Lee, D.D. and H.S. Seung. Learning the parts of objects by non-negative matrix factorization. *Nature*. 401:788-91, 1999.

[23] Berry, M.W., M. Browne, A.N. Langville, V.P. Pauca and R.J. Plemmons. Algorithms and applications for approximate nonnegative matrix factorization. *Computational Statistics & Data Analysis*. 52:155-73, 2007.

[24] Devarajan, K. Nonnegative Matrix Factorization: An Analytical and Interpretive Tool in Computational Biology. *PLoS Computational Biology*. 4:e1000029, 2008.

[25] Brunet, J.P., P. Tamayo, T.R. Golub and J.P. Mesirov. Metagenes and molecular pattern discovery using matrix factorization. *Proceedings of the National Academy of Sciences of the United States of America*. 101:4164-69, 2004.

[26] Sosnovtseva, O.V., A.N. Pavlov, O.N. Pavlova, E. Mosekilde and N.H. Holstein-Rathlou. The effect of L-NAME on intra- and inter-nephron synchronization. *European Journal of Pharmaceutical Sciences*. 36:39-50, 2009.

[27] Shi, Y., X. Wang, K.H. Chon and W.A. Cupples. Tubuloglomerular feedback-dependent modulation of renal myogenic autoregulation by nitric oxide. *American Journal of Physiology. Regulatory, Integrative and Comparative Physiology*. 290:R982-R91, 2006.

[28] Moon, T.K. The expectation-maximization algorithm. *Signal processing magazine, IEEE*. 13:47-60, 1996.

[29] Wang, H., K.L. Siu, K. Ju and K.H. Chon. A high resolution approach to estimating time-frequency spectra and their amplitudes. *Annals of Biomedical Engineering*. 34:326-38, 2006.

[30] Holstein-Rathlou, N.H. and P.P. Leyssac. Oscillations in the proximal intratubular pressure: a mathematical model. *American Journal of Physiology. Renal Physiology*. 252:F560-F72, 1987.

[31] Smedley, G., K.P. Yip, A. Wagner, S. Dubovitsky and D.J. Marsh. A laser Doppler instrument for in vivo measurements of blood flow in single renal arterioles. *Biomedical Engineering, IEEE Transactions on*. 40:290-97, 1993.

Chapter 7: An Approach to Detect Quadratic Phase Coupling Between the Renal Autoregulation Mechanisms in Time and Space

7.1   Introduction

Higher-order spectral analysis can provide insight into the non-linear interactions between physiological systems. While the power spectrum describes the frequencies present in a recorded signal, it cannot be used to investigate interactions between components of that signal because it suppresses phase information [1]. The bispectrum preserves phase information and can identify phase relationships between components of a signal [2]. In physiological systems, non-linear interactions may include one system modulating the amplitude or frequency of another [3]. Amplitude modulation (AM) results in two sinusoids with frequency f and phase φ generating a third sinusoid with a frequency and phase equal to $f_1 + f_2$ and $\varphi_1 + \varphi_2$, respectively. The phase relationship of the third sinusoid relative to the first two defines the interaction between components 1 and 2 as quadratic phase coupling (QPC). Frequency modulation (FM) of one signal by another will also result in the generation of a third sinusoid with a frequency at $f_1 + f_2$ but without the phase equal to $\varphi_1 + \varphi_2$, and this is defined as quadratic frequency coupling (QFC). QPC implies QFC, but QFC can occur without QPC [4].

Renal autoregulation contains at least two mechanisms that operate to attenuate blood pressure (BP) fluctuations in nephrons [5]. Both mechanisms oscillate within frequency regions identified from single nephron laser Doppler recordings [6]. Tubuloglomerular feedback (TGF) operates within a range of 0.02 – 0.06 Hz, and the myogenic response (MR) operates within a range of 0.1 – 0.3 Hz [6]. The two mechanisms each act to constrict and dilate the afferent arteriole preceding each nephron producing an inherent TGF-myogenic interaction [7].

Volterra-Wiener analysis of total renal blood flow (RBF) under forced BP conditions first showed that the TGF-myogenic interaction was non-linear [8]. Wavelet analysis of single nephron laser Doppler signals during spontaneous blood pressure showed that TGF modulates the amplitude and frequency of the MR [9-11]. TGF control over the MR represents coordination between the two mechanisms possibly indicating efficient renal autoregulation [10].

It is believed that the interactions occur at the individual nephron level so when fluctuations are additively combined between nephrons, such as in RBF recordings, the interaction in any one nephron will be filtered out [12]. Using a time-invariant bispectrum detector, the TGF-myogenic interaction was identified in tubule pressure signals for normotensive rats as QPC but not in spontaneously hypertensive rats (SHRs) [12]. The lack of detection in SHRs was believed to be caused by their time-varying dynamics resulting in the interaction occurring over time instances shorter than what could be detected [12]. A time-varying bispectrum detector was developed and applied to renal autoregulation to identify QFC but could not discriminate QPC [4]. The results showed that periods of QFC could be detected in tubule pressure as well as RBF in normotensive and SHRs [4]. Since the study only tested for QFC, it could not be determined if the non-linear interaction was only QFC, which could be FM, or also may have included QPC, which could represent AM.

Therefore, differentiating QFC and QPC in renal autoregulation is restricted by the acquisition of signals related to flow in a limited number of nephrons as well as the time-varying nature of renal autoregulation dynamics. Laser speckle perfusion imaging (LSPI) can monitor locations across the renal cortex simultaneously to acquire local flow dynamics. Time-varying detectors have been proposed that provide short-time QPC detection [13-15].

122

In this study a wavelet bicoherence detection procedure is modified to identify QPC between the TGF and MR over short time periods. The statistical properties of the detector are shown using simulation examples as is the ability to discriminate between AM and FM. The method is applied to RBF and LSPI to identify QPC at locations across the renal surface. The combination of our analytical procedure and LSPI allows QPC localization in time and space.

7.2   Quadratic Phase Coupling Detector

The time-invariant bispectrum can be estimated by the expected value of the triple Fourier transform (*X(f)*) product over K segments (1), where * represents the complex conjugate.

$$BS(f1, f2) = E[X(f_1)X(f_2)X^*(f_1 + f_2)] \tag{1}$$

The bicoherence is a normalized version of the bispectrum with values from $0 - 1$ and is estimated over *K* segments.

$$|BIC(f1, f2)| = \frac{|BS(f_1, f_2)|}{\sqrt{E[|X(f_1)X(f_2)|^2]E[|X(f_1 + f_2)|^2]}} \tag{2}$$

The magnitude of the bicoherence is often used as a detector for QPC using a 95% significance threshold based on the bicoherence estimate variance as a function of the number of segments used to estimate the bicoherence, defined by Elgar and Guza as $\sqrt{(6/2K)}$ where *K* is the number of segments [16, 17]. It has been shown that the bicoherence alone is not an appropriate indicator of QPC if the phases are not randomized across segments, as QFC without phase coupling will provide high bicoherence levels given constant phase relationships [15, 18]. Fackrell and McLaughlin showed the combination of the bicoherence and biphase statistical tests can discriminate cases of QPC [19]. When the biphase is close to 0 across segments and the bicoherence is high QPC can be declared. Bicoherence and biphase estimates and significance thresholds are a function of the number of segments analyzed. Usually at least 8 segments are

required to make a designation of QPC, so that relatively long data lengths are required for the detection of QPC. For this reason, time-varying detectors have been investigated [15].

The time-varying wavelet spectrum is defined as (3) where $x(t)$ represents the signal and ψ represents the wavelet function that is shifted throughout time and dilated at scales, s, to generate a spectral estimate across time and scales.

$$w(s,t) = \frac{1}{\sqrt{s}} \int_{-\infty}^{\infty} x(\tau)\psi^*\left(\frac{\tau - t}{s}\right) d\tau \tag{3}$$

The frequency of the wavelet spectrum is related to $1/s$. We use a Morlet wavelet with natural frequency of 6. Just as the time-invariant bispectrum can be determined by the expected value of the triple product of the Fourier transform in (1) over K segments, the wavelet bispectrum can be estimated at each time point by the integral of the wavelet spectrum as

$$WB(f_1, f_2, n) = \int_{n-T/2}^{n+T/2} w(f_1, \tau)w(f_2, \tau)w^*(f_1 + f_2, \tau)d\tau. \tag{4}$$

An integration time T is selected to estimate the wavelet bispectrum at each time location. Equivalent to (2), the wavelet bicoherence can then be estimated as

$$|WBIC(f_1, f_2, n)| = \frac{|WB(f_1, f_2, n)|}{\sqrt{\int_{n-T/2}^{n+T/2}|w(f_1, \tau)w(f_2, \tau)|^2 d\tau \int_{n-T/2}^{n+T/2}|w(f_1 + f_2, \tau)|^2 d\tau}}. \tag{5}$$

The wavelet bicoherence will be close to 1 when there is wavelet power at f_1, f_2, and f_{1+2} and the biphase at (f_1, f_2) is constant across the integration time. This can be used to define QFC. QPC requires a biphase $(\varphi_1 + \varphi_2 - \varphi_3)$ of 0.

Kim *et al.* proposed a procedure to randomize the biphase when estimating the time-invariant bicoherence by multiplying the biphase by a random variable, R, at each segment [18]. When the biphase is close to 0, as in the case of QPC, multiplying the biphase of each segment by a random variable will keep the biphase close to 0 so that a high bicoherence will remain.

When the biphase is not close to 0 but still constant across the segments, a situation that will generate a high bicoherence without the presence of QPC, the biphase will be randomized across segments when multiplied by the random variable resulting in a reduced bicoherence. Li *et al.* applied this approach to time-varying wavelet analysis to develop the phase-randomized wavelet bispectrum (WBPR)

$$WBPR(f_1, f_2, n) = \int_{n-T/2}^{n+T/2} |w(f_1, \tau)w(f_2, \tau)w^*(f_1 + f_2, \tau)|e^{iR(\tau)\varphi_d(f_1, f_2, \tau)}d\tau. \qquad (6)$$

ϕ_d represents the estimated biphase, and R the random variable at each time point multiplied by the biphase [15]. The phase-randomized wavelet bicoherence (WBICPR) is estimated as

$$|WBICPR(f_1, f_2, n)| = \frac{|WBPR(f_1, f_2, n)|}{\sqrt{\int_{n-T/2}^{n+T/2}|w(f_1, \tau)w(f_2, \tau)|^2 d\tau \int_{n-T/2}^{n+T/2}|w(f_1 + f_2, \tau)|^2 d\tau}}. \qquad (7)$$

To determine the significance of the phase-randomized wavelet bicoherence, Li *et al.* proposed a surrogate data approach by adding a random variable to the biphase prior to multiplying it by the random integer R [15]. This has the intended effect of shifting the biphase away from 0 when QPC is present, so that when the phase-randomization procedure is applied it estimates the bicoherence when the phase is randomized away from 0. However, adding a random variable to the biphase can sometimes shift the biphase towards 0 when it is not close to it, creating a bimodal distribution when generating multiple trials from surrogate data. We only want to determine the expected phase-randomized bicoherence when the biphase is away from 0 to determine a threshold. In this study, the biphase at each time point is replaced with a uniform random variable θ that is U[-π:-1,1:π]. The wavelet bispectrum for each surrogate trial is then

$$WBsurr(f_1, f_2, n) = \int_{n-T/2}^{n+T/2} |w(f_1, \tau)w(f_2, \tau)w^*(f_1 + f_2, \tau)|e^{i\theta(\tau)}d\tau. \qquad (8)$$

The phase-randomized bicoherence estimate is determined for X realizations of θ, and the mean plus 2 standard deviations at each time point are used as a threshold. This procedure provides the expected phase-randomized wavelet bicoherence given the signal dynamics without QPC.

Wavelet bicoherence, phase-randomized wavelet bicoherence and surrogate-derived thresholds are computed by first tracking the low and high dominant frequencies, f_1 and f_2, in the wavelet spectrum as the frequency corresponding to the maximum amplitude at each time point within that range. f_1 represents the TGF component $(0.02 - 0.06)$ Hz and f_2 the myogenic component $(0.1 - 0.[6]$. AM and FM operations will result in sum and difference frequencies in the power spectrum at $(f_1 + f_2)$ and $(f_1 - f_2)$, and a bispectrum peak at (f_1, f_2). Wavelet bicoherence values are tracked at the (f_1, f_2) pair across time to look for QPC between the TGF and myogenic mechanisms. Results are computed at this frequency pair as it varies over time for the designation of a non-linear interaction between the two mechanisms. Table I summarizes the detection procedure.

1	Estimate the wavelet spectrum and identify the maximum amplitude and corresponding frequency across the two frequency ranges: f_1=[0.02 – 0.06] and f_2=[0.1 – 0.3] Hz. (3)
2	Extract the wavelet coefficients $w(f_1, t)$ and $w(f_2, t)$
3	Compute the wavelet bicoherence and biphase at (f_1, f_2, t) (5)
4	Compute the phase-randomized wavelet bicoherence at (f_1, f_2, t) (7)
5	Compute X trials of the phase-randomized wavelet bicoherence surrogates (8) and use the mean plus two standard deviations over all trials at each time point to estimate the QPC threshold
6	Compare the phase-randomized wavelet bicoherence with the threshold to determine times with QPC

Table 7.1 - Procedure to detect time-varying quadratic phase coupling.

7.3   Materials and Methods

7.3.1   Detection Properties Simulation

Eq. 9 represents signals with and without QPC, a condition set by varying the properties of the third sinusoid.

$$sig(t) = A_1 \sin(2\pi f_1 t + \varphi_1) + A_2 \sin(2\pi f_2 t + \varphi_2) + A_3 \sin(2\pi f_3 t + \varphi_3) + r(t) \quad (9)$$

The test signal consists of 3 sinusoids with added white Gaussian noise, r. f_1 was set to 0.03 Hz and f_2 to 0.13 Hz, representative of the TGF and MR components, respectively, with phases φ_1 and φ_2 set as uniform random variables U[-π, π]. The frequency of the 3rd sinusoid, f_3, was set to the sum of the first 2, 0.16 Hz, to represent frequency coupling, and QPC was set by making φ_3 equal to $\varphi_1 + \varphi_2$ so that the biphase ($\varphi_1 + \varphi_2 - \varphi_3$) is equal to 0. Otherwise, when QPC was not present φ_3 was set as a uniform random variable U[-π, π]. A_1 and A_2 were set to 1, and A_3 was varied to represent the coupling strength.

30 signal sections, alternating with and without QPC, were concatenated together to generate signals with the time-varying presence of QPC. Section lengths were varied from [64, 128, 256, 512, 1024] sec. Signals at each length were generated with coupling amplitudes, A_3, varied from [0, 0.25 0.5, 0.75, 1.0].

The phase-randomized wavelet bicoherence was computed for each concatenated signal and coupling amplitude at (f_1, f_2, t). True positives were declared when the phase-randomized bicoherence was greater than the surrogate-derived threshold when QPC was present. True negatives were declared when the phase-randomized bicoherence was not greater than the threshold during periods when QPC was not present.

7.3.2 Amplitude and Frequency Modulation Simulation

This test is designed to determine if the proposed algorithm is able to specifically detect QPC (represented by AM) and not QFC (represented by FM). 4 signals (10 – 13) were developed to represent the following cases: Case 1: 2 independent signals without AM or FM, Case 2: the higher frequency sinusoid, f_2, is amplitude modulated by the lower, f_1, Case 3: f_2 is frequency modulated by f_1, Case 4: the f_2 is both amplitude and frequency modulated by f_1.

$$Case1(t) = \sin(2\pi f_1 t + \varphi_1) + \sin(2\pi f_2 t + \varphi_2) + r(t) \tag{10}$$

$$Case2(t) = (1 + \sin(2\pi f_1 t + \varphi_1)) * \sin(2\pi f_2 t + \varphi_2) + r(t) \tag{11}$$

$$Case3(t) = \sin\left(2\pi f_2 t + 2\pi * f_1 * \int_0^t \sin(2\pi f_1 \tau)\, d\tau\right) + r(t) \tag{12}$$

$$Case4(t) = (1 + \sin(2\pi f_1 t + \varphi_1)) * \sin\left(2\pi f_2 t + 2\pi * f_1 * \int_0^t \sin(2\pi f_1 \tau)\, d\tau\right) + r(t) \tag{13}$$

100 trials of each case were generated with random Gaussian white noise, r, and signal length of 1500 sec. f_1 was set to 0.03 Hz and f_2 to 0.13 Hz to represent the TGF and myogenic mechanisms, respectively. The amount of time the phase-randomized bicoherence was above the significance threshold was determined for each trial and the mean and standard deviation were computed over all trials. The number of trials with significant time-invariant bicoherence, biphase, and QPC were also determined using the statistical tests proposed in [16, 17, 19].

7.3.3 Experimental Data Collection

All experiments were approved by the Animal Care Committee of Simon Fraser University, in accordance with the guidelines of the Canadian Council of Animal Care. Male Long-Evans rats (Harlan, Livermore, CA, USA), aged 10-14 weeks were used. Anaesthesia was induced with 4% isoflurane in inspired gas (30% O_2, 70% air, 750 mL/min) and reduced to 2%. The trachea was cannulated and animals ventilated by a small animal respirator (TOPO, Kent

Scientific, Torrington, CT, USA) adjusted to match the natural breathing rate of each animal (~45 breaths per minute). The left femoral vein was cannulated (PE-50) for infusion of saline containing 2% bovine serum albumin (1% body weight per hour). A subcostal flank incision exposed the left kidney. Once freed from surrounding fat, the kidney was mounted in a plastic cup anchored to the table. Stopcock grease (Dow Corning, Midland, MI, USA) was placed in the cup to prevent motion and position the kidney towards the LSPI camera. The renal artery was stripped of fat and renal nerves. A transit time ultrasound flow probe (TS420, Transonic Systems, Ithaca, NY, USA) was mounted on the renal artery, secured with acoustic coupling gel (Surgilube and Nalco 1181), and recorded at a sampling rate of 500 Hz. There was a 1-hr post-surgery equilibration period.

Data were recorded in each animal under spontaneous blood pressure during control (CTL) conditions and non-selective nitric oxide synthesis (NOS) inhibition with intravenous infusion of N^ω-nitro-l-arginine methyl ester (L-NAME) (Sigma-Aldrich, Oakville, ON, Canada) at 10mg/kg$_{BW}$.

LSPI was performed with the moorFLPI imaging system (Moor Instruments, Axminster, UK) using an exposure time of 2 msec and flux computed over a spatial set of pixels (113x152 pixels at 25 Hz sampling rate). An ~4 mm hair was placed on the surface of the kidney, and the moorFLPI was positioned to capture the full hair in the viewing window resulting in the lens ~20 cm from the surface.

A Gaussian spatial filter was applied to each frame to increase the signal-to-noise ratio [20]. The image series were down sampled by a factor of 4 and the time-series from each pixel location were low-pass filtered to 0.5 Hz and down sampled to 1 Hz. A mean laser speckle signal was generated by averaging all pixels at each time frame. Renal blood flow (RBF) data were

low-pass filtered to 0.5 Hz and down sampled to 1 Hz. RBF, the mean laser speckle signal (LS$_{mean}$), and the time-series extracted from each pixel of the filtered image series were tested for the presence of QPC.

7.4   Simulation Results

7.4.1   Statistical Properties of Detector

The concatenated test signals contained segments from (9) alternating with and without QPC. Fig. 1 illustrates our approach by comparing the power spectrum and wavelet bicoherence results for a signal section with (top row) $\varphi_3 = \varphi_1 + \varphi_2$ to represent QPC and (bottom row) φ_3=U[-π, π]. Figs. 1a&e are the power spectra for the two scenarios. Three spectral peaks can be identified at the low frequency (f_1=0.03 Hz), high frequency (f_2=0.13 Hz), and sum of the low and high frequencies (f_3=0.16 Hz) in both spectra. No difference between the two segments can be discerned from the power spectra because phase relationships are suppressed. Fig. 1b represents the wavelet bicoherence spectrum at the time point with QPC and Fig. 1f represents the same for a time point without QPC. In both cases, the wavelet bicoherence is high in the area (0.03, 0.13) Hz and it is clear that this peak alone cannot discriminate between the two cases. Fig. 1c shows the absolute value of the wavelet biphase during QPC at the same time point as Fig. 1b. In this case, the biphase is close to 0 around (0.03, 0.13) Hz as expected. In Fig. 1g, the absolute value of the wavelet biphase is shown for the time point without QPC and is not close to 0. The wavelet biphase can discriminate between periods with and without QPC, but since the phases are constant across the integration time the bicoherence is high regardless of the state of QPC.

130
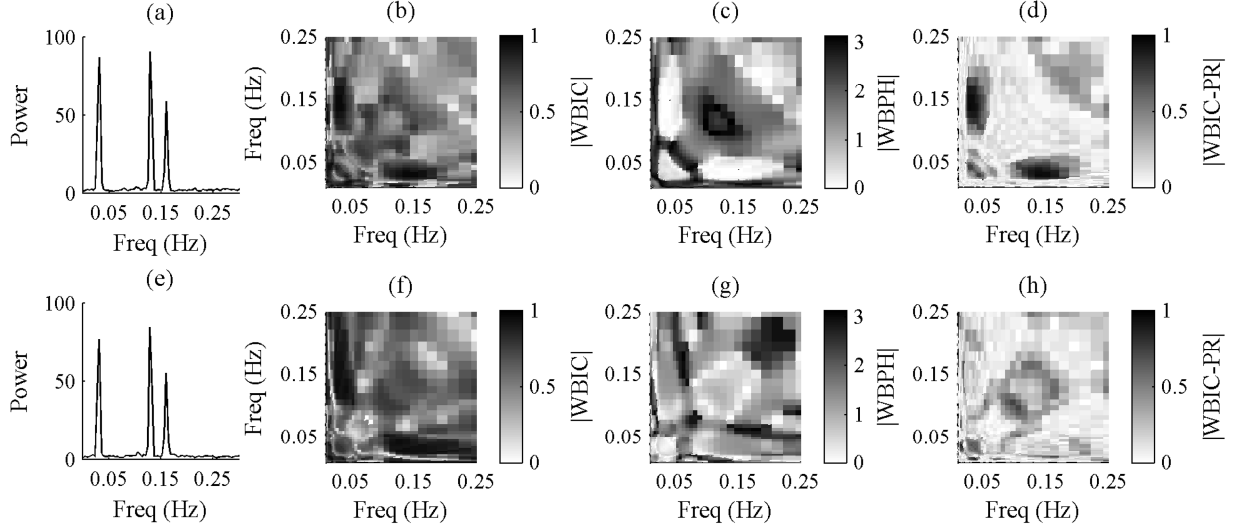
Figure 7.1 - Wavelet bicoherence spectra.
(a) and (e) are the power spectral densities for the test signal in (9) for the case of quadratic phase coupling ($\varphi_3 = \varphi_1 + \varphi_2$) and without quadratic phase coupling ($\varphi_3 = U[-\pi, \pi]$). (b) Wavelet bicoherence for the test signal at a time with quadratic phase coupling is present. (c) Absolute value of the wavelet biphase at the same time point. (d) Phase randomized wavelet bicoherence when quadratic phase coupling is present. (f) Wavelet bicoherence (g) biphase and (h) phase randomized wavelet bicoherence at a time point without quadratic phase coupling.

The phase-randomized bicoherence (7) during the two time points with and without QPC are shown in Figs. 1d&h, respectively. When QPC is present the phase randomized bicoherence still produces a high value in the area of (0.03, 0.13) Hz, Fig. 1d, but when the phases are not coupled there is no peak in the area of (0.03, 0.13) Hz, Fig. 1h. Multiplying the biphase at each time point by a random variable has little impact when the biphase is close to 0, so the bicoherence estimate remains high. When the biphase is constant but not close to 0, such as can happen in QFC, the random variable distorts biphase values so they are no longer constant across integration times.

The utility of the phase randomization procedure is further illustrated in Fig. 2. In this scenario, signal segments with and without QPC ranging in length from 2048 to 64 data points from (9) were concatenated together. The true state of QPC at each time point is shown by the dashed gray line in Fig. 2c. Fig. 2a shows the wavelet bicoherence, phase-randomized bicoherence and surrogate-derived threshold tracked at (0.03, 0.13) Hz across time. Wavelet bicoherence remains high across signal lengths since the frequency coupled component is always

present, Fig. 1b. The phase-randomized bicoherence is only high when biphase is close to 0, which occurs during periods with QPC. By comparing the phase-randomized bicoherence with surrogate-derived threshold, accurate detection of time points with QPC can be made for short data lengths as seen by the QPC decision in Fig. 1c (black line).
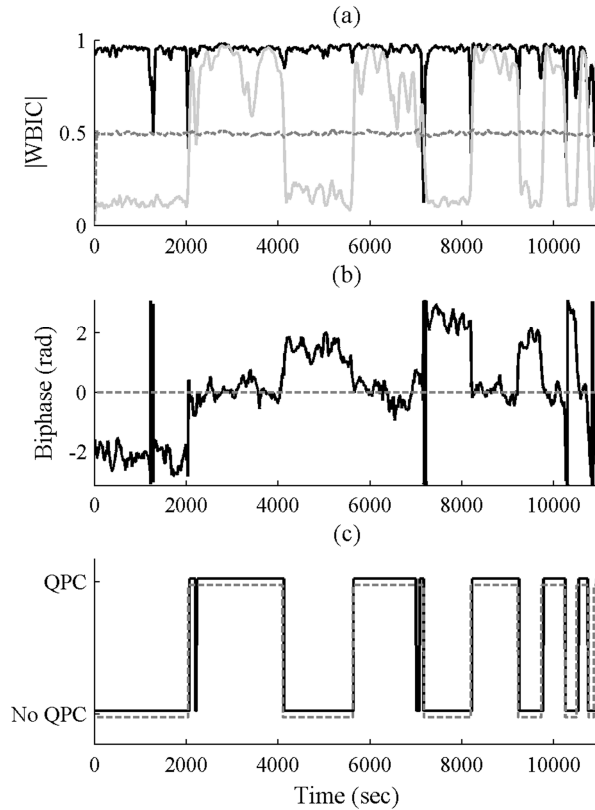
Figure 7.2 - Tracking the wavelet bicoherence.
Wavelet bicoherence results at (f_1, f_2) over time for test signal with alternating periods with or without the presence of quadratic phase coupling. (a) Wavelet bicoherence (black line), phase randomized wavelet bicoherence (light gray line) and surrogate data threshold (dashed gray line). (b) Wavelet biphase at (f_1, f_2). The true state of quadratic phase coupling is shown by the dashed gray line in (c), and the declared state based on the phase randomized surrogate data test is shown by the black line.

QPC detection was performed on the test signals described in III.A. The overall accuracies were found across coupling amplitude and lengths of QPC segments (not including coupling amplitudes of 0.0 or segment lengths of 64), Table II. An integration time of 100 sec provided the best accuracy over the various coupling amplitudes and segment lengths. The number of surrogate trials did not impact detection accuracy.

		Integration Time (sec)			
		10	50	100	200
Number of Surrogate Trials	20	50.0	71.5	75.4	73.8
	40	50.0	71.4	75.4	73.7
	60	50.0	71.5	75.4	73.7
	80	50.0	71.4	75.4	73.7

Table 7.2 - Accuracy of detecting quadratic phase coupling as a function of integration time and the number of surrogate trials.

Accuracy, sensitivity (rate of QPC detection when present) and specificity (rate of not detecting QPC when not present) as a function of the segment lengths and coupling amplitudes are shown in Fig. 3a-c, respectively, at an integration time of 100 sec using 40 surrogate trials.
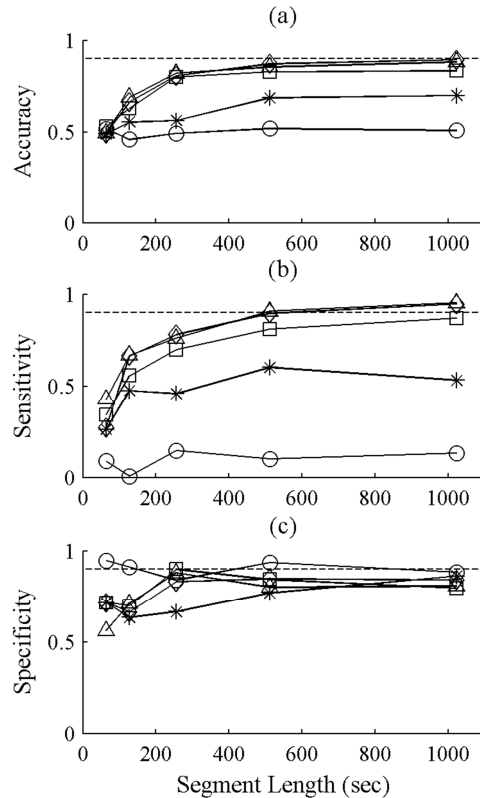
Figure 7.3 – Wavelet bicoherence detection properties for simulation.
(a) Accuracy, (b) sensitivity, (c) specificity for varying segment lengths and coupling amplitudes at an integration time of 100 sec and 40 surrogate trials. Lines on each plot represent the amplitude of the 3rd frequency component (circle 0.0, star 0.25, square 0.5, diamond 0.75, triangle 1.0). Dashed lines are at 0.9 for reference.

Sensitivity increases with increasing coupling amplitudes and segment lengths. At a coupling amplitude of 0, QPC is rarely detected. In this scenario the 3rd frequency is not present so we do

not expect to detect QPC. Specificity remains at ~85% across data lengths and coupling amplitudes. When the phase of the 3rd frequency component is set as a random variable, we expect it to equal the sum of the first two components on occasion which results in true negatives being detected.

7.4.2   Distinguishing Amplitude Modulation

Power spectra for the AM and FM signals (11-13) are shown in Fig. 4a-c. It is difficult to distinguish AM and FM cases from power spectra, Figs. 4a&b, as both present spectral components at $f_1 + f_2$ and $f_2 - f_1$. When AM and FM are simultaneously present the dynamics seen in the spectrum vary from the cases of only AM or FM, Fig. 4c.
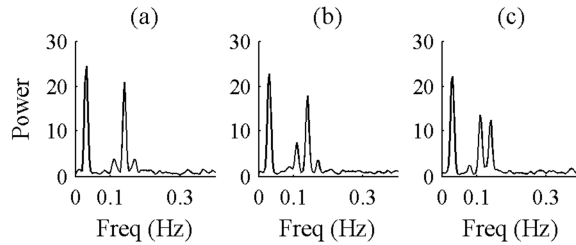
Figure 7.4 - Example power spectra of amplitude and frequency modulation simulations.
(a) amplitude modulation only, (b) frequency modulation only, (c) simultaneous amplitude and frequency modulation.

Wavelet bicoherence at (f_1, f_2) results for the 4 AM and FM cases (10-13) are shown in Fig. 5a-c for the 100 trials. In Cases 2 and 4, when AM is present the wavelet bicoherence is increased and the wavelet biphase is close to 0. There is significantly more QPC detected during Cases 2 and 4 (which include AM) than Case 3 (only FM).
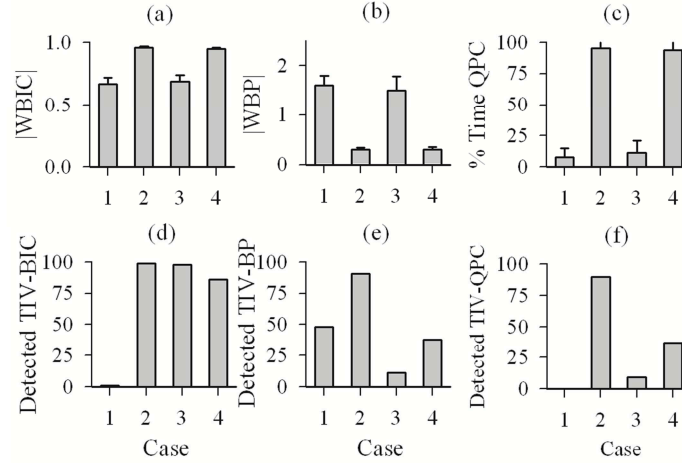
Figure 7.5 - Differentiation of amplitude and frequency modulation.
(a) Wavelet bicoherence, (b) biphase, (c) and the percent of time QPC was detected for 100 trials (mean ± SD) for the 4 cases of amplitude and frequency modulation (eqs. 10 – 13). Bottom row contains the detection results over the 100 trials using the time-invariant bicoherence: number of trials with significant (d) bicoherence, (e) biphase, and (f) quadratic phase coupling (significant bicoherence and biphase both detected).

The number of trials with significant time-invariant bicoherence, biphase, and QPC are shown in Fig. 5 d-f using the test described by Fackrell and McLaughlin [19]. The phase-randomized wavelet bicoherence test detected QPC, when AM alone was present (Case 2) and when AM and FM were simultaneously present (Case 4). Using the time-invariant test, Case 4 only identifies QPC in ~25% of the trials even though it is present alongside FM.

7.5   Experimental Results

7.5.1   Total Renal Blood Flow

A representative RBF recording for one animal after bolus infusion of L-NAME is shown in Fig. 6a with accompanying power spectrum in Fig. 6b. A weak TGF signal component can be seen at a low frequency component relative to the strong myogenic signal between 0.1 and 0.3 Hz. Two strong peaks are apparent in the MR range, and one may be generated by a non-linear interaction between the TGF and MR mechanisms. The wavelet bicoherence and phase-randomized wavelet bicoherence are computed at (f_{TGF}, f_{MYO}, t), where f_{TGF} and f_{MYO} are

determined by tracking the dominant amplitude in the respective frequency ranges. Fig. 6c shows the tracked wavelet bicoherence and phase-randomized wavelet bicoherence with its corresponding surrogate-derived threshold.
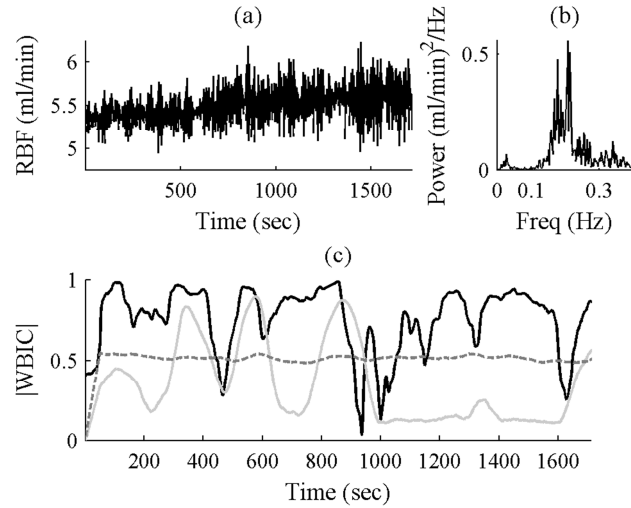
Figure 7.6 - Wavelet bicoherence analysis of renal blood flow.
(a) Renal blood flow signal after bolus infusion of L-NAME. (b) Power spectrum of the renal blood flow signal showing frequency content in the expected myogenic range, 0.1 – 0.3 Hz, and weak frequency content in the TGF range, ~0.02 Hz. (c) Wavelet bicoherence (black line), phase-randomized wavelet bicoherence (solid light gray line), and surrogate-derived threshold (dashed gray line) tracked at (f_{TGF}, f_{MYO}, t).

The wavelet bicoherence is high throughout most of the recording, but the phase-randomized bicoherence is only higher than the threshold for short time periods, when the light gray line (phase-randomized bicoherence) crosses the dark dashed gray line (threshold). This indicates the presence of transient QPC in total RBF.

LS_{mean}, average of all pixels across the ~5x7mm imaged surface, with accompanying power spectrum are shown in Fig. 7a&b for the same L-NAME monitoring period as the RBF signal in Fig. 6a. A stronger TGF frequency peak relative to the myogenic peak is seen for LS_{mean} compared to the total RBF signal. The wavelet bicoherence tracked at the TGF and MR frequencies is shown in Fig. 7c. Sparse, short periods with QPC are detected.
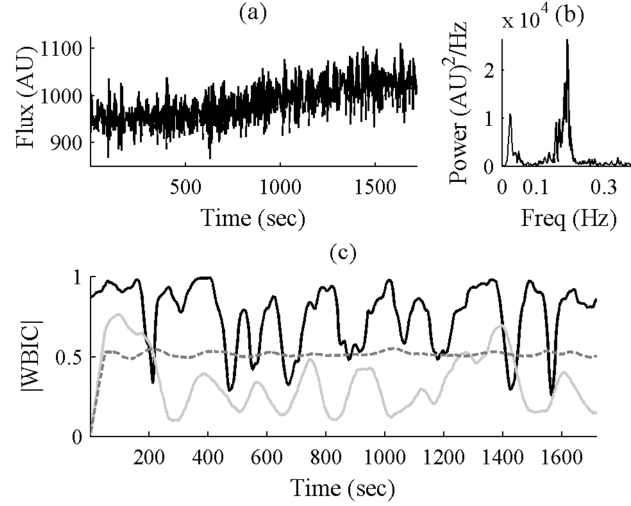
Figure 7.7 - Wavelet bicoherence analysis of LS$_{mean}$.
(a) Mean laser speckle signal generated by averaging all pixels at each frame for the same monitoring period as in Fig. 5. (b) Power spectrum of the laser speckle signal. (c) Wavelet bicoherence (black line), phase-randomized wavelet bicoherence (solid light gray line), and surrogate-derived threshold (dashed gray line) tracked at (f_{TGF}, f_{MYO}, t).

Grouped results for the amount of QPC during each recording for the 9 animals are shown in Table III. Segments with QPC shorter than the integration time of 100 sec were removed. The number of animals with significant QPC and the mean coupling time for these experiments are presented.

	Experiments with QPC		Mean QPC Time (%)	
	CTL	L-NAME	CTL	L-NAME
RBF	4	5	13.0 ± 5.6	15.8 ± 8.2
LS$_{mean}$	4	5	21.4 ± 9.6	11.6 ± 4.6

Table 7.3 - Quadratic phase coupling detected in renal blood flow and LS$_{mean}$.
Mean QPC times are for those experiments that had QPC > 0 sec after removal of segments that were significant for a period shorter than the integration time (100 sec). Mean ± SD. N=9.

Limited amounts of QPC were identified in both RBF and LS$_{mean}$. Bolus infusion of L-NAME did cause a significant change in QPC across animals.
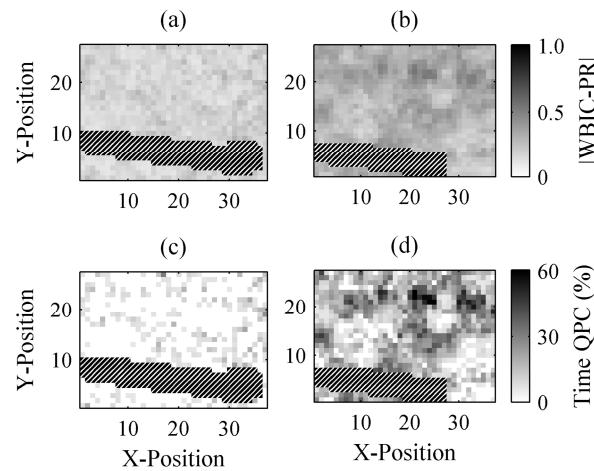
7.5.2 Quadratic Phase Coupling Across the Renal Surface

Total RBF and LS$_{mean}$ contain dynamics averaged over either all the nephrons in the kidney or within the imaging window. This will attenuate dynamics from any one nephron that

137

may display QPC. To test if localized QPC could be detected, the wavelet bicoherence analysis was applied to time-series extracted from each filtered pixel.

Time-averaged phase-randomized wavelet bicoherence during CTL and L-NAME periods for one animal at each pixel location are shown in Fig. 8a&b, respectively. During CTL, the phase-randomized wavelet bicoherence is low across the surface but increases during L-NAME. The percentage of time that QPC was declared significant is shown in Fig. 8c&d for CTL and L-NAME at each pixel location, after removal of segments shorter than the integration time. During CTL periods, there is a sparse distribution of pixels with limited QPC. During L-NAME, much of the surface shows significant QPC with some locations showing QPC up to 60% of the time.

Figure 7.8 - Quadratic phase coupling captured across the renal surface.
(a) Time-averaged phase randomized wavelet bicoherence during control and (b) L-NAME. The percentage of time that the phase-randomized wavelet bicoherence is greater than the surrogate-derived threshold at each pixel location after removal of segments less than 100 sec during control and (d) L-NAME. The black region with white lines represents the hair placed across the renal surface.

To further examine the utility of monitoring QPC on a pixel-by-pixel basis, two pixel locations were selected from the CTL and L-NAME periods in Fig. 8. Fig. 9a&b show the power spectra of the two locations during CTL and L-NAME periods, respectively. It is clear that the dynamics, especially the MR (>0.1 Hz), are increased during the L-NAME monitoring period.

The MR during L-NAME includes multiple peaks around 0.2 Hz. Fig. 9c shows the phase-randomized wavelet bicoherence for each of the 2 locations during CTL with the decision of when QPC is present. Limited, short-time periods with QPC exist for both locations. During L-NAME, QPC is present through much of the experimental recording at each location, Fig. 9d, but timing of QPC is not consistent between locations.
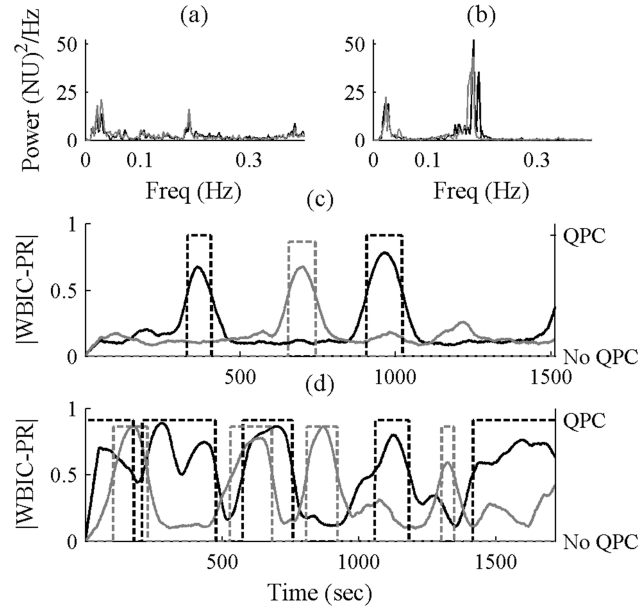
Figure 7.9 - Time-varying presence of quadratic phase coupling in laser speckle signals.
(a) Power spectra during the control period for 2 locations from the laser speckle surface. (b) Power spectra for the approximate same locations during the L-NAME period. (c) Phase-randomized wavelet bicoherence for the 2 locations during the control monitoring period with dashed lines representing the decision of QPC. (d) The same as (c) for the L-NAME monitoring period.

Over the 9 experiments, time-series extracted from individual pixels generally depict limited QPC (< 20% of the data length), but in most experiments a portion of the pixels depict significantly more QPC, up to 40 – 60% as seen in Fig. 8. It may be that these locations with high amounts of QPC represent nephrons with MR and TGF mechanisms operating together. Table IV quantifies the number of pixels with significant QPC, and the amount of time that those pixels are coupled for. Approximately 60% of pixels have at least a 100 sec period with QPC. The remaining 40% do not show any QPC and may represent locations away from individual

nephrons where the image perfusion series is a blend of fluctuations from multiple nearby nephrons.

	CTL	L-NAME
Pixels with QPC (%)	57.7 ± 20.1	63.1 ± 14.1
Median of % Time QPC	10.8 ± 2.2	12.1 ± 3.1
75th Percentile of % Time QPC	16.3 ± 3.7	19.0 ± 4.4
95th Percentile of % Time QPC	25.5 ± 4.4	30.9 ± 6.4

Table 7.4 - Quadratic phase coupling detected across the renal surface.
Percentage of times that QPC is significant is only for pixels with significant QPC. Mean ± SD. N=9.

7.6   Discussion

The simulations presented show that our approach for detecting time-varying QPC detects the presence of such coupling, and not QFC only, when it is present given sufficient time lengths and coupling strengths. This can be used to discriminate between interactions that may cause QFC but not QPC. Such is the case in FM and we did not identify significant amounts of QPC when only FM was present, but we did when AM was present. In renal autoregulation, both AM and FM are part of the TGF-myogenic interaction [10, 11, 21]. Discriminating between AM and FM allows interpretation of the physical mechanisms involved in the interaction. AM may be interpreted as TGF modifying the magnitude of changes in vessel diameter while FM describes how TGF alters the rate at which the MR occurs.

Bicoherence magnitude detectors have been used to identify QPC [22]. These detectors ignore the concept that a high bicoherence can occur without QPC if the phases remain constant throughout the estimation period and that phase coupling requires the biphase to be 0 [1]. Kim *et al.* introduced the phase randomized bicoherence to reduce high bicoherence values during period of only QFC without QPC but with constant phase relationships [18]. This procedure randomizes the biphase when it is not close to 0 which reduces the bicoherence but has little impact when the biphase is close to 0. Li *et al.* expanded on the approach to time-varying

systems by applying it to wavelet bicoherence and providing a significance threshold based on surrogate trials of biphase randomization [15]. They forced the true biphase estimate away from 0 by adding a random number to the biphase. This procedure may result in a bimodal distribution if adding the random number forces the biphase close to 0 in some trials. For this reason, we replaced the estimated biphase with a random variable not close to 0 to develop the estimated significance threshold for the expected phase-randomized wavelet bicoherence.

Previously, a time-varying bispectrum procedure was described that used surrogate data as a significant threshold [4]. This approach only considered the bispectrum magnitude and could therefore not distinguish between QFC and QPC. The phase randomization procedure is computationally efficient compared to other surrogate data techniques because it only requires adjusting phase information after estimation of the wavelet biphase. In this way, the wavelet transform and wavelet bicoherence do not need to be recomputed for each surrogate data trial. We used a wavelet previously applied to renal autoregulation data [21] and an integration time optimized for our frequencies of interest. The wavelet of choice and integration time can be varied if investigating a system with faster or slower components.

In Fig. 3c it is seen that the specificity of not detecting QPC during trials with only QFC is consistent at ~85% across segment lengths and coupling amplitudes. Since we are assigning a random phase, φ_3, in QFC-only trials we will still have a biphase close to 0 in a portion of the trials. If phases are aligned to randomly assign the biphase to 0 when only QFC is present, it is not possible to discriminate it from QPC. This causes the overall accuracies of ~75% in Table I. The false-positive rate carries through to our FM tests where we detect QPC in FM only scenarios ~11% of the time. In real data, we cannot discern QPC from cases of QFC with a biphase that is close to 0, so we consider all cases where we detect QPC.

We focused our physiological investigation specifically on the TGF-myogenic interaction and whether QPC representing AM could be detected between these two components by tracking the frequency components at (f_{TGF}, f_{MYO}). Renal dynamics are more complex than these two mechanisms alone, which is clear from viewing the spectra of our simulation signals in Fig. 1 compared to the RBF data in Fig. 6. Accounting for time-variance using wavelet transforms adjusts for some of the complexity, but there are other factors to consider. Non-linear interactions may also occur between neighboring nephrons [23, 24] and with a reported low frequency mechanism (~0.01 Hz) [25]. The proposed method could be applied to determine the presence of these other interactions in renal autoregulation by varying the frequency ranges of interest or looking at cross-bicoherence between locations in LSPI [26].

Limited QPC (~15 – 20% of the time) was identified in total RBF and LS_{mean}. Previously, QFC was identified for short, transient time periods, but was present for a majority of time in RBF [4]. The present study may indicate that the majority of QFC previously identified was representative of FM with only limited periods of AM. Using double wavelet analysis Sosnovtseva *et al.* showed the myogenic frequency sequence to have a relatively sharp spectral peak around the expected frequency of TGF, while the AM spectral peak was broad in normotensive rats [27]. These results indicate that AM of the MR may have more time-variance than FM, and that TGF may not be the only mechanism that modulates the MR amplitude. In fact, Siu *et al.* identified the presence of AM by a low frequency source that was not found to cause FM [25]. We also previously identified modulation in normotensive and SHRs across frequency ranges that may indicate either TGF or a low frequency modulator in laser Doppler signals [21]. Introduction of an additional modulator of the myogenic mechanism could reduce our ability to detect TGF-based AM.

Signals extracted from single pixels of LSPI have the potential to show much higher amounts of QPC, up to 60% of the time for pixels from certain locations, than RBF or LS_{mean}. Locations where high amounts of QPC are identified may represent signals from single nephrons where we are able to identify the TGF and MR fluctuations. It was previously shown using time-invariant analysis that interactions could be identified in tubule pressure signals and laser Doppler signals from single nephrons [12, 22]. The advantage of LSPI is that it allows us to investigate interactions at multiple locations across the renal surface. This allowed us to see two locations in Fig. 9d that both had high amounts of QPC, but the time points of when QPC occurred varied between locations. This suggests the mechanisms causing QPC are local and supports the idea of it being more difficult to identify QPC in RBF as fluctuations are averaged across all nephrons. In some instances we may not be able to detect QPC because of an insufficient signal-noise ratio that limits our ability to track the TGF and MR signatures in the wavelet spectrum. When we are able to track the TGF and MR signatures and QPC is present between them our approach will detect it.

7.7   Conclusion

In the present study we have provided a method to identify QPC over short time instances and in spatial locations. To accomplish this we combined two technical innovations. First, a time-varying procedure to detect QPC using a phase-randomization wavelet bicoherence procedure was modified for detection of the TGF-myogenic interaction. Previously, a time-varying bispectrum detector was developed that tested for QFC but could not discriminate cases of QPC [4]. The detection procedure was applied to LSPI which provides information about the renal autoregulation dynamics across the imaged renal surface. Combined, the imaging and analytical procedures identify locations where both renal autoregulation mechanisms are

functioning cooperatively with QPC. More specifically, the presented procedure identifies locations in time and space where TGF is having a direct influence on the MR. The combination of LSPI and our analytical procedure could be used to study the heterogeneity of interactions across time and space in healthy and diseased models. We applied the approach to the study of the TGF-myogenic interaction, but the procedure itself is general and can be applied to any system with multiple control systems suspected of non-linear interactions.

7.8   References

[1]   Nikias, C.L. and A. Petropulu. Higher-order spectra analysis: a nonlinear signal processing framework. PTR Prentice-Hall, 1993.

[2]   Nikias, C.L. and M.R. Raghuveer. Bispectrum estimation: A digital signal processing framework. *Proceedings IEEE*. 75:869-91, 1987.

[3]   Zhong, Y., Y. Bai, B. Yang, K. Ju, K. Shin, M. Lee, K.-M. Jan and K.H. Chon. Autonomic nervous nonlinear interactions lead to frequency modulation between low-and high-frequency bands of the heart rate variability spectrum. *American Journal of Physiology. Regulatory, Integrative and Comparative Physiology*. 293:R1961-R68, 2007.

[4]   Raghavan, R., X. Chen, K.-P. Yip, D.J. Marsh and K.H. Chon. Interactions between TGF-dependent and myogenic oscillations in tubular pressure and whole kidney blood flow in both SDR and SHR. *American Journal of Physiology. Renal Physiology*. 290:F720-F32, 2006.

[5]   Cupples, W.A. and B. Braam. Assessment of renal autoregulation. *American Journal of Physiology. Renal Physiology*. 292:F1105-F23, 2007.

[6]   Yip, K.P., N.H. Holstein-Rathlou and D.J. Marsh. Mechanisms of temporal variation in single-nephron blood flow in rats. *American Journal of Physiology. Renal Physiology*. 264:F427-F34, 1993.

[7]   Cupples, W.A. Interactions contributing to kidney blood flow autoregulation. *Current opinion in nephrology and hypertension*. 16:39-45, 2007.

[8]   Chon, K.H., Y.-M. Chen, V.Z. Marmarelis, D.J. Marsh and N.-H. Holstein-Rathlou. Detection of interactions between myogenic and TGF mechanisms using nonlinear analysis. *American Journal of Physiology. Renal Physiology*. 267:F160-F73, 1994.

[9]   Marsh, D.J., O.V. Sosnovtseva, K.H. Chon and N.-H. Holstein-Rathlou. Nonlinear interactions in renal blood flow regulation. *American Journal of Physiology. Regulatory, Integrative and Comparative Physiology*. 288:R1143-R59, 2005.

[10]   Marsh, D.J., O.V. Sosnovtseva, A.N. Pavlov, K.-P. Yip and N.-H. Holstein-Rathlou. Frequency encoding in renal blood flow regulation. *American Journal of Physiology. Regulatory, Integrative and Comparative Physiology*. 288:R1160-R67, 2005.

[11]   Sosnovtseva, O., A. Pavlov, E. Mosekilde, N.-H. Holstein-Rathlou and D. Marsh. Double-wavelet approach to study frequency and amplitude modulation in renal autoregulation. *Physical Review E*. 70:031915, 2004.

[12]   Chon, K.H., R. Raghavan, Y.-M. Chen, D.J. Marsh and K.-P. Yip. Interactions of TGF-dependent and myogenic oscillations in tubular pressure. *American Journal of Physiology. Renal Physiology*. 288:F298-F307, 2005.

[13]   Jamšek, J., A. Stefanovska and P.V. McClintock. Wavelet bispectral analysis for the study of interactions among oscillators whose basic frequencies are significantly time variable. *Physical Review E*. 76:046221, 2007.

[14]   Van Milligen, B.P., E. Sánchez, T. Estrada, C. Hidalgo, B. Branas, B. Carreras and L. Garcia. Wavelet bicoherence: a new turbulence analysis tool. *Physics of Plasmas*. 2:3017, 1995.

[15]   Li, X., D. Li, L.J. Voss and J.W. Sleigh. The comodulation measure of neuronal oscillations with general harmonic wavelet bicoherence and application to sleep analysis. *NeuroImage*. 48:501, 2009.

[16]   Elgar, S. and G. Sebert. Statistics of bicoherence and biphase. *Journal of Geophysical Research. C. Oceans*. 94:10993-98, 1989.

[17]   Elgar, S. and R. Guza. Statistics of bicoherence. *Acoustics, Speech and Signal Processing, IEEE Transactions on*. 36:1667-68, 1988.

[18]   Kim, T., E.J. Powers, W.M. Grady and A. Arapostathis, 'A novel QPC detector for the health monitoring of rotating machines', in *Instrumentation and Measurement Technology Conference Proceedings IEEE*, 2007, pp. 1-6.

[19]   Fackrell, J. and S. McLaughlin, 'Quadratic phase coupling detection using higher order statistics', in *IEE Coll. `Higher Order Statistics in Signal Processing: Are They of Any Use?'*, 1995.

[20]   Scully, C.G., N. Mitrou, B. Braam, W.A. Cupples and K.H. Chon. Detecting physiological systems with laser speckle perfusion imaging of the renal cortex. *American Journal of Physiology. Regulatory, Integrative and Comparative Physiology*. 304(11): R929-39, 2013.

[21]   Scully, C.G., K.L. Siu, W.A. Cupples, B. Braam and K.H. Chon. Time–frequency approaches for the detection of interactions and temporal properties in renal autoregulation. *Annals of Biomedical Engineering*. 41:172-84, 2013.

[22]   Siu, K.L., J. Ann, K. Ju, M. Lee, K. Shin and K.H. Chon. Statistical approach to quantify the presence of phase coupling using the bispectrum. *Biomedical Engineering, IEEE Transactions on*. 55:1512-20, 2008.

[23]   Holstein-Rathlou, N.-H., O.V. Sosnovtseva, A.N. Pavlov, W.A. Cupples, C.M. Sorensen and D.J. Marsh. Nephron blood flow dynamics measured by laser speckle contrast imaging. *American Journal of Physiology. Renal Physiology*. 300:F319-F29, 2011.

[24]   Marsh, D.J., I. Toma, O.V. Sosnovtseva, J. Peti-Peterdi and N.-H. Holstein-Rathlou. Electrotonic vascular signal conduction and nephron synchronization. *American Journal of Physiology. Renal Physiology*. 296:F751-F61, 2009.

[25]   Siu, K.L., B. Sung, W.A. Cupples, L. Moore and K.H. Chon. Detection of low-frequency oscillations in renal blood flow. *American Journal of Physiology. Renal Physiology*. 297:F155-F62, 2009.

[26]   Siu, K.L. and K.H. Chon. On the efficacy of the combined use of the cross-bicoherence with surrogate data technique to statistically quantify the presence of nonlinear interactions. *Annals of Biomedical Engineering*. 37:1839-48, 2009.

[27]   Sosnovtseva, O., A. Pavlov, O. Pavlova, E. Mosekilde and N.-H. Holstein-Rathlou. The effect of L-NAME on intra-and inter-nephron synchronization. *European Journal of Pharmaceutical Sciences*. 36:39-50, 2009.

Chapter 8: Exploring the Relationship between Renal Autoregulation Function and Phase Synchronization

8.1   Introduction

We have shown that laser speckle perfusion imaging (LSPI) time-series can be used to effectively estimate the renal autoregulation properties at points across the renal surface [1]. Using this imaging technique synchronization in the dynamics between locations on the renal surface can be investigated and used to identify clusters of phase synchronized regions as shown in Chap. 6 of this dissertation and [2]. Synchronization between perfusion signals across the surface has been shown indicating coupling in renal autoregulation activity between nephrons. Synchronization between nephrons could lead to improved renal autoregulation effectiveness due to increased regulation of preglomerular resistance and spatial smoothing of blood flow [3], but such physiological significance of synchronization has not been explored.

Here, we show how detection of synchronization in LSPI series can be used to explore the question of how internephron synchronization of the renal autoregulation mechanisms relates to the effectiveness of renal autoregulation. We estimate the overall phase synchronization (for tubuloglomerular feedback (TGF) [0.02 – 0.05 Hz] and the myogenic response (MR) [0.1 – 0.3 Hz] frequency ranges) between time-series extracted from all pixels within the LSPI sequence and compare the estimates of synchronization with estimates of the low frequency system gain [0.005 – 0.02 Hz] [1] as a marker of renal autoregulation effectiveness. Estimates are made over periods of control, enhanced, and reduced renal autoregulation to develop a relationship between synchronization and gain over a range of autoregulation states. We then investigate if synchronization is modulated over time and compare our synchronization modulation sequences with modulation of the system gain.

146

8.2 Methods

8.2.1 Experimental Data Collection

Experimental data used in this Chapter is from a previously published report [1], and details of data collection can be found in Chapter 5. Renal blood flow (RBF), blood pressure (BP), and LSPI data acquired as described in Chapter 5 were used from the BP forcing experiments (N=8) during control, intrarenal infusion of non-selective inhibition of nitric oxide synthase with N^{ω}-nitro-l-arginine methyl ester (L-NAME) and intrarenal infusion of the rho-kinase inhibitor Y-27632 to provide a range of renal autoregulation.

8.2.2 Analytical Approach

Transfer Function Estimation

RBF and BP transfer function estimates are used from [1]. A band-pass filter (f_{c1}=0.004 and f_{c2}=1 Hz) was applied to the RBF and BP recordings. Welch's periodogram method with 512 segment size and 50% overlap between segments was used to estimate transfer function with BP as the input and RBF as the output. Renal autoregulation functions to attenuate low frequency fluctuations in RBF [4], therefore the mean low frequency (0.005 – 0.02 Hz) gain, LF_{GAIN}, in decibels (dB) was used as an indicator of renal autoregulation effectiveness.

Phase Synchronization Estimation

Phase coherence (PC) was estimated between the time-series extracted from each pixel as as a marker of phase synchronization between all pairs of oscillators. The signal from pixel *i* was band-pass filtered and the instantaneous frequency estimated using the Hilbert transform. Band-pass filters were designed for the TGF and MR frequency ranges with pass-bands of 0.02 – 0.06 Hz and 0.09 – 0.032 Hz, respectively. Instantaneous frequencies that jump outside of the pass-

band can occur due to noise and phase slips. These locations are identified and linearly interpolated to reduce the impact of phase slips on the PC estimates. The instantaneous phase, φ_{ik}, is taken as the integral of the instantaneous frequency for pixel i at each time point, k. PC estimates are made for all pairs of pixels by taking the mean of the exponential difference of the instantaneous phases across time, (1). PC estimates are bound between 0 and 1 representing null and complete synchronization.

$$PC_{ij} = \left| \frac{1}{n} \sum_k \exp\left(i(\varphi_{ik} - \varphi_{jk})\right) \right| \tag{1}$$

The average PC between pixel i and all other pixels (2) was used as an indicator of how synchronized pixel i is with all other pixels. A value of R_i close to 1 indicates the phase within the pass band of time-series of pixel i is highly synchronized with that of all other pixels.

$$R_i = \frac{1}{r} \sum_j PC_{ij} \tag{2}$$

The mean of all the bivariate PC estimates was used as an indicator of overall phase synchronization in the image series, (3) [5]. This value assumes that the time-series from all locations combine to form a mean oscillator and is an indicator of how well all pixels are coupled to that mean oscillator.

$$PC_{\mathrm{MEAN}} = \frac{1}{r} \sum_i R_i \tag{3}$$

The standard deviation, σ_{PC}, of all R_i indicates the heterogeneity of synchronization across the surface (4). A lower σ_{PC} indicates a homogenous surface where PC is distributed evenly, while a high σ_{PC} indicates there are regions that are highly coupled and regions that are poorly coupled to the mean oscillator.

$$\sigma_{PC} = \sqrt{\frac{1}{r}\sum_i (R_i - \bar{R}_i)^2}$$ (4)

Time-varying Transfer Function Estimation

Wavelet transforms were estimated for the low-pass filtered and downsampled RBF and BP recordings with a Morlet wavelet function with center frequency of 6 [1, 6]. These were used to estimate the time-varying wavelet transfer function by computing the co- and quadrature spectra. The wavelet power of the RBF wavelet transform within the two frequency regions was also used as an indicator of the RBF amplitude corresponding to the TGF and MR dynamics.

Time-varying Phase Synchronization

The wavelet transform of the time-series from each pixel was computed and used to estimate the instantaneous phase at each frequency. PC was then determined between every pair of pixels at each frequency over a integration period of length *m*. Because PC estimates are related to the number of cycles they are computed over, the integration period *m* was varied for each frequency. Computing PC over too few cycles will result in a high PC value. A minimum of 10 oscillations were used to compute PC. For example, at *f*=0.1 Hz PC was estimated over a 51 second period from *k-25:k+25* at every time point *k*.

$$R_{ij}(f,k) = \left| \frac{1}{2m} \sum_{k-m:k+m} exp\left(i\left(\varphi_{ik}(f) - \varphi_{jk}(f)\right)\right)\right|$$ (5)

Modulation sequences of phase synchronization were extracted for the MR (0.1 – 0.3 Hz) and TGF (0.02 – 0.05 Hz) frequency ranges by averaging across frequencies at each time point, PS_{MYO} and PS_{TGF}, respectively. The low frequency gain modulation sequence between 0.005 – 0.02 Hz was determined by averaging the time-varying wavelet gain at each time point. To determine if time-varying changes in synchronization are related to time-varying changes in the system properties, correlation coefficients between the TGF and MR phase synchronization

sequences and gain estimates were made. The power spectral density was computed for each modulation sequence to identify modulation frequencies after linearly detrending the modulation sequences and normalizing to unit variance. The mean-squared coherence was estimated between the phase synchronization modulation sequences and the time-varying gain estimates for the TGF, MR and low frequency regions.

Statistical Analysis

Data are displayed as mean ± standard error (SE). Statistics were computed with SPSS 17.0, $P<0.05$ considered significant. Comparisons between the TGF and MR frequency ranges were made at each condition (CTL, L-NAME, Y-27632) with paired t-test. Between-condition comparisons were made using repeated measures ANOVA with Sidak post-hoc test for both frequency ranges. Correlation coefficients were computed between the low frequency gain (0.005 – 0.02 Hz) and PC_{MEAN} for the TGF and MR frequency regions.

## 8.3   Time-invariant Analysis

8.3.1   Results

Figure 1 shows an example of R_i for all pixels. This is used as a measure of the synchronization between the time-series extracted from each pixel and a 'mean-field' by assuming all signals belong to a single cluster. A high R_i indicates the pixel is strongly coupled to all other pixels. MR R_i are high and consistent across the surface during control and L-NAME and reduced during Y-27632. For TGF, R_i are low during control and L-NAME but increase during Y-27632. During Y-27632 infusion vasomotion is reduced so that the active renal autoregulation elements contribute less to our recorded flow signals. Therefore, the dominant signals received at each location are induced by forced BP fluctuations.
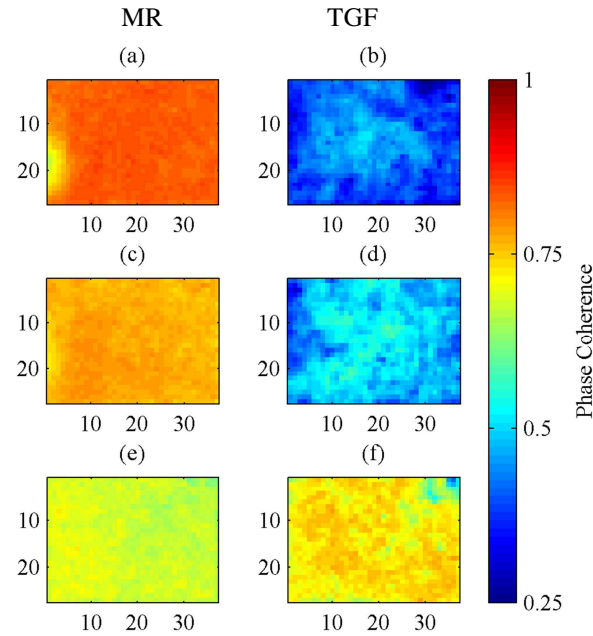
Figure 8.1 - Phase synchronization across the renal surface.
Average phase coherence for the time-series extracted from each pixel with all other pixels, R_i. (a, c, e) are for the myogenic response frequency range and (b, d, f) are for the TGF frequency range. The rows correspond to control, L-NAME, and Y-27632 infusion periods, respectively.

PC_{MEAN} for the three conditions in both the MR and TGF frequency ranges are shown in Figure 2. The MR has significantly higher synchronization than TGF during CTL and L-NAME, but not during Y-27632. The MR-PC_{MEAN} is significantly lower during Y-27632 than CTL and L-NAME infusions.
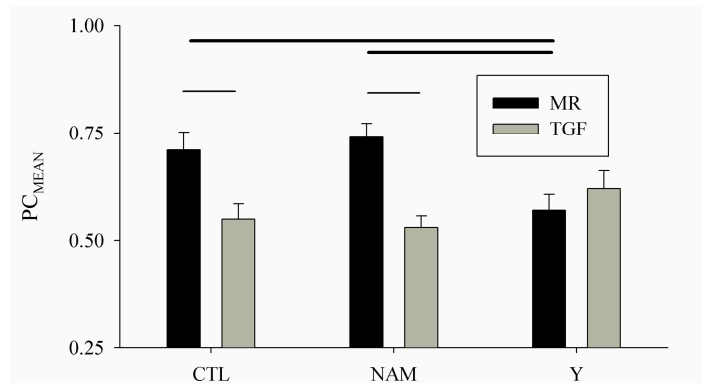
Figure 8.2 - MR and TGF average phase coherence during 3 levels of renal autoregulation.
Mean phase coherence across all pixels for the myogenic and TGF frequency ranges during control, L-NAME and Y-27632 monitoring periods. Data are displayed as mean ± SE, N=8. Thin lines indicate statistical significance between the frequency ranges during the monitoring period using a paired t-test, P<0.05 for CTL and P<0.01 for NAM. Thick lines indicate significance between monitoring periods for the same frequency region using repeated measures ANOVA with Sidak post-hoc test, P<0.05 for CTL-Y and P<0.01 for NAM-Y.

To describe the variance in synchronization between pixels across the surface, the standard deviation of all R_i, σ_{PC}, are shown in Figure 3. Under all three conditions the variability of synchronization across the surface is higher in the TGF than MR frequency range. No difference is found in the variance of synchronization across the surface between infusion periods for either frequency range.
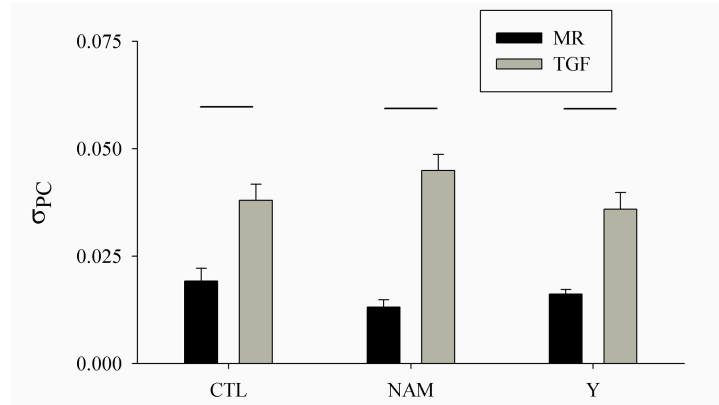
Figure 8.3 - Spatial variance of synchronization.
Standard deviations of the synchronization strength over all pixels. Thin lines indicate statistical significance between the frequency ranges during the monitoring period using paired t-test, P<0.05. Thick lines indicate statistical significance between monitoring periods for the same frequency region using repeated measures ANOVA with Sidak post-hoc test, P<0.01.

PC_{MEAN} for the MR and TGF across all conditions and animals are plotted against the estimated low frequency gain from RBF and BP measurements in Figure 4a&b, respectively. A negative correlation coefficient (r=-0.36, P=0.081) exists for the MR-PC_{MEAN} and low frequency gain relationship. A significant positive correlation coefficient (r=0.53, P=0.008) exists for the TGF-PC_{MEAN} and low frequency gain estimate. The more negative the low frequency gain the more effective renal autoregulation is at attenuating BP fluctuations. Therefore, higher MR-PC_{MEAN} is associated with more effective renal autoregulation. For TGF, a lower PC_{MEAN} is correlated with more effective renal autoregulation.
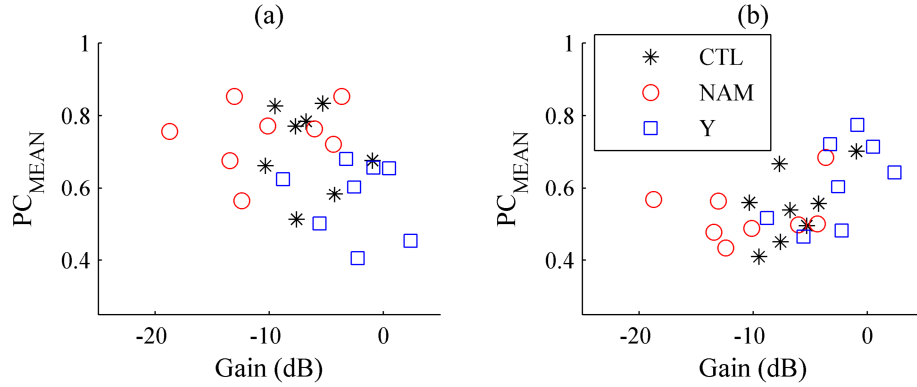
Figure 8.4 - Scatter plots of synchronization strengths versus renal autoregulation gain.
Scatter plot of cluster strengths for MR (a) and TGF (b) frequency regions versus the low frequency gain estimate (0.005 – 0.02 Hz) from renal blood flow and blood pressure transfer functions for the three monitoring periods for each animal.

8.3.2   Discussion

In this study, we investigated the relationship between phase synchronization in the renal autoregulation dynamics acquired from perfusion signals across the renal cortex and renal autoregulation effectiveness. The mean of bivariate PC estimates was used as a measure of synchronization among time-series from all pixels, and the low frequency gain (0.005 – 0.02 Hz) from RBF and BP transfer functions was used as an indicator of renal autoregulation effectiveness. To ensure a range of renal autoregulation responses, forced fluctuations in BP were generated during CTL, L-NAME and Y-27632.

The MR occurs directly in the afferent arteriole resulting in a response time of ~7-10 sec [4]. Therefore, if a strong BP fluctuation approaches all points in the vasculature at approximately the same time, the vasculature in all areas can respond appropriately. While we are continuously forcing BP fluctuations, there is little chance for desynchronized oscillations to develop. The MR of all afferent arterioles are entrained to the BP fluctuations. This is shown by the high PC_{MEAN} during CTL and L-NAME. During periods of high MR synchronization LF_{GAIN} is reduced, possibly indicating that a larger area of the vasculature is simultaneously responding

to attenuate fluctuations in RBF. In the situation of this study where forced BP fluctuations are dominating any locally generated oscillations, the MR is potentially hemodynamically coupled between nephrons. During Y-27632 the active MR is reduced and we see a decrease in PC_{MEAN}. Since there is no longer a strong MR additional noise is likely being captured in the flow signals resulting in a reduced PC_{MEAN}.

Contrasting the potential hemodynamic coupling of the MR, TGF has delays in response time on the order of 50 sec caused by tubule length and signaling mechanisms at the macula densa [7] and has been shown to be electrotonically coupled between nephrons [8]. Differences in TGF delay times among nephrons could be the cause of lower PC_{MEAN} indicating reduced synchronization during CTL and L-NAME conditions in the TGF frequency range than the MR. This is also seen by the higher variance in the average PC for each pixel with all other pixels for TGF. More heterogeneity exists in TGF dynamics across the renal surface. The positive correlation between TGF-PC_{MEAN} and LF_{GAIN} indicates that when renal autoregulation is more effective at reducing BP fluctuations TGF is occurring with increased independence among locations. There is less entrainment of TGF from forced BP fluctuations resulting in lower TGF-PC_{MEAN} than for the MR.

8.4   Time-variant Analysis

8.4.1   Results

The PC and gain estimates were expanded across time to identify if a relationship existed between temporal changes in synchronization and gain. Figure 5 shows an example of the procedure to investigate the time-variance of renal autoregulation synchronization.
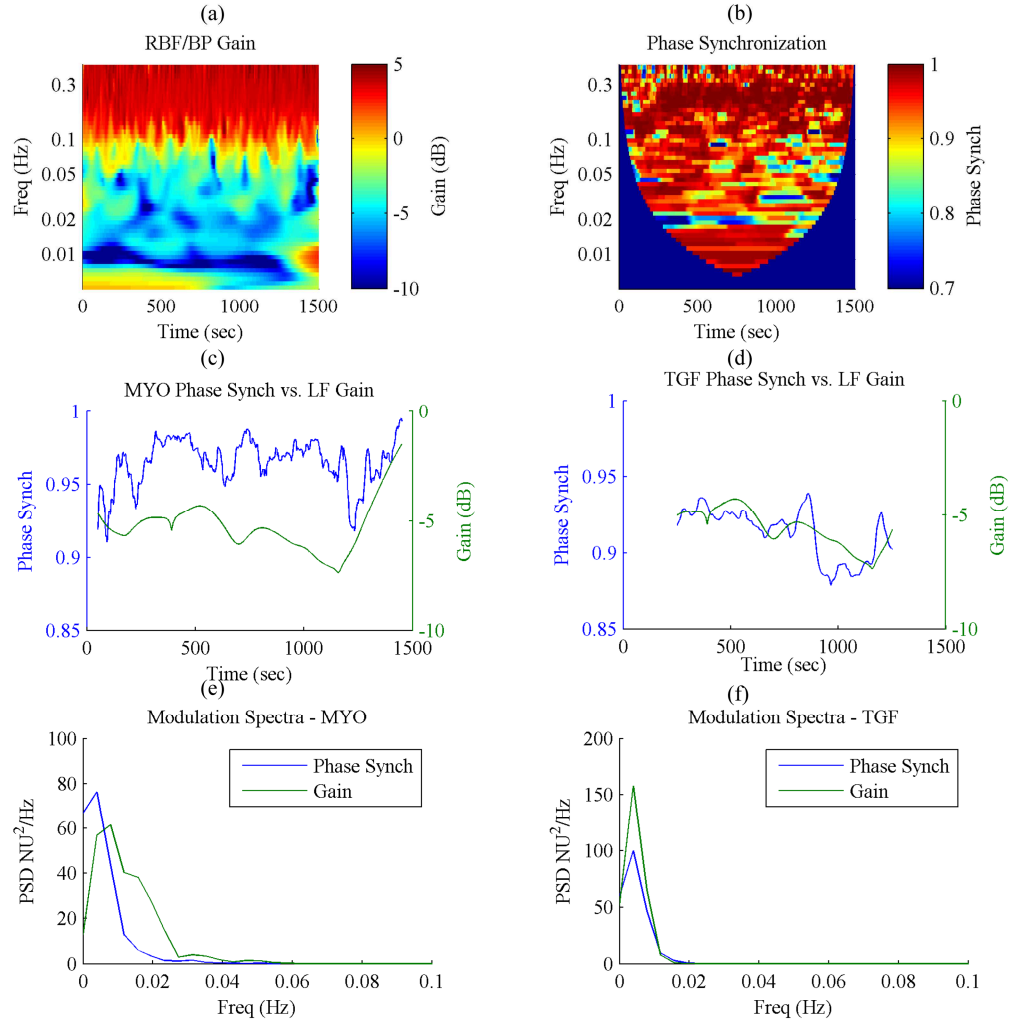
Figure 8.5 - Example of time-varying synchronization analysis.
Analysis of time-varying synchronization for one animal during the L-NAME monitoring period. (a) Renal blood flow and blood pressure time-varying transfer function. (b) Time-varying phase synchronization averaged across all pixels. (c) Myogenic modulation sequence for time-varying phase synchronization and time-varying low-frequency gain. (d) TGF modulation sequence alongside low-frequency gain modulation sequence. (e) Power spectra of the myogenic phase synchronization modulation sequence and time-varying myogenic system gain. (f) TGF modulation sequence spectra.

First, the wavelet gain and phase synchronization are estimated as in Figure 5a&b, respectively. Values across the frequency region at each time point are averaged together to develop modulation sequences for both mechanisms. Figure 5c shows the MR phase synchronization alongside the low frequency gain estimate, and Figure 5d shows the same for the TGF phase synchronization. The power spectrum of each modulation sequence is generated to determine if the indices vary with a regular pattern, Figure 5e&f.

155

Correlation coefficients between the relevant modulation sequences for each animal and condition are shown in Figure 6 (correlation between extracted synchronization time-series and extracted gain or amplitude in the respective frequency range from the time-frequency representations). Over the 24 data points (N=8 animals with 3 conditions) the correlation coefficients were compared to 0 for each pair of modulation sequences. The correlation coefficient between MR phase synchronization and MR RBF amplitude had a mean significantly greater than 0 (P<0.001). TGF phase synchronization had a mean correlation coefficient significantly positive with low frequency gain (P=0.014) and the TGF amplitude estimated from RBF (P=0.005).
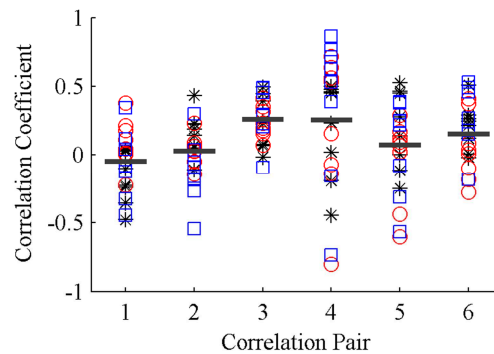
Figure 8.6 - Correlations between gain and synchronization time-series.
Correlation coefficients between phase synchronization modulation sequences and system parameters for each animal (N=8) and each condition (CTL – black star, L-NAME – red circle, Y-27632 – blue square). Gray lines correspond to the mean correlation coefficient at each pair. Correlation pairs correspond to the following: (1) MR phase synchronization and low frequency gain, (2) MR phase synchronization and MR gain, (3) MR phase synchronization and MR amplitude, (4) TGF phase synchronization and low frequency gain, (5) TGF phase synchronization and TGF gain, and (6) TGF phase synchronization and TGF amplitude.

Power spectra for the modulation sequences averaged across animals for the three conditions are shown in Figure 7. A consistent modulation frequency is not found for phase synchronization for the MR or TGF (7a&d, respectively). MR gain and amplitude have some low frequency modulation seen by the higher power in the region >0.01 Hz. This is not seen on the phase synchronization or TGF gain and amplitude spectra.
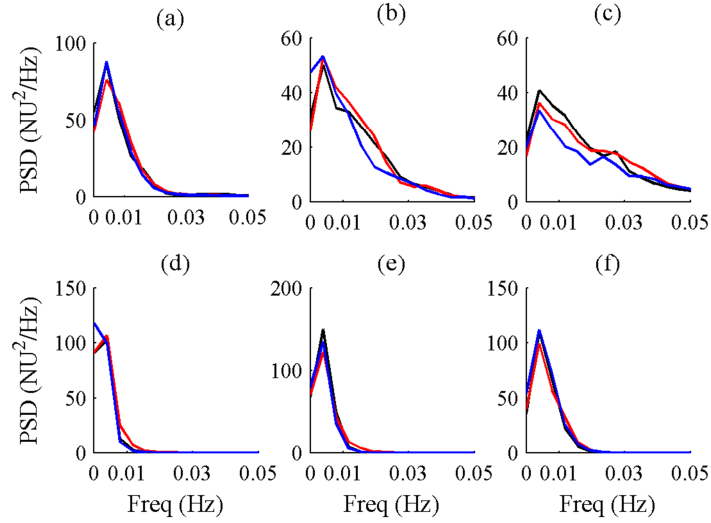
Figure 8.7 - Spectra of modulation sequences.
Mean spectra of the modulation sequences (N=8) for (a) myogenic phase synchronization, (b) myogenic gain, (c) myogenic renal blood flow amplitude, (d) TGF phase synchronization, (e) TGF gain, and (f) TGF renal blood flow amplitude. Control (black), L-NAME (red), and Y-27632 (blue).

The average coherence spectra between phase synchronization and gain estimates are shown in Figure 8 across all animals. Coherence is low across all frequencies for both the TGF and MR phase synchronization estimates with low frequency gain. The same is true for TGF and MR phase synchronization estimates with the gain from their respective frequency regions.
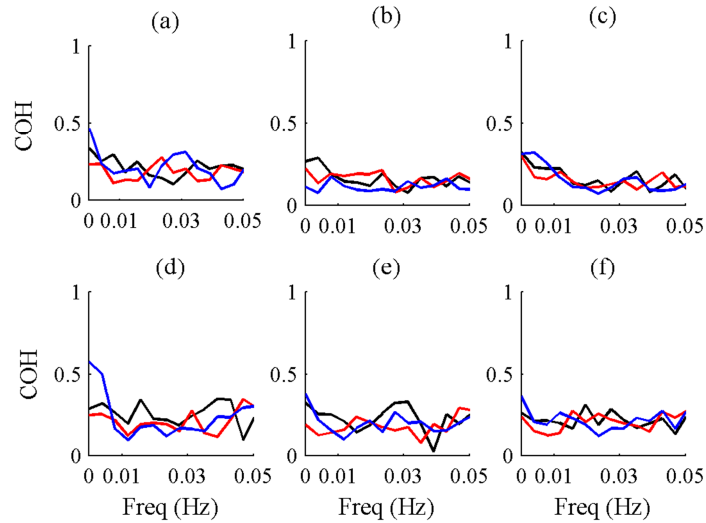
Figure 8.8 - Coherence between modulation sequences.
Mean coherence of the phase synchronization modulation sequences and gain and amplitude modulation sequences (N=8). (a, b, c) myogenic phase synchronization versus low frequency gain, myogenic gain, and myogenic amplitude, respectively. (d, e, f) TGF phase synchronization versus low frequency gain, TGF gain, and TGF amplitude, respectively. Control (black), L-NAME (red), and Y-27632 (blue).

157

8.4.2 Discussion

The relationship between phase synchronization across the renal surface and renal autoregulation function was studied using time-varying analysis. MR phase synchronization indices from LSPI had a slight positive correlation with the MR amplitude estimated from RBF, but not with low frequency gain or the MR gain. TGF phase synchronization had a slight positive correlation with low frequency gain as well as the TGF amplitude estimated from RBF. We did not find consistent modulation frequencies for time-varying phase synchronization indices for either the TGF or MR frequency ranges. The previously reported 0.01 Hz frequency [9, 10] present in RBF was not identified in phase synchronization modulation. Without any consistent modulation frequencies coherence between phase synchronization and system properties at any frequency was not expected, and we did not find coherence between time-varying changes in system gain and phase synchronization. We did not find significant changes in modulation during control, L-NAME, or Y-27632 monitoring periods.

Phase synchronization in the imaged area did not vary in time enough to alter the system properties. With LSPI only perfusion relative to a subset of the renal vasculature can be examined at any time. For this reason we might not expect to find agreement between phase synchronization in the area we are looking at and the system properties. Other areas that are not being imaged may have a more significant contribution to the overall system properties. Weak correlations are present between the MR and TGF phase synchronization indices and respective RBF amplitudes. This is expected as more arterioles that are responding at the same time will produce a stronger effect in total RBF.

When examining synchronization there is a tradeoff between the accuracy of the PC estimate and time over which PC is computed [11]. We know that time-varying dynamics are

present in renal autoregulation and PC estimates how well the dynamics from two signals vary in time together. As we look at shorter periods of time two signals that are not phase-locked will appear to have a stronger phase relationship than if we looked over a longer period [11]. This makes it difficult to investigate time-varying synchronization and questions what is actually meant by time-varying synchronization. Signals with similar frequencies will, for short periods of time, appear synchronized. Marsh *et al.* showed in modeling studies that nephron dynamics can spontaneously synchronize over short periods, and that the time scale that this occurred is similar to the previously identified 0.01 Hz frequency [12]. In this study we attempted to investigate if such synchronization modulation could be identified in LSPI data of renal cortical blood flow, and if so if it was related to any changes in system properties. We did not find modulation in our synchronization indices. Further investigations into the tradeoff between the temporal resolution and accuracy of synchronization estimates are needed. These would inform the limits of what we can investigate and have confidence in terms of time-varying renal autoregulation synchronization. We used wavelet analysis to generate our time-varying indices because of their use in renal autoregulation studies and computation speed, but this may not be the best approach to monitor changes across the different frequency regions of interest [6].

This study demonstrates how the relationship between renal autoregulation synchronization among nephrons and renal autoregulation effectiveness can be examined by comparing analysis of LSPI with that of RBF and BP.

8.5　References

[1]　Scully, C.G., N. Mitrou, B. Braam, W.A. Cupples and K.H. Chon. Detecting physiological systems with laser speckle perfusion imaging of the renal cortex. *American Journal of Physiology. Regulatory, Integrative and Comparative Physiology*. 304(11): R929-39, 2013.

[2]　Holstein-Rathlou, N.H., O.V. Sosnovtseva, A.N. Pavlov, W.A. Cupples, C.M. Sorensen and D.J. Marsh. Nephron blood flow dynamics measured by laser speckle contrast imaging. *American Journal of Physiology. Renal Physiology*. 300:F319-F29, 2011.

[3]   Cupples, W.A. Interactions contributing to kidney blood flow autoregulation. *Current Opinion in Nephrology and Hypertension*. 16:39-45, 2007.

[4]   Cupples, W.A. and B. Braam. Assessment of renal autoregulation. *American Journal of Physiology. Renal Physiology*. 292:F1105-F23, 2007.

[5]   Allefeld, C. and J. Kurths. An approach to multivariate phase synchronization analysis and its application to event-related potentials. *International Journal of Bifurcation and Chaos*. 14:417-26, 2004.

[6]   Scully, C.G., K.L. Siu, W.A. Cupples, B. Braam and K.H. Chon. Time–frequency approaches for the detection of interactions and temporal properties in renal autoregulation. *Annals of Biomedical Engineering*. 41:172-84, 2013.

[7]   Layton, A.T., L.C. Moore and H.E. Layton. Multistability in tubuloglomerular feedback and spectral complexity in spontaneously hypertensive rats. *American Journal of Physiology. Renal Physiology*. 291:F79-F97, 2006.

[8]   Marsh, D.J., I. Toma, O.V. Sosnovtseva, J. Peti-Peterdi and N.-H. Holstein-Rathlou. Electrotonic vascular signal conduction and nephron synchronization. *American Journal of Physiology. Renal Physiology*. 296:F751-F61, 2009.

[9]   Siu, K.L., B. Sung, W.A. Cupples, L.C. Moore and K.H. Chon. Detection of low-frequency oscillations in renal blood flow. *American Journal of Physiology. Renal Physiology*. 297:F155-F62, 2009.

[10]   Pavlov, A.N., O.V. Sosnovtseva, O.N. Pavlova, E. Mosekilde and N.-H. Holstein-Rathlou. Characterizing multimode interaction in renal autoregulation. *Physiological Measurement*. 29:945, 2008.

[11]   Hurtado, J.M., L.L. Rubchinsky and K.A. Sigvardt. Statistical method for detection of phase-locking episodes in neural oscillations. *Journal of Neurophysiology*. 91:1883-98, 2004.

[12]   Marsh, D.J., A.S. Wexler, A. Brazhe, D.E. Postnov, O.V. Sosnovtseva and N.-H. Holstein-Rathlou. Multinephron dynamics on the renal vascular network. *American Journal of Physiology. Renal Physiology*. 304:F88-F102, 2013.

Chapter 9: Conclusions and Future Work

9.1   Conclusions

This thesis describes the development of techniques for the characterization of renal autoregulation dynamics across time and space. Previous studies have investigated renal autoregulation dynamics within and between nephrons using single or pairs of flow or pressure signals and were therefore limited in the properties that could be explored [1-8]. The methods described here are particularly designed to take advantage of the joint spatial and temporal information provided from laser speckle perfusion imaging (LSPI) of the renal cortex. As outlined in Figure 1, these methods provide information about the spatial and temporal dynamics across the renal surface, synchronization between perfusion signals, and TGF-myogenic interaction in time and space. Taken together these approaches allow for a more complete characterization of renal autoregulation dynamics than what was previously available.
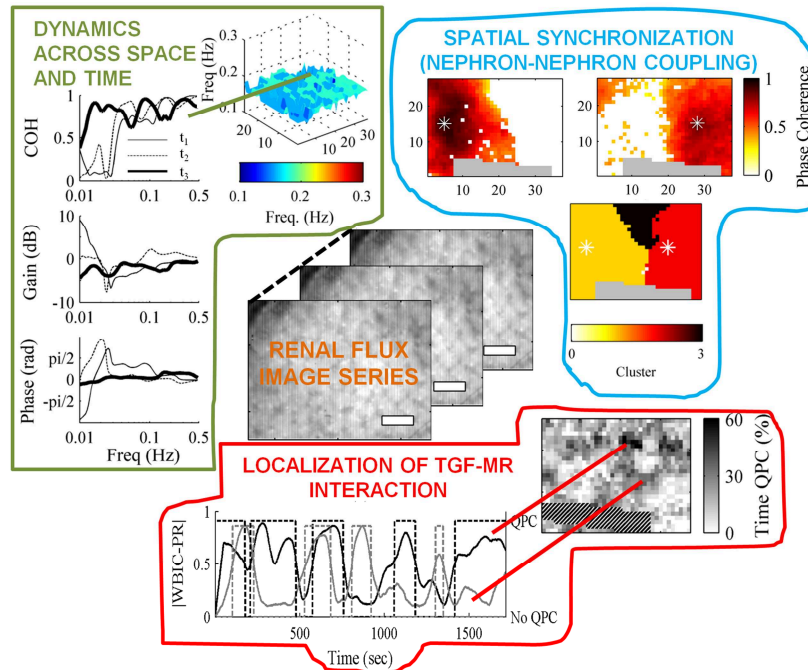
Figure 9.1 - Techniques presented in this dissertation for spatial and temporal renal autoregulation analysis.

We investigated LSPI as a tool for monitoring renal cortical perfusion across the cortex and found agreement with renal blood flow (RBF). Frequencies characteristic of tubuloglomerular feedback (TGF) and the myogenic response (MR) were identified within time-series of LSPI pixels. Oscillations related to the cardiac pulse, respiration and mesentery baroreflex were found to be homogenous at all locations within the imaging window and agreed with frequencies identified in RBF. Contrasting this, the renal autoregulation dynamics could be heterogeneous across the surface indicating local generation of signals. Transfer function analysis using LSPI provided equivalent information to that obtained from RBF.

With the knowledge that spatial heterogeneity of the renal autoregulation dynamics could be identified with LSPI, we developed an approach to identify regions across the surface with phase synchronized dynamics. The approach makes use of the idea that renal autoregulation dynamics are non-stationary and that LSPI can capture the time-varying characteristics of such data. Renal autoregulation frequencies vary over time, but when nephrons are coupled their frequencies should vary in time similarly. By investigating the phase relationship over time between all pixel pairs a synchronization matrix can be developed indicating the phase coupling between the time-series from each pixel with every other pixel. The synchronization matrix is used as a basis for clustering and when clustering results are mapped back to the respective pixels a map of phase coupled regions is generated. This approach allows for visual interpretation of how renal autoregulation dynamics are synchronized across the renal surface.

While the previous approach is capable of monitoring synchronization of the renal autoregulation dynamics between nephrons, it has also been shown that the two feedback mechanisms in each nephron can interact with each other, referred to as the TGF-myogenic interaction. We developed an approach capable of detecting the presence of quadratic phase

162

coupling between the TGF and MR across the renal surface. The algorithm is capable of identifying short periods of quadratic phase coupling. When applied to renal autoregulation data intermittent quadratic phase coupling was found. Applying the algorithm to LSPI allows us to identify locations where both mechanisms are operating in a cooperative fashion.

The intended goal of the methods presented in this report is to enable studies to further our understanding of how interactions play a role in renal autoregulation function. Towards this end we investigated how phase synchronization in perfusion signals across the renal surface is related to renal autoregulation effectiveness. We found that synchronization of the MR had a slight negative correlation with the low frequency gain estimate while TGF synchronization was positively correlated with the low frequency gain estimate when blood pressure (BP) fluctuations are forced. These results may point to differences in the modes of coupling and significance of TGF and MR synchronization. When the time-varying nature of synchronization was investigated no conclusive results indicated a consistent modulator of synchronization, or a relationship between synchronization and system gain changes over time. The presented work in this area is meant as an outline of approaches to be taken for investigating the relationship between synchronization and renal autoregulation effectiveness and is not complete for an understanding of this purpose.

9.2   Future Work

As discussed, the purpose of these approaches is to enable future studies to characterize renal autoregulation dynamics across spatial and temporal scales and investigate the significance and mechanisms of interactions. One of the most interesting applications of the described approaches would be to characterize interactions amongst a variety of animal models that represent a range of renal autoregulation under a range BPs. For example, it has previously been

shown between pairs of nephrons that Spontaneously Hypertensive Rats (SHRs) have increased complexity and time-variance over normotensive SDRs [3, 7, 9, 10]. SHRs have highly effective autoregulation as they are able to withstand high BP without suffering renal damage; therefore there is much interest in understanding complexity in renal autoregulation. It is expected that the increased complexity observed in SHRs in recordings of flow in single or pairs of nephrons would be identified by a higher number of small localized clusters and increased time-variance in the TGF-myogenic interaction. Results from SHRs should be compared with normotensive animals as well as normotensive and hypertensive animals that are susceptible to renal injury, such as the Brown-Norway (normotensive animal but susceptible to hypertensive-induced renal damage [11]), STZ diabetic (can show efficient renal autoregulation but susceptible to renal damage [12]), and remnant kidney (chronic kidney disease model showing progressive hypertension with impaired renal autoregulation [13]) rats. Such studies could result in knowledge about the physiological significance of interactions and their role during disease, particularly characterization of diabetic and remnant kidney models could lead to a more informed understanding of renal autoregulation dynamics during the progression of hypertension under those conditions.

The information that can be acquired about renal autoregulation dynamics is limited to the instruments capable of recording flow signals and approaches for analysis of such data. LSPI is based on the statistics of speckle patterns as determined over a spatial or temporal set of pixels. It has been shown that the number of pixels used to estimate the speckle contrast is proportional to the signal-noise ratio, as more pixels are averaged the signal-noise ratio increases [14]. In this work we used the commercially available moorFLPI which computes speckle contrast with a fixed number of pixels, 25, over either temporal or spatial dimensions. We found a need to

average additional pixels after the mooFLPI flux computation to increase the signal-noise ratio of the TGF and MR. There is a trade-off between the number of pixels averaged and our spatial and temporal resolution. Use of the moorFLPI is limited in this sense because the system has a 568x760 pixel CCD camera at 25 Hz. Using the Gaussian filter that we found necessary provides an effective pixel resolution of ~160 μm, not sufficient to identify individual vascular components of the renal microcirculation. By using a CCD camera with a higher pixel density or increased frame rate it may be possible to decrease the effective pixel resolution. This would be most advantageous if raw CCD camera data were available for processing rather than the moorFLPI flux data which is already processed and has lost either spatial or temporal resolution depending on the computation setting used. By increasing the number of pixels used to compute the speckle contrast it is possible that the overall number of pixels used, and hence spatial resolution, could be decreased.

The potential of the described methods would further be boosted as a research instrument by performing anatomical imaging such as microtomography after the experiments. Such imaging can be used to map the renal vasculature [15]. With proper alignment it would be possible to combine anatomical with the functional information obtained from LSPI, further increasing the value of the analytical approaches described in this report. By investigating the vascular structure underlying clusters of phase synchronized regions we can determine the number of nephrons and distances involved in the formation of clusters and have a more complete understanding of what our phase synchronized clusters represent.

It should be noted that studies of autoregulation are not limited to the renal microcirculation, and neither are the methods described here. Rather they are applicable to video imaging representing flow data from any vascular bed. As shown in Chapter 5, even in the renal

microcirculatory flow dynamics other than those related to renal autoregulation can be captured and analyzed further. This provides the potential to explore the relationship between the cardiac and renal systems by capturing the dynamics related to each with LSPI and using our time-varying quadratic phase coupling test to detect interactions.

In this dissertation we have focused on developing approaches for LSPI as a research instrument. LSPI requires invasive procedures and stabilization of the kidney making it ill-suited for many clinical applications. Situations where the renal surface is exposed and observed to determine organ viability could benefit by the use of LSPI to monitor the renal microcirculation such as organ transplant or renal surgeries. Alternatively, applying the analytical procedures to non-invasive ultrasound imaging of renal perfusion could allow renal autoregulation studies as a general diagnostic procedure [16]. Future studies characterizing spatial and temporal interactions in various pathophysiological animal models could inform us if clinically relevant diagnostics might be obtained from our analytic techniques.

9.3   References

[1]   Chon, K.H., Y.-M. Chen, V.Z. Marmarelis, D.J. Marsh and N.-H. Holstein-Rathlou. Detection of interactions between myogenic and TGF mechanisms using nonlinear analysis. *American Journal of Physiology. Renal Physiology*. 267:F160-F73, 1994.

[2]   Chon, K.H., R. Raghavan, Y.-M. Chen, D.J. Marsh and K.-P. Yip. Interactions of TGF-dependent and myogenic oscillations in tubular pressure. *American Journal of Physiology. Renal Physiology*. 288:F298-F307, 2005.

[3]   Raghavan, R., X. Chen, K.-P. Yip, D.J. Marsh and K.H. Chon. Interactions between TGF-dependent and myogenic oscillations in tubular pressure and whole kidney blood flow in both SDR and SHR. *American Journal of Physiology. Renal Physiology*. 290:F720-F32, 2006.

[4]   Siu, K.L. and K.H. Chon. On the efficacy of the combined use of the cross-bicoherence with surrogate data technique to statistically quantify the presence of nonlinear interactions. *Annals of Biomedical Engineering*. 37:1839-48, 2009.

[5]   Chen, Y.M., K.P. Yip, D.J. Marsh and N.H. Holstein-Rathlou. Magnitude of TGF-initiated nephron-nephron interactions is increased in SHR. *American Journal of Physiology - Renal Physiology*. 269:F198-F204, 1995.

[6]   Holstein-Rathlou, N.H. Synchronization of proximal intratubular pressure oscillations: evidence for interaction between nephrons. *Pflügers Archiv European Journal of Physiology*. 408:438-43, 1987.

[7] Sosnovtseva, O.V., A.N. Pavlov, E. Mosekilde, K.-P. Yip, N.-H. Holstein-Rathlou and D.J. Marsh. Synchronization among mechanisms of renal autoregulation is reduced in hypertensive rats. *American Journal of Physiology - Renal Physiology*. 293:F1545-F55, 2007.

[8] Yip, K.P., N.H. Holstein-Rathlou and D.J. Marsh. Dynamics of TGF-initiated nephron-nephron interactions in normotensive rats and SHR. *American Journal of Physiology. Renal Physiology*. 262:F980-F88, 1992.

[9] Chon, K.H., Y. Zhong, L.C. Moore, N.H. Holstein-Rathlou and W.A. Cupples. Analysis of nonstationarity in renal autoregulation mechanisms using time-varying transfer and coherence functions. *American Journal of Physiology. Regulatory, Integrative and Comparative Physiology*. 295:R821-R28, 2008.

[10] Layton, A.T., L.C. Moore and H.E. Layton. Multistability in tubuloglomerular feedback and spectral complexity in spontaneously hypertensive rats. *American Journal of Physiology. Renal Physiology*. 291:F79-F97, 2006.

[11] Wang, X. and W.A. Cupples. Interaction between nitric oxide and renal myogenic autoregulation in normotensive and hypertensive rats. *Canadian journal of physiology and pharmacology*. 79:238-45, 2001.

[12] Sima, C.A., M.P. Koeners, J.A. Joles, B. Braam, A.B. Magil and W.A. Cupples. Increased susceptibility to hypertensive renal disease in streptozotocin-treated diabetic rats is not modulated by salt intake. *Diab tologia*. 55:2246-55, 2012.

[13] Bidani, A.K., M.M. Schwartz and E.J. Lewis. Renal autoregulation and vulnerability to hypertensive injury in remnant kidney. *American Journal of Physiology - Renal Physiology*. 252:F1003-F10, 1987.

[14] Skipetrov, S.E., J. Peuser, R. Cerbino, P. Zakharov, B. Weber and F. Scheffold. Noise in laser speckle correlation and imaging techniques. *Opt. Express*. 18:14519-34, 2010.

[15] Nordsletten, D.A., S. Blackett, M.D. Bentley, E.L. Ritman and N.P. Smith. Structural morphology of renal vasculature. *American Journal of Physiology. Heart and Circulatory Physiology*. 291:H296-H309, 2006.

[16] Schneider, A., L. Johnson, M. Goodwin, A. Schelleman and R. Bellomo. Bench-to-bedside review: Contrast enhanced ultrasonography - a promising technique to assess renal perfusion in the ICU. *Critical Care*. 15:157, 2011.